ROYAUME DU MAROC
Université Mohammed V
- RABAT -
جامعة محمد الخامس
– الرباط –
Faculté des sciences
كلية العلوم
CENTRE D'ETUDES DOCTORALES - SCIENCES ET TECHNOLOGIES

N° d'ordre 3372

THESE

En vue de l'obtention du : ***DOCTORAT***

Structure de Recherche : Laboratoire de la Matière condensée et des Sciences interdisciplinaires
Discipline : Physics Informatics
Speciality : Material Science and Renewable Energies

Présentée et soutenue le : 14/11/2020 par :

Loubaba ATTOU

Elaboration and investigation on CuO/Pt-TiO2 NTs composite material for Supercapacitors applications

JURY

Abdelilah BENYOUSSEF	PES, Académie des Sciences et Technologies, Hassan II, Rabat	Président
Hamid EZ-ZAHRAOUY	PES, Université Mohammed V-Rabat, Faculté des Sciences	Directeur de thèse
Boujemaâ JABER	PES, UATRS/CNRST, Rabat	Co-Directeur de thèse
Mohamed BENAISSA	PES, Université Mohammed V-Rabat, Faculté des Sciences	Rapporteur/Examinateur
Lahoucine BAHMAD	PES, Université Mohammed V-Rabat, Faculté des Sciences	Rapporteur/Examinateur
Noureddine MASAIF	PES, Université Ibn Tofail-Kénitra, Faculté des Sciences	Rapporteur/Examinateur

Année Universitaire : 2020-2021

ROYAUME DU MAROC
Université Mohammed V - RABAT -
جامعة محمد الخامس – الرباط –
Faculté des sciences
كلية العلوم
CENTRE D'ETUDES DOCTORALES - SCIENCES ET TECHNOLOGIES

N° d'ordre 3372

THESE

En vue de l'obtention du : ***DOCTORAT***

Structure de Recherche : Laboratoire de la Matière condensée et des Sciences interdisciplinaires
Discipline : Physics Informatics
Speciality : Material Science and Renewable Energies

Présentée et soutenue le : 14/11/2020 par :

Loubaba ATTOU

Elaboration and investigation on CuO/Pt-TiO2 NTs composite material for Supercapacitors applications

JURY

Abdelilah BENYOUSSEF	PES, Académie des Sciences et Technologies, Hassan II, Rabat	Président
Hamid EZ-ZAHRAOUY	PES, Université Mohammed V-Rabat, Faculté des Sciences	Directeur de thèse
Boujemaâ JABER	PES, UATRS/CNRST, Rabat	Co-Directeur de thèse
Mohamed BENAISSA	PES, Université Mohammed V-Rabat, Faculté des Sciences	Rapporteur/Examinateur
Lahoucine BAHMAD	PES, Université Mohammed V-Rabat, Faculté des Sciences	Rapporteur/Examinateur
Noureddine MASAIF	PES, Université Ibn Tofail-Kénitra, Faculté des Sciences	Rapporteur/Examinateur

Année Université : 2020-2021

Dedication

♣ *To my generous parents, for the reason of what i become today, thank you for your great support and continuous care.*

♣ *To My brothers, Taha and Saâd,*

♣ *To my beloved family…*

Acknowledgements

The work presented above was made at three different unities, at the Mohammed V University in Rabat, Faculty of Sciences, in the Laboratory of Condensed Matter and Interdisciplinary Sciences (LaMCScI) under the supervision of Pr. Hamid EZ-ZAHRAOUY, at UATRS in CNRST (National Center for Scientific and Technical Research) under the supervision of Pr. Boujemaâ JABER and at the Institute for Materials and Surface Technology at the University of Applied Sciences, Kiel in Germany.

First and foremost, I wish to thank warmly my supervisor, Mr. **Hamid EZ-ZAHRAOUY**, PES, Professor at the Faculty of Sciences, Mohammed V University in Rabat for his indispensable advices and visionary supervision, for all of the encouragements and supports he gave me, on my research work, on my publication and thesis write-up. I am especially thankful to him.

I would like to express my highest regards to my thesis co-supervisor, Mr. **Boujemaâ JABER**, PES, head Member of the UATRS division at the National Center for Scientific and Technical Research (CNRST), for his seriousness, kindness and good advice, my sincere gratitude geos to for his concern and his directing for all the experimental work that were carried out at the CNRST.

Besides my supervisors, it is a pleasure to thanks the thesis committee for reporting and reviewing my thesis and giving their useful comments.

My deepest thanks goes to my thesis president, Mr. **Abdelilah BENYOUSSEF**, PES, Director of Materials and Nanomaterials Center at MAScIR Foundation and resident member of the Hassan II Academy of Science and Technology in Rabat.

I would like also to offer my thanks to my thesis Rapporteur and Examinateur, Mr. **Mohammed BENAISSA**, PES, Professor at the Faculty of Sciences, Mohammed V University in Rabat, who kindly judge this work by agreeing to be part of jury members.

I would like also to offer my thanks to my thesis Rapporteur and Examinateur, Mr. **Lahoucine BAHMAD**, PES, Professor at the Faculty of Sciences, Mohammed V University in Rabat, for his acceptance to reviewing my thesis.

I would like to express my sincere thanks to my thesis Rapporteur and Examinateur, Mr. **Noureddine MASAIF**, PES, Professor at the Faculty of Sciences, Ibn Tofail University in Kenitra, for his acceptance to reviewing my thesis.

I want to thank Prof. **Mohammed ES-SOUNI,** Chair of the Institute for Materials & Surface Technology IMST, University of Applied Sciences in Kiel, Germany, for the prosperous collaboration we had through Erasmus+ scholarship program.

I would like to acknowledge the valuable discussions with Dr. **Dimitri SCHOPF**, Doctor at the Institute for Materials and Surface Technology, University of Applied Sciences, Kiel, Germany, I am indeed grateful to him for his considerable assistance and for all that I have learned from him in the field of electrochemistry and energy storage Nanocomposite engineering.

I would like to express my deepest love to my dearest parents for their always unconditional love and support during my education and whole life, it is with no doubt because of their high education for me if today I stand at this glamourous point in my life.

I would thank also my two brothers for their kindness, sympathy and enthusiasm, and also my family members for their love and their continued support in everything.

ABSTRACT

Metal oxides show promising electronic properties in energy storage applications. The goal of this thesis would be to develop a composite material associating these oxides, then to explore its electronic and electrochemical performance. In the first part, studying theoretically CuO (II) using the FP LAPW method based on DFT with mBJ corrective approach, and experimentally by the effect of the annealing temperature on the properties of the NPs of the CuO produced by the Solgel method. In the second part, fabricating the CPTNT (CuO / Pt-TiO2) composite material from an initial anodic fabrication of the well-ordered TiO2 NTs, sputtering the Pt NPs followed by electrodeposition of the Cu NPs in the material as obtained, followed by oxidation of the copper by thermal annealing. The electrochemical properties and capacitive behavior of this material are evaluated using cyclic voltammetry (CV), electrochemical impedance spectroscopy (EIS) and chronopotentiometry (GCD). A high specific capacity of 423 F g^{-1} is achieved at a current density of 0.5 A g^{-1}, with long term stability of 93% over 5000 cycles. The results show that this electrode will be able to deliver a high energy density of 19.62 Wh Kg^{-1} and a power density of up to 442.89 W Kg^{-1}. DFT is used to study the electronic structure of TiO2 codoped by (Cu, Pt), in order to better understand its electrochemical behavior. The results obtained throughout this study demonstrate that this new nanocomposite is a notable candidate for high performance supercapacitors.

Keywords: Anodization, Titanium dioxide, CuO, Energy storage, Electrical conductivity, DFT.

RESUME

Les oxydes métalliques présentent des propriétés électroniques prometteuses dans différentes applications comme le stockage d'énergie. Le but de cette thèse serait d'élaborer un matériau composite qui rassemblera ces oxydes, puis d'explorer ses performances électroniques et électrochimiques. D'une part étudier théoriquement le CuO (II) en utilisant la méthode FP LAPW, basée sur la DFT avec l'approche corrective modifiée Becke-Johnson mBJ, et expérimentalement par l'effet de la température de recuit sur les propriétés des NPs du CuO élaboré par la méthode Solgel. D'autre part, fabriquer le matériau composite CPTNT (CuO/Pt-TiO2) à partir d'une anodisation des NTs de TiO2, pulvérisant les NPs du Pt en dessus suivi par une électrodéposition des NPs du Cu dans le matériau, et une oxydation du cuivre par recuit thermique. Les propriétés électrochimiques et le comportement capacitif de ce matériau sont évalués en utilisant la voltampérométrie cyclique (CV), la spectroscopie d'impédance électrochimique (EIS) et les chronopotentiométrie (GCD). Une capacité spécifique élevée de 423 F g^{-1} est atteinte à une densité de courant de 0,5 A g^{-1}, avec une stabilité à long terme de 93% sur 5000 cycles. De plus, les résultats démontrent que cette électrode pourra délivrer une haute densité d'énergie de 19,62 Wh Kg^{-1} et une densité de puissance jusqu'à 442,89 W Kg^{-1}. La DFT est utilisée pour étudier la structure électronique du TiO2 codopé par (Cu, Pt), afin de mieux comprendre ses comportements électrochimiques. Les résultats obtenus tout au long de cette étude démontrent que ce nouveau nanocomposite est un candidat notable pour les supercondensateurs à haute performance.

Mots clés : Anodisation, Dioxide de titane, CuO, Stockage d'énergie, Conductivité électrique, DFT.

RESUME DETAILLE

Le stockage de l'énergie est l'un des grands défis du XXIe siècle, et c'est une solution optimale pour faire face aux fluctuations de la production et à la demande croissante d'énergie et afin de soutenir notre mode de vie moderne. Il existe plusieurs technologies qui sont développées et utilisées comme dispositifs de stockage d'énergie comme les supercondensateurs ou bien condensateurs électrochimiques, ces derniers ont suscité un intérêt considérable de la part des chercheurs en raison de leurs principaux avantages, à savoir une densité de puissance élevée, une excellente capacité de débit [6], une longue durée de vie [7] et une relative stabilité de sa température caractéristique par rapport aux batteries.

Le supercondensateur est capable de stocker de l'énergie en utilisant deux mécanismes de comportement capacitif, les pseudocondensateurs basés sur des réactions d'oxydation – réduction près de la surface et les condensateurs électrochimiques à double couche (EDLC) qui sont fournis par l'accumulation de charge électrostatique à l'interface électrode / électrolyte.

Du point de vue des types de matériaux, les matériaux traditionnels pour les condensateurs électriques à double couche comprennent du carbone à large surface spécifique et des substrats nanostructurés à faible conductivité tels que TiO2 (titane), limitent l'accumulation de la charge stockée au niveau des EDLC électriques à double couche conventionnels, qui conduisent à une réduction de sa propre capacité spécifique à moins de 160 F g^{-1}. [8]

Le dioxyde de titane (TiO2) a été largement étudié et utilisé dans un éventail d'applications industrielles en raison de ses propriétés singulières, notamment un indice de réfraction élevé, une activité photocatalytique et une semi-conductivité. Des efforts considérables ont été consacrés au contrôle de divers paramètres tels que la morphologie, la taille des particules, la cristallinité et la porosité pour des applications spécifiques. Il a été considéré comme un substitut prometteur pour remplacer les anodes en graphite dans les batteries lithium-ion, principalement en raison de sa capacité spécifique théorique compétitive (335,6 mAh.g-1), de son faible coût et de sa bonne stabilité chimique. Néanmoins, TiO2 présente une mauvaise conductivité électronique et un faible coefficient de diffusion ionique ; ces problèmes peuvent être limités en réduisant la distance de diffusion des ions (par exemple en utilisant des structures nanoporeuses). Par conséquent, l'amélioration de la conductivité TiO2 NT est nécessaire pour les matériaux d'électrode de supercondensateur en raison de sa conductivité limitée [10]. Ainsi, les chercheurs se sont concentrés sur l'amélioration de la conductivité électronique du TiO2 (par exemple par dopage d'atomes métalliques) ou sur l'amélioration du transport électronique (par exemple en utilisant des composites carbone-dioxyde de titane).

Les oxydes de métaux de transition (TMO) incluant le MnO2, Co3O4, V2O5, CuO and WO3, etc. [11,12] ont suscité un grand intérêt en tant que matériaux d'électrode de supercondensateur en raison de leurs performances électrochimiques exceptionnelles et de leur variété d'états d'oxydation pour le transfert de charge redox.

Parmi ces TMO, l'oxyde de cuivre Cu(II)O est connu pour ses capacités catalytiques et ses applications prometteuses dans de nombreux domaines (catalyseur, lithium-ion batteries capteurs de gaz).

C'est dans ce contexte que l'objectif de nos travaux était de combiner TiO2 et CuO à la fois pour réaliser un nouveau composite pour électrode de supercondensateurs et pour réaliser l'étude systématique, indispensable pour améliorer la conductivité électrique et les performances de ce nouveau matériau composite et améliorer ses propriétés électrochimiques.

Le premier chapitre délimite les principaux sujets de cette étude en apportant un aperçu général de la littérature sur les concepts et notions essentiels sur les supercondensateurs et leurs types, et donne une brève description de la structure cristalline et des propriétés des matériaux d'électrodes utilisés dans nos travaux (Dioxyde de titane TiO2 et oxyde de cuivre CuO).

Le chapitre II comprend une étude des propriétés électroniques des matériaux utilisés dans nos travaux poursuivie par une description de la synthèse, des caractérisations et une évaluation de leurs performances en utilisant les principales méthodes de caractérisation employées dans ce travail (diffraction des rayons X, spectroscopie UV, cyclage électrochimique… etc).

Le chapitre III résume les idées de base du DFT et contient une brève description de la méthodologie des calculs.

Dans la première partie du chapitre IV, nous exposons les investigations théoriques des propriétés structurelles et électroniques de la supercellule CuO réalisées par la théorie fonctionnelle de la densité (DFT) avec approximation généralisée du gradient (GGA-mBJ) et dans la deuxième partie, nous rapportons la synthèse / caractérisation des CuO NP recuits à différentes températures en analysant leurs propriétés structurelles, électroniques, optiques et photocatalytiques.

Le chapitre V traite de la synthèse et de la caractérisation du CuO / TiO2 (CPTNT) et des résultats de ses propriétés électroniques, optiques et électrochimiques et de ses applications. Enfin, une conclusion générale, qui résume les principaux résultats, obtenus dans ce travail.

Contents

Chapter II: Experimental methodology

Chapter III: Computational methodology

Chapter IV: Structural, optical and electronic properties of copper oxide CuO

Chapter V: Electrochemical study on CuO/Pt-TiO2 composite material

ABBREVIATIONS

Ab-initio	First principle calculations
DFT	Density functional theory
DFT+U	Density functional theory with Hubbard U term
HF	Hartree-Fock
SCF	Self-consistent field
LDA	Local density approximation
LSDA	Local spin density approximation
PBE	Perdew Burke Ernzerhof
GGA	Generalized gradient approximation
FP-LAPW	Full potentiel linearized augmented plane wave
TDOS	Total density of states
PDOS	Partial density of states
BS	Band structure
mBJ	Modified Becke-Johnson
VB	Valence band
VBM	Valence band maximum
CB	Conduction band
CBM	Conduction band minimum
EF	Fermi Energy
Eg	Band gap energy
BZ	Brillouin Zone
RMT	Muffin-Tin Radius
TMO	Transition metal oxide
TiO_2	Titanium dioxide
CuO	Copper oxide
NPs	Nanoparticles
$Cu(CH3COO)_2),H_2O$	Copper acetate monohydrate
NaOH	Sodium hydroxide
FWHM	Full width at half maximum
SAED	Selected area electron diffraction
MAUD	Material analysis using diffraction
NTs	Nanotubes

NH4F	Ammonium fluoride
Na2SO4	Sodium sulfate
XRD	X-ray diffraction
SEM	Scanning electron microscopy
EDX	Energy-dispersive X-ray spectroscopy
XPS	X-ray photoelectron spectroscopy
TEM	Transmission electron microscopy
PTNTs	Pt-TiO2 NTs (Pt sputtered on TiO2 nanotubes)
CPTNTs	CuO/Pt-TiO2 NTs (CuO on Pt sputtered TiO2 nanotubes)
EC	Electrochemical Capacitor
CV	Cyclic voltammetry
GCD	Galvanostatic charge-discharge
EIS	Electrochemical Impedance Spectroscopy

SYMBOLS

$\widehat{\boldsymbol{H}}$	Total Hamiltonian operator
$\boldsymbol{\psi}$	Wave function
$\boldsymbol{\varphi_i}$	Single-particle wave functions
$\boldsymbol{\varepsilon_{xc}[\rho(\vec{r})]}$	Electron density of exchange and correlation
$\boldsymbol{V_{eff}[\rho(r)]}$	Effective potential
$\boldsymbol{V_{xc}[\rho(r)]}$	Exchange correlation potential
$\boldsymbol{V_H[\rho(r)]}$	Hartree potential for electrons
$\boldsymbol{\rho(r)}$	Electronic density
$\boldsymbol{F_{HK}}$	Hohenberg-Kohn functional
$\mathbf{B_0}$	Compression modulus
$\boldsymbol{E(\mathrm{V})}$	Lattice total energy
$\boldsymbol{E_0(\mathrm{V})}$	Lattice total energy at equilibrium
$\mathbf{V}$	Lattice volume
$\mathbf{V_0}$	Lattice volume at equilibrium
$\boldsymbol{n}$	Refractive index
$\boldsymbol{c}$	Velocity of light in free space
$\boldsymbol{R(\omega)}$	Reflectivity
$\boldsymbol{\alpha(\omega)}$	Absorption coefficient
$\boldsymbol{\varepsilon(\omega)}$	Complex dielectric function
$\boldsymbol{\varepsilon_1(\omega)}$	Real part of dielectric function
$\boldsymbol{\varepsilon_2(\omega)}$	Imaginary part of dielectric function
$\boldsymbol{\sigma(\omega)}$	Optical conductivity
$\boldsymbol{S}$	Seebeck coefficient
$\boldsymbol{ZT}$	Figure of merit
$\boldsymbol{\sigma}$	Electrical conductivity
$\boldsymbol{T}$	Temperature
$\boldsymbol{k}$	Thermal conductivity
$\boldsymbol{\beta}$	Line broadening at (FWHM)
$\boldsymbol{\theta}$	Bragg angle
$\boldsymbol{\lambda}$	X-ray wavelength
$\boldsymbol{D}$	Average crystallite size

$\boldsymbol{F(R)}$	Kubelka-Munk parameter
$\boldsymbol{R}$	Reflectance
$\boldsymbol{n}$	Transition nature of sample
$\boldsymbol{h}$	Planck's constant
$\boldsymbol{\nu}$	Frequency of vibration
$\boldsymbol{R}(\%)$	Photodegradation efficiency
$\mathbf{q_e}$	Amount of dye adsorbed at equilibrium
$\mathbf{q_t}$	Amount of dye adsorbed at time t
$\boldsymbol{A/A_0}$	Absorbance of dye at time t/at t=0
$\boldsymbol{C/C_0}$	Concentration of dye at time t/at t=0
$\mathbf{C}$	Theoretical specific capacity
$\mathbf{q}$	Charge transferred
$\mathbf{V}$	Applied voltage
$\boldsymbol{C_{sp}}$	Specific capacitance
$\boldsymbol{I}$	Charge-discharge current
$\boldsymbol{\nu}$	Scan rate
$\boldsymbol{\Delta t}$	Discharge time
$\boldsymbol{\Delta V}$	Potential window
$\boldsymbol{m}$	Active material mass
$\boldsymbol{E_c}$	Energy density
$\boldsymbol{P_s}$	Power density
$\boldsymbol{R_{ct}}$	Charge–transfer resistance
$\boldsymbol{Z(t)}$	System impedance

LIST OF FIGURES

Chapter I

Introduction and state of art

I.1 Introduction and scope of the thesis

In the past several decades, the global economy developed rapidly as well as the world population, which resulted in a strong demand for energy. Since the global energy consumption is increasing continuously due to human civilization, which causes fossil-fuel shortage and ecological deterioration, the exhaustion of this global energy will soon threat human society in the near future. Due to a massive use of these fossil fuels, our society is facing a huge depletion of their reserves, which significantly increase the greenhouse gas content [1], in particular, the carbon dioxide CO2 [2]. Thus, renewable energy sources such as solar, tide and wind become either a viable alternative or a supplement to fossil fuels and nuclear energy. An important intermediate step between these energy resources and versatile energy applications is energy

storage, which attracts a lot of attention in academia and industry [3]. Hence, energy storage is one of the great challenges in the twenty-first century with its importance of storing energy to cope with production's fluctuations and the growing demand of energy [4]. To provide optimum energy requirement for the rapidly developing global economy, we are in need of the promising energy sources and at the same time, those sources must be non-polluting, sustainable and environmental friendly, simultaneously, this development will help to overcome the problem of the depletion of fossil fuels. There are several technologies, which are developed and used as devices for energy storage. One can list the prominent technologies, which are dedicated to the energy conversion and storage called as electrochemical devices. For this purpose the use of the high-energy storage devices such as the fuel cells and the batteries being used till last decade.

Among the various energy storage devices, supercapacitors, called electrochemical capacitors have gained considerable interest from researchers owing to their main advantages, i.e., high power density, fast charge–discharge [5], excellent rate capability [6], a long cycle life [7] and a relative stability of its temperature characteristics with respect to the batteries. Supercapacitor is able to store energy by using two mechanisms of capacitive behavior, Pseudocapacitors based on near-surface oxidation–reduction reactions and electrochemical double layer capacitors (EDLC) which are provided by electrostatic charge build-up at the electrode/electrolyte interface.

By material types point of view, traditional materials for electrical double layer capacitors include high specific area carbon and nanostructured low conductive substrates such as TiO2 (titania), limit the accumulation of the stored charge at the conventional electric double layer EDLCs, which lead to a reduction of its own specific capacity to less than 160 F g^{-1}.[8]

Titanium dioxide (TiO2) has been widely studied and employed in an array of industrial applications due to its singular properties including high refractive index, photocatalytic activity, and semiconductivity. Considerable efforts have been devoted to controlling various parameters such as morphology, particle size, crystallinity and porosity for specific applications. It has been considered as a promising substitute to replace graphite anodes in lithium-ion batteries, mainly due to its competitive theoretical specific capacity (335.6 $mAh.g^{-1}$), low cost and good chemical stability. Nevertheless, TiO2 presents poor electronic conductivity and low ion diffusion coefficient; those issues can be limited by reducing the distance of ions diffusion (e.g. by using nanoporous structures). TiO2 nanotubes arrays have

been used for electrochemical capacitor applications [9]. Therefore, TiO2 NTs conductivity improvement is needed for supercapacitor electrode materials because of its limited conductivity [10]. Thus, the researchers have focused on improving the electronic conductivity of TiO2 (e.g. by metal atoms doping) or improving the electronic transport (e.g. by using carbon-titania composites).

Transition metal oxides (TMOs), including MnO2, Co3O4, V2O5, CuO and WO3, etc. [11,12] has attracted great interest as supercapacitor electrode materials because of their outstanding electrochemical performance and their variety of oxidation states for the redox charge transfer. Among these TMO, copper oxide Cu(II)O, has been known for its catalytic capabilities and its promising applications in many fields including catalyst, lithium ion batteries and gas sensor [12, 13]. It is in this context that the aim of our work was to combine TiO2 and CuO both to make a new composite for supercapacitors electrode and to carry out the systematic study, which is essential to improve the electrical conductivity and performance of this new composite material and enhance its electrochemical properties.

The first chapter delimits the main topics of this study by bringing a general literature overview of the essential concepts and notions about supercapacitors and its types, and gives a brief description on crystal structure and properties of electrode materials used in our work (Titanium dioxide TiO_2 and copper oxide CuO). Chapter II includes a study of electronic properties of materials used in our work pursued by a description of the Synthesis, characterizations and evaluation of their performances using the principle of the main characterization methods employed in this work (i.e.c X-ray diffraction, UV spectroscopy, electrochemical cycling…etc). Chapter III resumes the basic ideas behind the DFT and contains a brief description of the methodology of calculations.

In the first part in chapter IV, we are exposing the theoretical investigations of the structural, and electronic properties of CuO supercell carried out by density functional theory (DFT) with generalized gradient approximation (GGA-mBJ) and in the second part, we report the synthesis/characterization of CuO NPs annealed at different temperatures by analyzing their structural, electronic, optical and photocatalytic properties. Fifth chapter discusses the synthesis and characterization of CuO/TiO2 (CPTNTs) and discusses the results of its electronic, optical and electrochemical properties and its applications. Finally, a general conclusion, which summarizes the main results, obtained in this work.

I.2 Energy-storage devices

Generally, Energy is able to be stored electrostatically in conventional capacitors, or electrochemically either in cells or batteries (electrochemical power sources). Among all, electrochemical energy storage and conversion technologies, such as batteries, fuel cells and supercapacitors are some of emerging fields to meet energy demands and each of them has its unique merits and become complement or supplement to each other [14]. Batteries and fuel cells rely on the conversion of chemical energy into electrical energy.

The energy density and power density comparison of various energy conversion and storage devices is presented in the simplified Ragone plot, as depicted in Figure 1.1 supercapacitors occupy an important position in terms of the specific energy as well as the specific power. With a high power capability and relatively large energy density compared to conventional capacitors, supercapacitors offer a promising approach to meet the increasing power demands of energy storage systems in the next days. Because of the advantages of supercapacitors, they can replace conventional batteries or even novel energy storage devices utilized in electrical vehicles [15]

Supercapacitors have more widespread applications than traditional batteries and is one of the emerging energy storage device to meet all technical and economical amenities. Therefore, many researchers are sparing no efforts to study the electrode materials of supercapacitors.

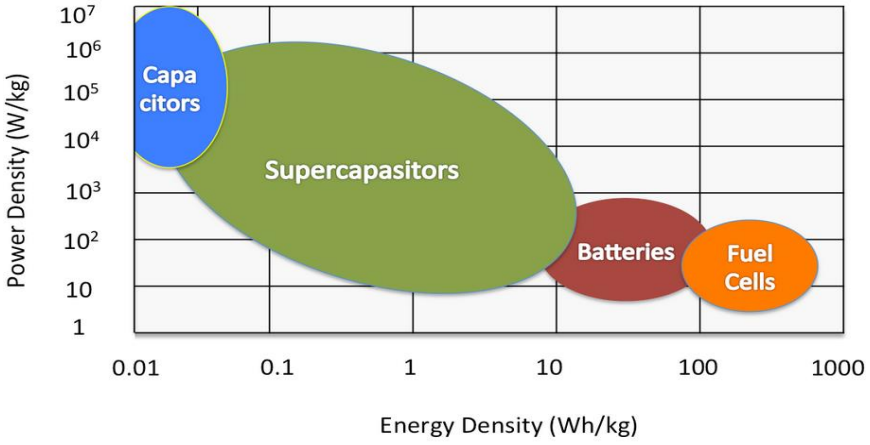

Figure I.1: *Ragone plot of energy density vs. power density for various energy-storing devices. [16]*

I.3 Supercapacitors

A supercapacitor (SCs), also known as electrochemical capacitor (ECs) have many advantages [17]. The most intriguing one is that they can store an extremely high amount of energy, and discharge that energy at rates demanded specifically by the application, which can lead to an ultrahigh power density resulting from the fast charge-discharge [18]. Besides, the long cycle life, 100-1000 times longer than batteries, inevitably earns itself an important place in all of the energy storage devices [19]. Moreover, simple principle and relatively cheap materials simplify the application and reduce the cost. Another important advantage of ECs is that in general, they do not contain hazardous or toxic materials and that they are easy to dispose. All of the abovementioned assets open various directions for the applications of supercapacitors.

A supercapacitor consists of two electrodes impregnated by an electrolyte and separated by an insulating and porous membrane, the separator (Figure 4.3). Under the effect of an electric field, the ions of the electrolyte will interact with the electrodes. The anions and cations will move respectively to the positive and negative electrodes. Thanks to this surface phenomenon, the supercapacitor can charge and discharge in a very fast manner (a few seconds to a few minutes), unlike batteries, which store energy via slower redox reactions (several hours). Supercapacitors therefore have a higher power density than batteries (> 2000 W / kg vs <1000 W / kg for batteries) but a lower energy density (<10 Wh / kg vs 20-150 Wh / kg for batteries) [20]. (Figure I.1)

The key for increased energy density of supercapacitors resides on the electrode material. Currently, the development of new electrodes for enhanced energy density supercapacitors are receiving considerable attention, with some promising results being available.

However, to achieve more promising energy density and power density, supercapacitors still need to be improved. The key to this is improving fundamental understanding of the processes in supercapacitors and their electrode materials.

Thus, this PhD dissertation aims at contribution for this crucial objective by delivering novel electrode materials characterized by increased energy storage performance.

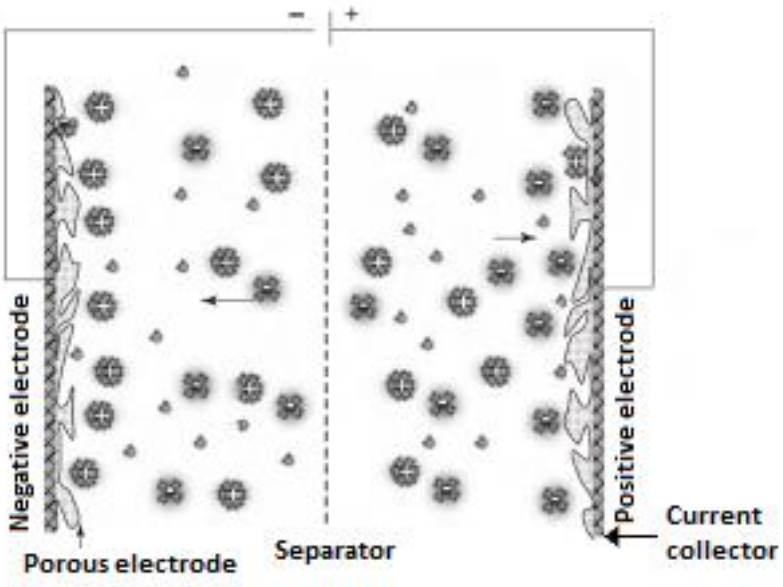

Figure I.2: *Diagram of a supercapacitor. Adapted from [20].*

I.4 Types of Supercapacitors

Based on the energy storage mechanism, supercapacitors can be classified into two categories. One is the electrical double layer capacitor (EDLC), where the capacitance comes from the pure electrostatic charge accumulated at the electrode/electrolyte interface; therefore, it is strongly dependent on the surface area of the electrode materials that is accessible to the electrolyte ions. The other category is the pseudocapacitor, in which fast and reversible faradic processes take place due to electro-active species [21]. Hybrid supercapacitors are the combination of both EDLSC and pseudocapacitor. These supercapacitors are capable of accumulating extremely high amounts of charge and hence these kinds of supercapacitors are called as high-energy storage devices are detailed classification of supercapacitors as follows Figure I.3.

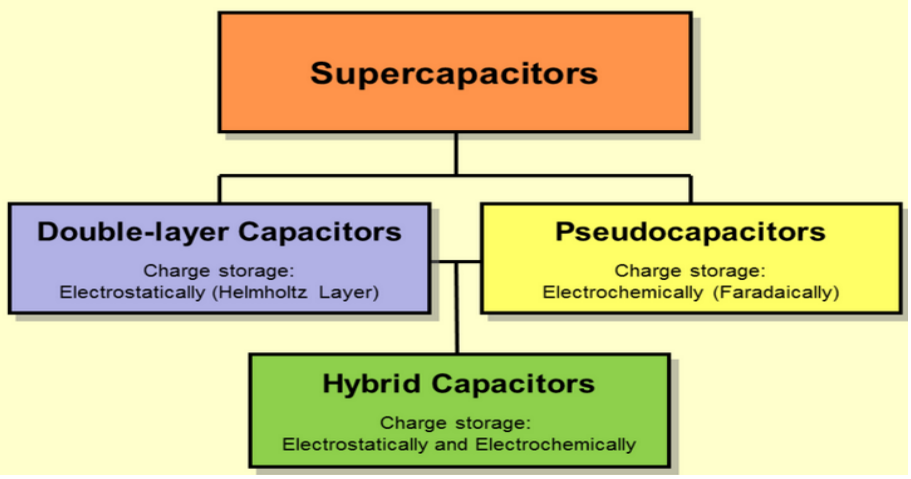

Figure I.3: *Supercapacitor types: electrochemical double-layer capacitors and pseudocapacitors as well as hybrid capacitors. Adapted from [22].*

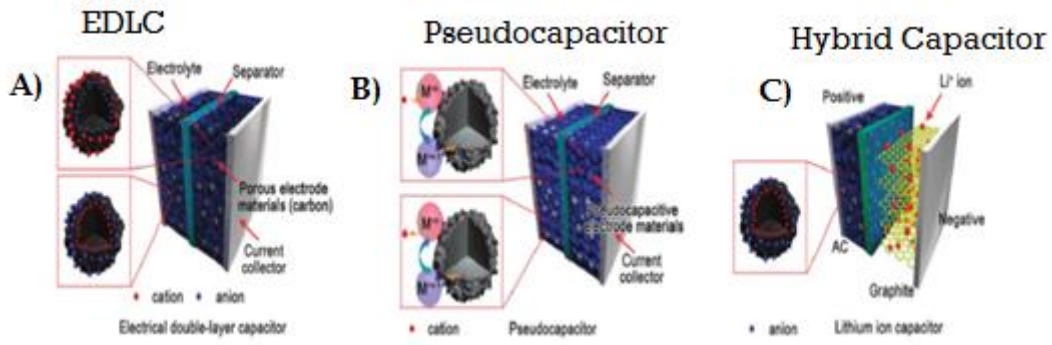

Figure I.4: *Supercapacitor configuration of EDLC A), pseudocapacitors B) as well as hybrid capacitors C). Adapted from [23].*

I.4.1 EDLC

Electrochemical Double Layer Capacitor (EDLC) have a relatively simple energy storage mechanism among the different categories of supercapacitors. Double Layer Capacitor (EDLC) are similar to electrostatic capacitors in terms of the energy storage mechanism, the charges are accumulated on the electrode surfaces during charging. Opposite charged ions in the electrolyte solution diffuse into the pores of the charged electrode. Thus, a double-layer of charge is produced at each electrode surface. These double-layers, along with its large electrode material surface area, allow EDLCs to achieve much higher specific energy densities than conventional capacitors [24, 25].

EDLCs can accumulate more energy due to capacitance improvement. The increase in capacitance comes from the porous structures of the electrode materials that increase the contact area. Electrode materials are often composed of carbon with high porosity such as activated carbon, air gel carbon, graphene, carbon nanotubes ... etc. The configuration of the EDLCs is shown in Figure I.5. Nowadays, EDLCs are presented as a mature technology. Their use is the most widespread among all the supercapacitors available on the commercial market. The energy density of these devices does not exceed 10 W h kg^{-1}, but their power is around 10^3 to 10^5 W kg^{-1}. [26]

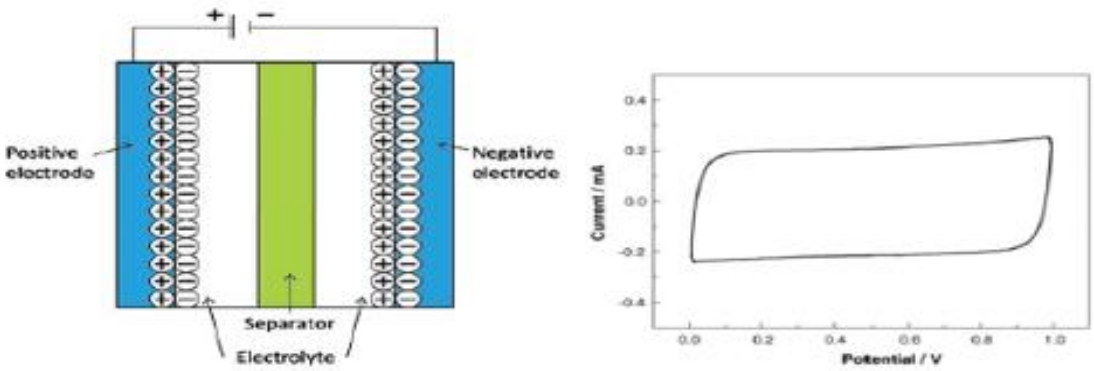

Figure I.5: *EDLC diagram and its corresponding voltammogram, taken from [27, 28]*

I.4.2 Pseudocapacitors

Pseudocapacitors are faradic in origin, quite different from the classical electrostatic capacitance observed in the double layer, and it helps to increase the charge storage capacitance in supercapacitor shown Fig.1.6. Pseudocapacitors stores energy by means of fast and reversible redox reaction between the electrodes and electrolytes. Faradic reactions are allowed by the addition of electroactive materials (redox), these electroactive materials may be added to the electrodes or dissolved in the electrolyte.

In the case of electrodes, electroactive materials are often transition metal oxides, [29] such as Ruthenium oxide RuO2 [30] Manganese oxide MnO2 [31], Fe2O3 and NiO [32], electrically conducting polymers such as polyaniline [33]. The energy density for pseudocapacitor can reach values greater than 50 Whkg-1 and powers ~ 103 Wkg-1 [34, 35].

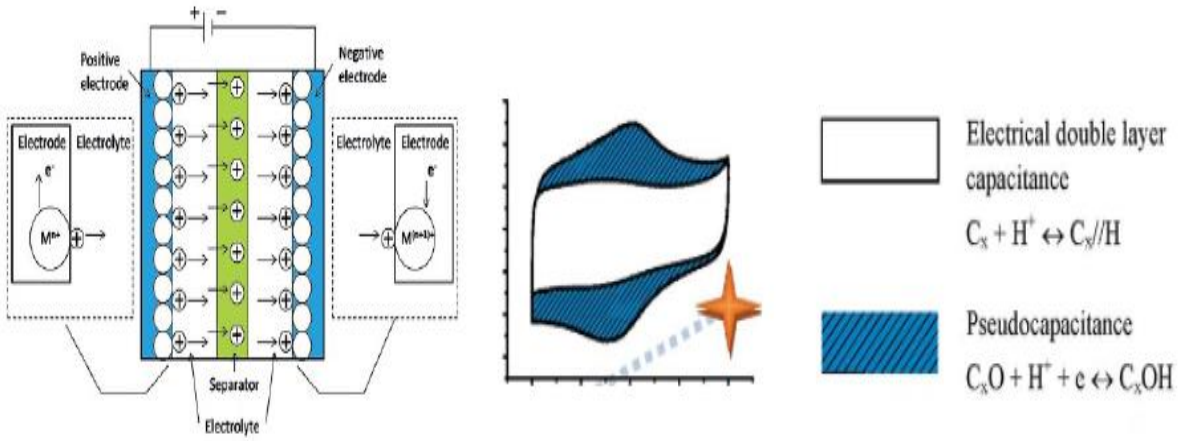

Figure I.6: *Pseudocapacitor diagram and its corresponding voltammogram, adapted from [36, 37]*

I.5 Basic definitions and electrochemical concepts

I.5.1 Capacitance:

Capacitance is an important parameter to evaluate active materials and determine the ability of a material to store an electric charge. The theoretical specific capacity (C) can be calculated from Eq. (I.1), based on the total amount of charge transferred (q) as a voltage is applied to the plates (V):

$$C = \frac{q}{V} \qquad \text{(I.1)}$$

Therefore, specific capacitance can be calculated based on the amount of charge transferred per unit mass (F g^{-1}) or specific surface area of the electrode (F cm^{-2}), according to Eq. (I.2) :

$$C_s = \frac{I * \Delta t}{\Delta V * m \ (or\ s)} \qquad \text{(I.2)}$$

where, C_s is the specific capacitance (F g^{-1}), I is the charge-discharge current (A), m is the active material mass (g), s is the specific surface area (cm^2), ΔV is the potential window (V), and Δt is the discharge time (s).

I.5.2 Energy density:

Energy density is a term used for the amount of energy stored in a given mass of the system (Wh kg^{-1}) or region of space per unit volume (Wh L^{-1}). It determines the supercapacitor weight or size required to achieve a given performance target. It can be calculated using the following equation Eq. (I.3):

$$E_c = \frac{1}{2} * C_s * \Delta V^2 \quad \text{(I.3)}$$

I.5.3 Power density:

Power density is the abilities of the cell to transfer energy in unit time (h) per unit mass of the system (W kg^{-1}) or unit volume (W L^{-1}) (Eq. I.4):

$$P_s = \frac{E_s}{\Delta t} \quad \text{(I.4)}$$

I.5.4 Cycle life:

This term refers to the number of charge-discharge cycles which electrochemical supercapacitors or batteries can experience before they fail to meet a specific performance criterion.

I.6 Supercapacitors electrode materials

Transition metal oxides (TMOs) are widely studied as the electrode materials for supercapacitors because of their high pseudocapacitance and better cycle stability compared to conductive polymers. As faradaic materials, TMOs have two or more oxidation states in the same phases. When charging and discharging take place, TMOS are able to convert between different oxidation states and protons can insert into and extract from the oxide lattice during reduction and oxidation. The redox reactions are fast and reversible, since no phase changing occurs in the process. Several TMOs such as RuO2 [30] MnO2 [31], V2O5 [38], NiO [39] and Co3O4 [40], have been found to have the above properties and been tested as supercapacitor electrode materials.

Specific capacitance of more than 1500 F.g-1 has been reported [41], but Ru-based electrode are expensive, and small voltage window also limits their applications [29, 42, 43]. So instead of ruthenium-oxides, other metal oxide systems have also been tested as possible electrode materials for supercapacitor, such as NiO [39], Co3O4 [40], MnO2 [31], TiO2 [45] and CuO [46].

I.7 Copper (II) oxide (CuO)

I.7.1 Crystallographic structure:

CuO or tenorite oxide is distinguished from the transition metal monoxides 3d by its monoclinic structure. It is a black ionic solid having as melting and evaporation temperature 1064 and 1100°C respectively. In this structure, copper is located in the center of square planes defined by oxygen anions (Figure I.7). Tenorite crystallizes in the C2/c space group with mesh parameters defined in Table I.1.

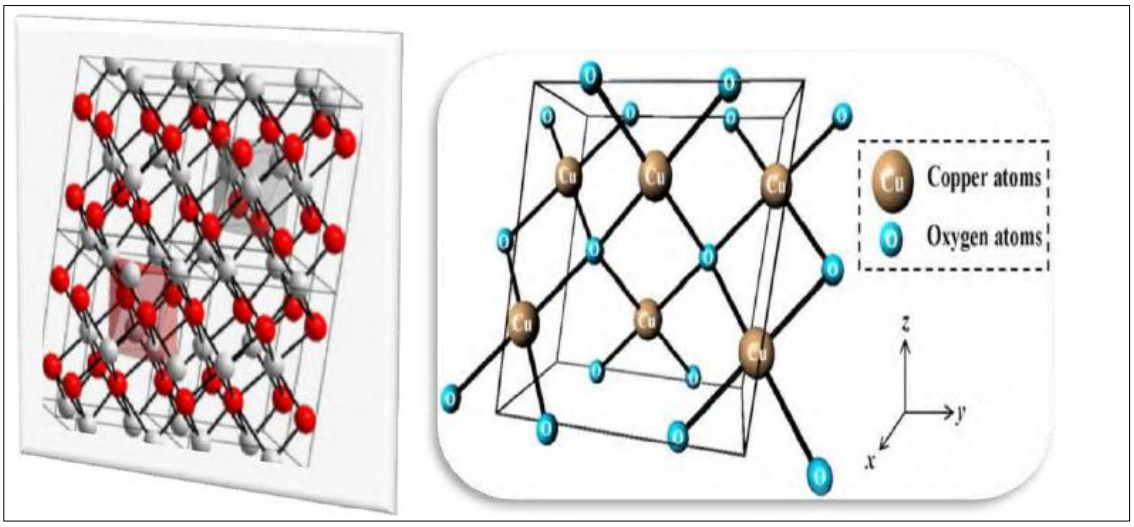

Figure I.7. *Schematic representation of the crystallographic structure of CuO: gray spheres represent the Cu2+ ions and red spheres the O2- ions* [47].

Table I.1: *Crystallographic data of the CuO tenorite.*

	CuO
Space group	C2/c
Lattice parameters (Å)	a = 4.6883 b = 3.4229 c = 5.1319 β = 99.54°
Volume (Å^3)	81.08
Molar volume (cm^3.mol^{-1})	12.21
Density (g.cm^{-3})	6.505
Z	4
Interatomic distances (Å)	d_{Cu-O} =1.96 d_{O-O} = 2.62 d_{Cu-Cu} = 2.90

The elemental cell of CuO (a = 4.6837A °, b = 3.4226A °, c = 5.1288A °, = 99.54 °) [48-49] comprises Cu^{2+} ions coordinated by four (4) O^{2-} ions in an approximately square planar configuration.

I.7.2 Electronic and optical properties:

Copper oxide CuO is considered as a "p" type semiconductor because of the presence of acceptor levels attributable to copper gaps, it has a band gap that can vary depending on the mode of preparation between 1 eV to 2 eV [50, 51, 52].

However, experimentally, the exact value of the band gap and the direct or indirect character of the band transition are not yet determined with certainty. In addition, by calculation by means of the DFT, it is found that the CuO has an indirect gap between the points Γ (0 0 0) and C (0 ½ ½).

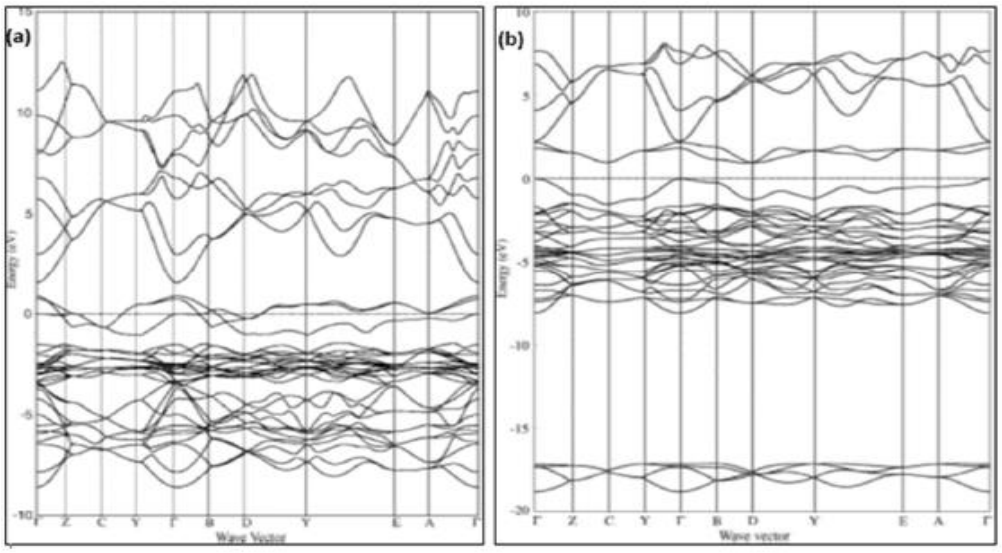

Figure I.8: *Electronic band structure and density of states for CuO calculated by the DFT* [52].

Evaluation of the refractive indices of optical materials is considerably important for applications in integrated optic devices, such as switches, filters, and modulation, among others, in which η is a key parameter for the device design [53]. The refractive index of CuO at a

nanoscale has a value that is between 1.90 and 2.4 depending on transparency of the semiconductor to incident spectral radiation.

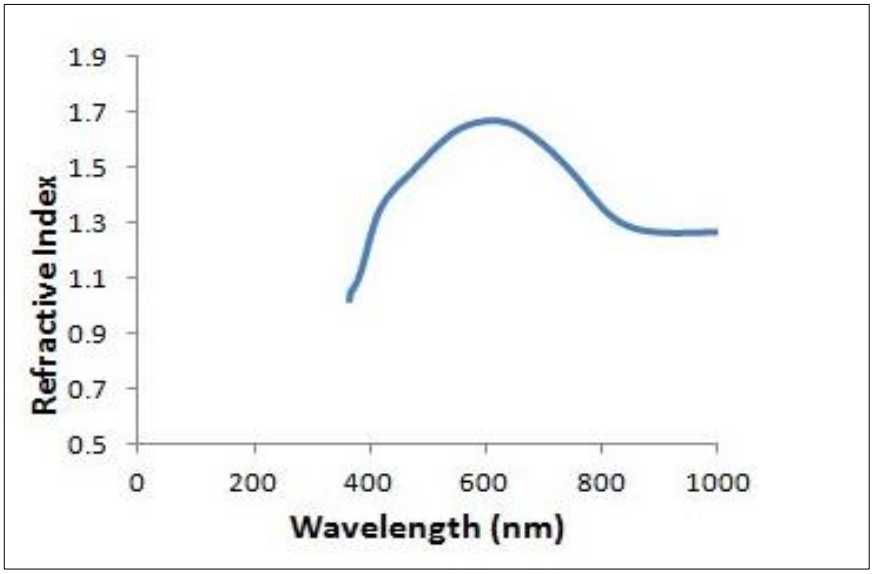

Figure I.9: *Refractive index against wavelength of CuO thin film* [54]

Understanding the optical properties of CuO nanostructures is very important in their applications in electronic and optical devices.

I.7.3 Broad range of CuO applications

I.7.3.1 Photocatalytic applications

Organic dyes are extensively used for various industrial applications including textile dyeing, photographic, coating and photochemical industries. Most of the dyes used as coloring materials are toxic to aquatic organisms. The pollutants can be effectively removed from wastewater by the photocatalytic process using semiconductor photocatalyst. Among several metal oxides, CuO is one of the suitable photocatalyst for this purpose, because of its photocatalytic activity, reusability, nontoxicity and other properties. It is used also to degrade many dyes and chemicals

I.7.3.2 Supercapacitors

Electrochemical capacitors, also known as supercapacitors (SCs) or ultra capacitors are promising energy storage systems as they bridge the gap between traditional dielectric capacitors and chemical batteries. Supercapacitors are particularly useful in applications requiring fast charge/discharge rates such as power backup for electronic devices, cell phone

cameras, regenerative braking and hybrid electric vehicles. Metal oxides often exhibit higher specific capacitances and electrochemical stability than most conductive polymers, so they are preferred electrode materials for building high-energy supercapacitors. Copper oxide (CuO) is a promising candidate due to its, easy preparation in various shapes at the nanoscale and good electrochemical performance. For example, Wang et al., [55] synthesized nanosheet arrays of CuO on nickel foam with a high specific capacitance of 569 F/g in KOH electrolyte; however, the method employed is relatively complex and the yield is quite low.

I.7.3.3 Anticancer agent

The anticancer activity of CuO had reported by the report they said that nanostructures depends on the level of reactive oxygen species (ROS) production which is dependent on the presence of defects sites in the metal oxide crystal structure. The white light can generate electron hole pair in CuO by exciting the valance band electrons to conduction band. These holes in the valance band are migrated to the surface of the nanostructures and interacted with water molecules which lead to generate hydroxyl radicals (OH). On the other hand, the photo-generated electrons are reached the surface which interacts with adsorbed oxygen molecules to form oxygen radicals after interacting with H+ ions and generate H2O2. These free radicals induce damage to the cellular components like DNA, lipids and proteins of the cancer cells and cause their death through apoptosis [56].

I.7.3.4 Solar cell observers

In the context of the developing of energy saving technologies, much attention has been devoted to the selective absorbers of electromagnetic radiation and the related alternative energy sources, in particular, to thermal converters of solar energy, which employ coatings based on such selective absorbers. The selective solar energy absorbers must obey certain requirements. These materials should possess a large absorption coefficient (α) and a small reflection coefficient (R) in the photon energies $E > 0.5$ eV, on the one hand, and exhibit low emission or high reflection in the IR spectral range at $E < 0.5$ eV. In other words, a selective monoabsorber (i.e., an absorber based on a single component) must exhibit a strong absorption of radiation of the given source at a minimum level of the energy reradiated to the atmosphere in the IR range. These conditions could be satisfied by solar energy absorbers with an optical gap width of Eg ~ 0.5 eV and a small refractive index n in the IR range. It was suggested to use various copper compounds as selective absorbers of solar energy operating at $T < 500°C$. [57].

I.8 Anatase Titanium dioxide (TiO2)

Among the various wide-band-gap oxide semiconductors, titanium dioxide (TiO_2) is a very attractive candidate electrode material that is used in a broad range of electrochemical applications because it is non-toxic, environmentally friendly, low-cost, and has excellent chemical and photochemical stability.

Titania has three common polymorphs: rutile (tetragonal), anatase (tetragonal), and brookite (orthorhombic). The structure of the three main phases is well characterized by TiO_6 octahedron building blocks, as illustrated in Figure. I.10. All these three crystal forms are wide- band-gap (E_g 3 eV) semiconductors [58-63].

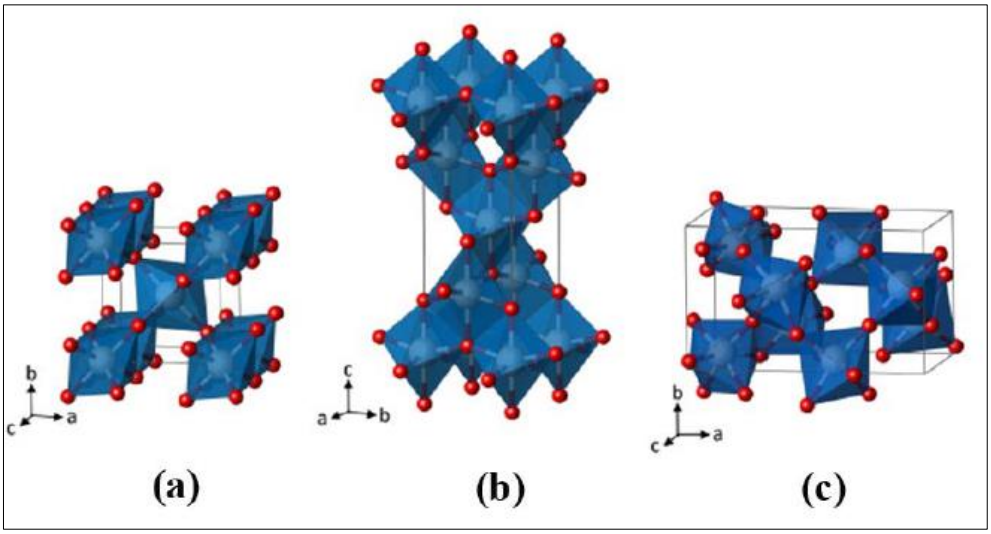

Figure I-10: *Three different polymorphs of titanium dioxide: (a) rutile, (b) anatase and (c) brookite.* [63]

Most preferred form of TiO2 is anatase phase due to their nature of strong photoactive and high electron mobility, prime reason to be used in DSSC and photocatalysis applications [64, 65].

I.8.1 crystal structure

For the allotropic forms of titania, their structural difference generally lies in the way of the connectivity of TiO6 octahedra subunits where each titanium is octahedrally surrounded by six oxygen atoms. Depending on the crystal structure, TiO6 octahedra are connected by a various number of corner, edge and/or face-sharing.

The crystal parameters of TiO2 anatase are gathered in **Table I.2**. TiO2 anatase crystallizes in a tetragonal cell with a space group of I_{41}/amd. The unit cell contains 4 formula units, i.e. 12 atoms (**Figure I.11a**). TiO2 anatase involves one cation site for Ti and one anion site for O with multiplicities of 4 and 8, respectively. TiO2 anatase consists of distorted TiO6 octahedra sharing four edges. Two different Ti-O distances can be distinguished. Larger distance (1.964 Å) originates from two Ti-O bonds along c-axis, while shorter distance (1.937 Å) comes from four Ti-O bonds at (ab) plan. Each oxygen atom is coordinated with three titanium atoms. The 3D anatase network is formed by the stacking of zigzag chains along the c-axis (**Figure I.11b**). The stacking mode for anatase results in a density of ca. 3.9 g/cm3, which is lower than rutile and brookite. It means that, anatase shows larger area for same weight of material, indicating a higher degree of structural openness. Moreover, the stacking of zigzag chains creates vacant sites which are able to accommodate heteroatoms, i.e. intercalation properties.

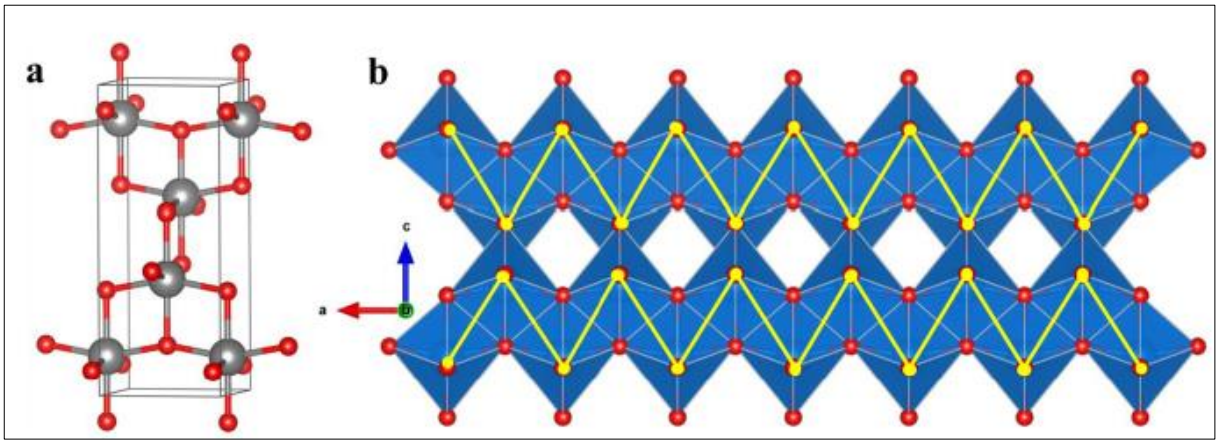

Figure I.11: *Structural representation of TiO2 anatase: (a) ball-stick configuration of a unit cell, (b) extended unit cell showing the connectivity of TiO6 octahedra (Grey: Ti, red: O).*

Table 1.2: *Crystal structure information of TiO2 anatase (Reference: ICSD #44882).*

Crystal system	Space group	Lattice constant (Å)	Volume (Å^3)	d_{Ti-O} (Å)	Density (g/cm^3)	Atomic positions				
						Atoms	Site	x	y	z
Tetragonal	$I4_1$/amd	a=b=3.785 c=9.514	136.3	2*1.964 4*1.937	3.88	Ti	4a	0	0	0
						O	8e	0	0	0.2064

I.8.2 Electronic structure

Figure 1.2 presents the molecular-orbital bonding diagram of TiO_2 anatase [66]. It shows that the upper valence band (VB) are dominantly composed of 2p orbital of oxygen atom. 3d orbital of titanium atom are mainly located at the bottom of conduction band (CB). For pure TiO2 anatase, the energy gap Eg between the top of VB and the bottom of CB is 3.2 eV. This value of band gap induces adsorption of photon below wavelength of ca. 380 nm. Consequently, TiO2 is a white powder. It can absorb the light in the ultraviolet region, making it a good candidate as UV absorber and providing applications in cosmetics.

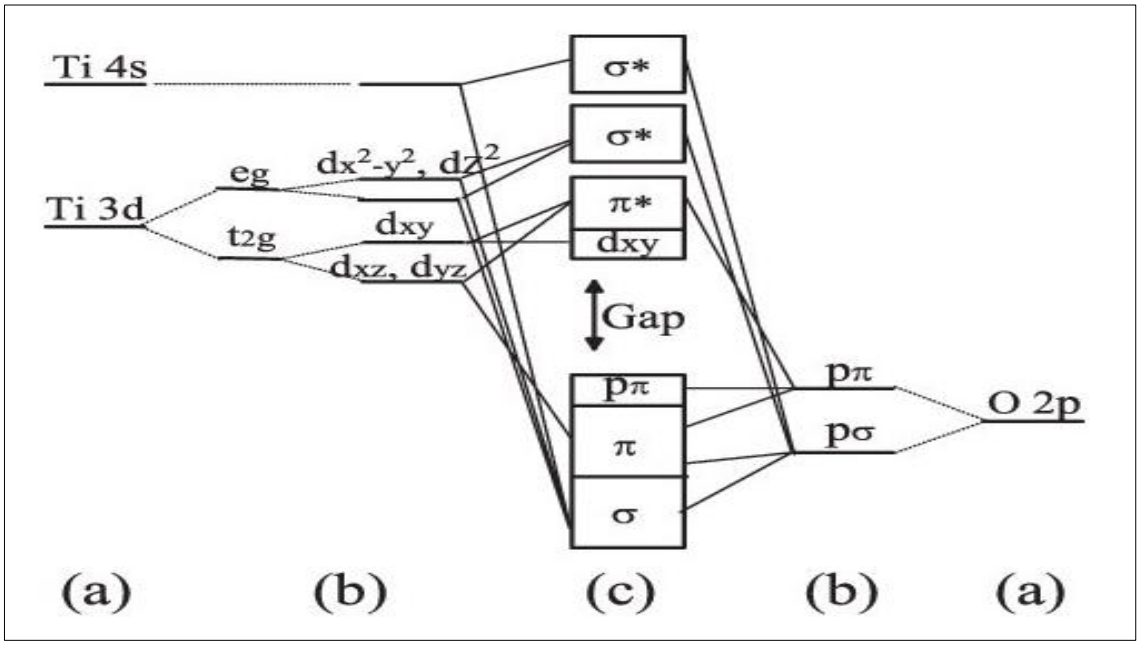

Figure I.12. *The molecular-orbital bonding diagram for pure anatase TiO2: (a) atomic states, (b) crystal field split states, (c) final states. O p σ and O p π are the oxygen 2p states in and out of the Ti 3 O plane, respectively.* [66]

I.8.3 Applications of Titanium dioxide:

I.8.3.1 Dye sensitized Solar Cells [DSSCs]

Dye sensitized solar cells are based on a semiconductor formed between a photo sensitized anode and an electrolyte. TiO2 semiconductors are widely studied as an efficient candidate in dye sensitized solar cells [180].

DSSCs generated from semiconductor nanostructures such as nanorods, nanowires, and nanotubes are of great relevance because direct connection of the point of photo generation with the collection electrode using such structures may improve the cell performance. Recently nanostructured TiO2 are used in DSSCs for improving the performance [180]. DSSCs made from TiO2 nanotubular structure show much higher efficiencies as compared to other structures [65].

I.8.3.2 Photocatalysts

Light-facilitated chemical reactions are referred as photo catalytic. High photo activity, low cost and high stability makes TiO2 an efficient material for photo catalysts [178]. TiO2 adsorbs the reactants on its surface, with the energy supplied from the electromagnetic radiation (photons) and facilitates the reaction between the adsorbed reactants. Photocatalytic oxidation (PCO) with UV light rays and TiO2 coated filter creates hydroxyl radicals and super-oxide ions, which are highly reactive electrons. These highly reactive electrons aggressively combine with other elements in the air, such as bacteria and Volatile Organic Compounds (VOC), which include harmful pollutants such as formaldehyde, ammonia and other common contaminates released by building materials and household cleaners. Once bound together, the chemical reaction takes place between the super-charged ion and the pollutant. Thus, the pollutant breaks down into harmless carbon dioxide and water molecules, which make the air more purified.

TiO2 has been most commonly studied photocatalysts due to its ability to break down organic pollutants and even achieve complete mineralization among various photoactive semiconductors like ZnO, Fe2O3, CdS, ZnS etc.

Photo catalytic and hydrophilic properties of TiO2 make it close to an ideal catalyst. Owing to their high photo catalytic activity, strong oxidizing ability coupled with chemical inertness and unique optical properties, the nano materials based on the titanium dioxide are able to revolutionize the creation of various electro-optical and electro-chemical systems that can be used as efficient power sources, gas sensors, which are operating at high temperatures devices

for the decomposition of water using solar energy, nanofilters for air purification and carbon dioxide consumption.

I.8.3.3 Controlling environmental pollutants

Rapid urban development causes terrific air pollution and it becomes a great threat in our society. TiO2 based photo catalysts are used to combat air pollution [116, 117]. TiO2 when exposed to sunlight convert air pollutants such as nitrogen oxides (NOx), volatile organic compounds (VOCs), carbon monoxide (CO), and ozone to more environmentally acceptable products such as calcium nitrate and carbon dioxide. In Japan, air purifiers equipped with TiO2 coated filters are very popular for indoor air treatment. TiO2 based paint is used for the self-cleaning purpose.

I.8.3.4 Wastewater purification

Like air pollution, another serious environmental problem that the modern society faces is water pollution. According to official reports of some countries, 41.3% of the United States' water is polluted. TiO2 becomes superior in water purification as in air purification. Various studies have been reported on the photo degradation of the organic compounds present in industrial wastewater using TiO2 semiconductor as photo catalyst [227, 228].

In recent years, photocatalytic degradation mediated by illuminated TiO2 has received considerable attention for treating polluted water. The semiconductor photocatalytic process is based on aqueous phase hydroxyl radical chemistry and couples low energy UV. It has been proved that this process can degrade many toxic compounds in wastewater into carbon dioxide and water.

I.8.3.5 Cosmetics

UV light causes sunburns and skin cancer after prolonged exposure. Sunscreens have the benefit of protecting consumers from the UV light. Most frequently used materials in these cosmetics items are TiO2 and ZnO2 [229,230].

Chapter II

Experimental methodology

II.1 Elaboration and synthesis of nanomaterials

The formation of metallic or semiconducting nanoparticles in aqueous solution by the various synthesis processes is based on the nucleation of the solid phase in the solution. The constituent elements of the particle have stronger interactions with each other than with the solvent from which they tend to separate.

In a solution, the presence of a solute in a concentration greater than the solubility leads to the formation of molecules, their combination into particles and the precipitation of these. However, the formation of small nanoparticles with a narrow size distribution in solution requires special experimental conditions.

Although the nanoparticles formed in aqueous solution are very small crystallites, they tend to evolve rapidly to the massive state because they are thermodynamically unstable toward growth. The formation of nanoparticles of controlled size can only be possible if complexing agents or ligands, inorganic or organic, can protect the surfaces and prevent the growth of particles.

Numerous methods have been recently developed to synthesize various CuO nanostructures with diverse morphologies, sizes, and dimensions using various chemical and physical strategies, among them, Solgel method, which we chose in our work.

II.1.1 Sol-gel method

Sol-gel syntheses (production of a gel from powder-shaped materials) are wet-chemical processes for producing porous nanomaterials, ceramic nanostructured polymers as well as oxide nanoparticles.

Sol-gel can be defined as a process in which solid nanoparticles dispersed in a liquid (sol) agglomerate together to form a continuous three-dimensional network extending throughout the liquid (a gel). The idea behind it is to “dissolve” the compound in a liquid in order to bring it back as a solid in a controlled manner.

In sol-gel processes, material production or deposition takes place from a liquid sol state, which is converted into a solid gel state via a sol-gel transformation.

To start with, adding organic substances in the sol-gel process produces an organometallic compound from a solution containing an alcoxide (they are typical precursors). The pH value of the solution is adjusted with an acid or a base which, as a catalyst, also triggers the transformation of the alcoxide.

The subsequent reactions are hydrolysis (splitting of a chemical bond by water) followed by condensation and polymerization (reaction giving rise to many- or long-chained compounds from single-chained ones). The particles or the polymer oxide grow as the reaction continues, until a gel is formed.

These reactions are defined below:

- **Hydrolysis of the alcohol group**

$$M - OR + H_2O \longrightarrow M - OH + ROH \quad \text{(II.1)}$$

- **Condensation of the resulting hydroxyl group**

$$M - OH + M - OR \longrightarrow M - O - M + ROH \quad \text{(II.2)}$$

$$M - OH + M - OH \longrightarrow M - O - M + H_2O \quad \text{(II.3)}$$

The course of hydrolysis and the polycondensation reaction depend on many factors: the composition of the initial solution, the type and amount of catalyst, temperature as well as the reactor- and mixing geometry. For coatings, the alcoxide initial solution of the sol-gel process can be applied on surfaces of any geometry. After the wetting, the build-up of the porous network takes place through gel formation, yielding thicknesses of 50-500 nm. Thicker layers, suitable as membranes for example, are created by repeated wetting and drying. The sol-gel process can also be used to produce fibers. In all cases, gel formation is followed by a drying step. Figure 4 illustrates the different reaction and processing steps of the sol-gel process.

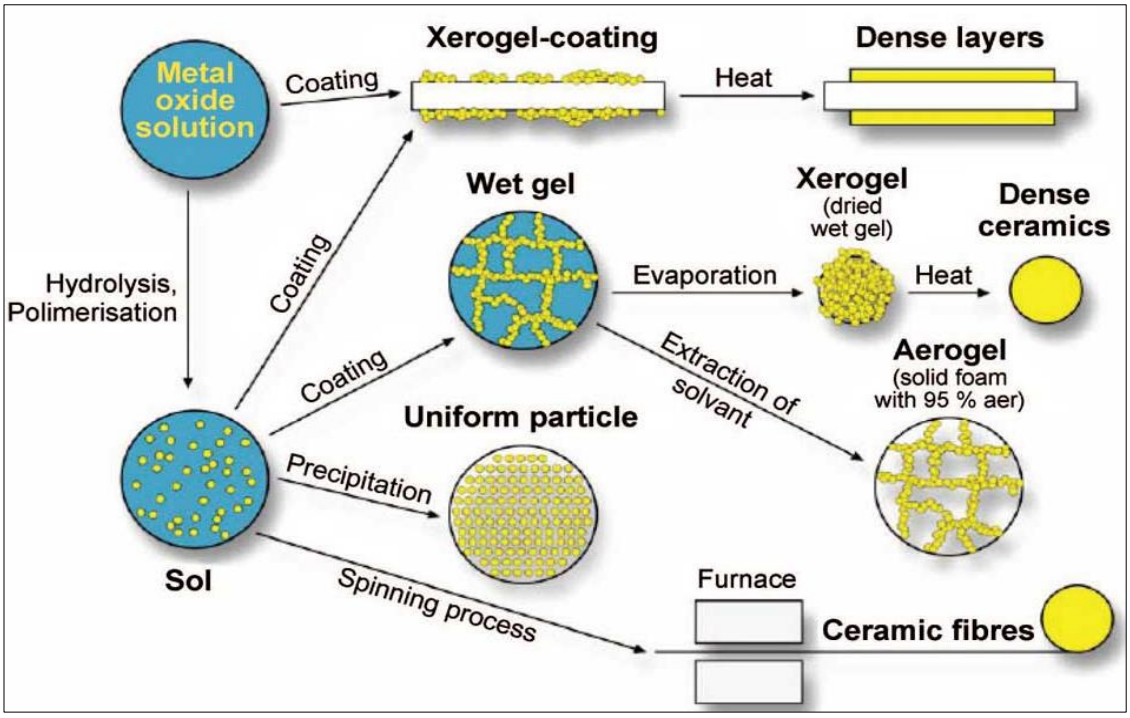

Figure II.1. *Reaction and processing steps in the sol-gel process. [67]*

A distinct advantage of the sol-gel process lies in the processability of the sols and gels, depending on processing step, into powders, fibers, ceramics and coatings. Moreover, highly porous nanomaterials can be produced. Composites can be created by filling in these pores during or after gel production. The low process temperature also enables substances to be

embedded into the gel during the synthesis step; these can then be stored or released in a controlled manner.

II.1.2 Anodized Titanium dioxide nanotubes TiO2 NTs

II.1.2.1 Material synthesis

The one dimensional (1D) tubular structure of TiO2 is of great scientific interest as well as practical significance particularly if the nanotubes are highly ordered, and aligned perfectly in close packed arrays. These outstanding characteristics are realized by the potentiostatic anodization of Ti substrates as it is a simple, straightforward and cheap preparation technique (see Fig. II.2). The majority of reported preparation methods only result in random networks of TiO2 nanotubes with uncontrolled dimensions. However, template-assisted atomic layer deposition (ALD) can produce nanotubes with controlled geometries. It requires long time and complicated preparation steps which is reflected in the high cost, and thus, a limit in use [68]. The first anodic oxidation study of pure Ti and Ti-6Al-4V substrates resulted in uniform porous films of TiO2 as reported by Zwilling *et al.* [69] in 1999. However a previous report before Zwilling's work had explored the anodization of Ti substrates in the presence of fluoride ions only results in a porous structure [70]. In 2001, Grimes and co-workers [71] reported that well-defined nanotube arrays were synthesized by the anodic oxidation of Ti substrates in HF containing electrolyte. These results aroused numerous attention and pushed the research towards the optimization of synthesis parameters (i.e. electrolyte configurations, applied voltage, reaction time, pH, agitation and temperature, etc.), to understand the formation mechanism and to employ these nanotubes in various research applications.

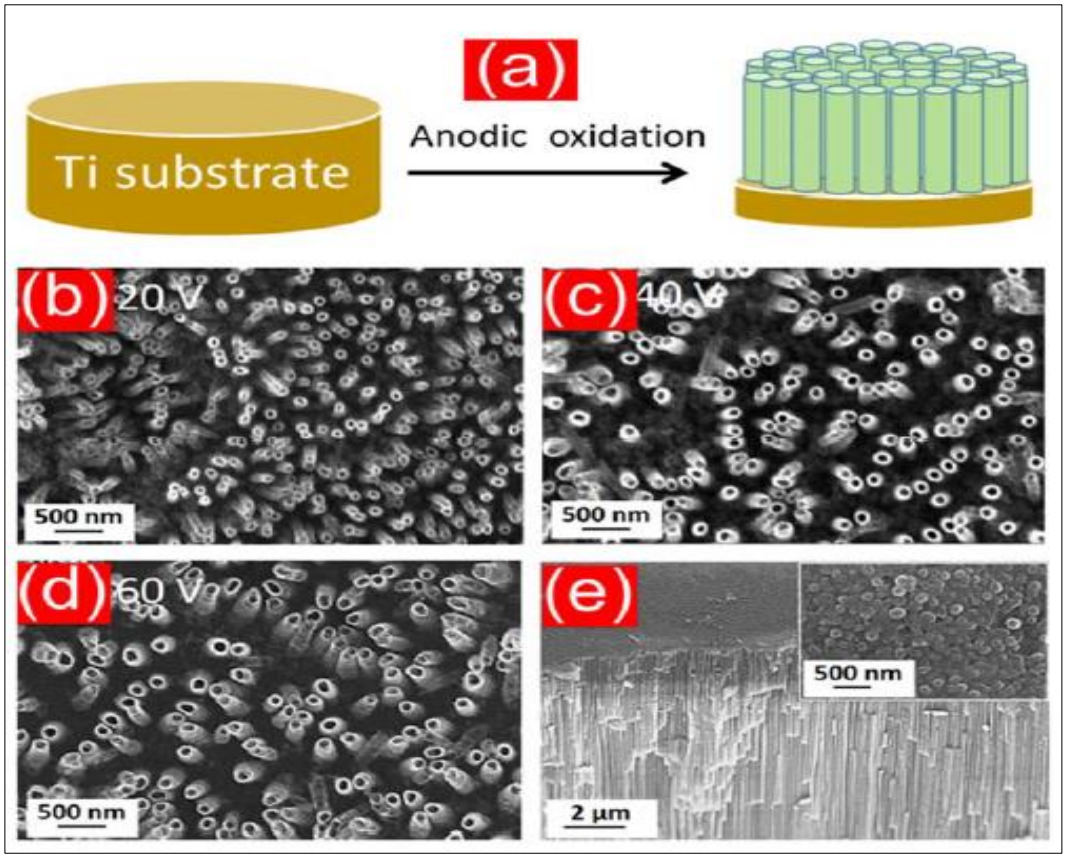

Fig.II.2. *Schematic illustration of the formation of anodized TiO2 nanotubes (a); SEM micrograph of anodized Ti substrates in formamide based electrolyte containing 0.2 M NH4F at different anodization voltage 20 V (b), 40 V (c) and 60 V (d); The cross-sectional view (e), the inset shows the bottom view of the nanotubes prepared at 60 V reprinted from ref.* [72].

Extensive studies proved that the TiO2 nanotubes obtained by anodic oxidation are self-organized, well-aligned perpendicular to the substrate, and exhibit uniform tube diameters, wall thicknesses as well as high surface areas. Furthermore, the nanotube dimensions (i.e. diameter, wall thickness and tube length) can be precisely controlled by tuning the applied voltage, the used temperature the electrolyte composition especially F- concentration [71-73]. The anodization is normally performed in a two-electrode electrochemical cell with the metal/alloy sheets as the working electrode and platinum foil or graphite as counter electrode in aqueous or organic electrolytes containing F– ions as shown in the schematic of Figure II.3.

Aqueous HF solutions were firstly used as electrolytes to manufacture TiO2 nanotube arrays with tube lengths below 500 nm [71, 74]. Replacing the aqueous solutions with organic electrolytes composed of ethylene glycol as solvent in addition to a fluorine source such as NH4F at high pH values allows for TiO2 nanotube formation with lengths reach up to 1000 micrometer [75, 76].

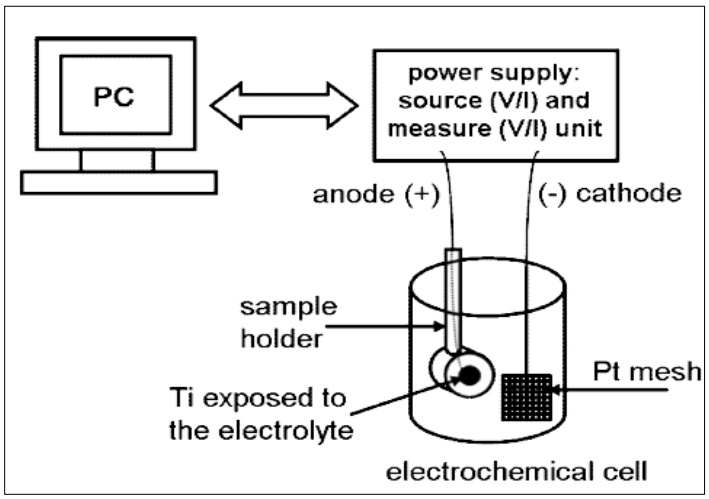

Fig. II.3. *Schematic illustration of anodic oxidation.* [77]

The nanotubes fabricated with these electrolytes always exhibited average diameters and wall thicknesses larger than 50 nm and 15 nm, respectively. Using neutral electrolytes such as those containing $(NH4)_2\ SO_4$ with NH_4F leads to a reduced dissolution rate of TiO2 resulting in nanotube arrays with length in the micrometer range [78]. These electrolytes are considered as mild oxidation conditions for Ti substrates. Note that, the chemical composition of the electrolyte also plays a central role in the physical properties of the fabricated nanotubes [79]. For instance, addition of acetic acid results in the formation of robust tubes. Furthermore, increasing the F- concentration allows control of the tube wall thickness [80].

II.1.2.2 Formation mechanism of TiO2 NTs

In anodization process, the achievement of vertically aligned TiO2 nanotubes directly from Ti foil under a sufficient applied potential in an electrochemical cell consists of working electrode (Ti foil) and counter electrode (Pt), which were immersed in the suitable electrolyte solution.
Once voltage is applied to titanium alloys connected to the anode of the electrochemical cell, the reactions occurring are the oxidation of Ti, which releases Ti^{4+} ions (Eq. II.4) and the reaction of Ti^{4+} ions with O^{2-} and OH^- (Eqs. II.5 and II.6 respectively).

$$Ti \rightarrow Ti^{4+} + 4e^- \quad \text{(II.4)}$$

$$Ti^{4+} + 2O^{2-} \rightarrow TiO_2 \quad \text{(II.5)}$$

$$Ti^{4+} + 4OH^- \rightarrow Ti(OH)_4 \quad \text{(II.6)}$$

After the formation of the initial oxide layer, the O^{2-} anions can migrate through the TiO2 layer reaching the Ti/oxide interface, where they react with the metal producing new amounts of

TiO2. The above reactions (Eq. II.4 to Eq. II.6) represent a field assisted oxidation process in which the applied potential controls the rate of ion migration within the TiO2 layer.

During anodization, the oxide film will continue to grow as long as the electric field is strong enough to drive the ionic conduction across the oxide [18].

When these electrochemical reactions are carried out in the presence of fluoride ions in an electrolyte solution, the anodization process is strongly affected by two possible ways and forms water soluble $(TiF6)^{2-}$ according to the equation given by:

$$Ti^{4+} + 6F^{-} \rightarrow [TiF_6]^{2-} \quad \text{(II.7)}$$

$$TiO_2 + 6F^{-} \rightarrow [TiF_6]^{2-} + 2H_2O \quad \text{(II.8)}$$

Under specific concentration of fluoride ions, the formation of TiO2 nanotubes is achieved as a result of equilibrium between the electrochemical oxidation of Ti to TiO2 and chemical dissolution of TiO2 [82]. Normally, the formation of TiO2 NTs in the anodization process depends on three simultaneous reactions: field-assisted oxidation of Ti metal to form TiO2, field-assisted etching of the oxide layer by the electric field weakening the bond between Ti and O, and the chemical dissolution of TiO2 by fluoride ions [231-233].

The growth of nanotubes is a result of competition between electrochemical oxide formations (Eqs. (II.4) to (II.6)) and chemical dissolution of the oxide by F^- ions producing $[TiF6]^{2-}$ complex ions (Eqs. (II.7) and (II.8)) by fluoride ions [234-236]. These three stages, which are undergone during the formation of TiO2 nanotubes, are illustrated in Figure II.4:

(**Stage I**) There is a sudden drop in current value at earliest stage of anodization process (as soon as potential is applied between electrodes) which is due to formation of passive TiO2 layer which offers resistance to the current flow.

(**Stage II**) In next stage, the current value is increasing due to field assisted and chemical assisted dissolution/etching of the passive oxide layer, so the resistance is decreased, pores and pits are appeared in the compact oxide layer due to the fluoride ions react with oxide layer, this region represent the nanopore formation.

(**Stage III**) In final stage, the steady state of TiO2 nanotubes is established and formation of regular shape of nanotubes occurs [83]. The curve is reaching a saturation at certain current value and there will not be much change in current value or there will be slow decrease, this region represents the tube lengthening.

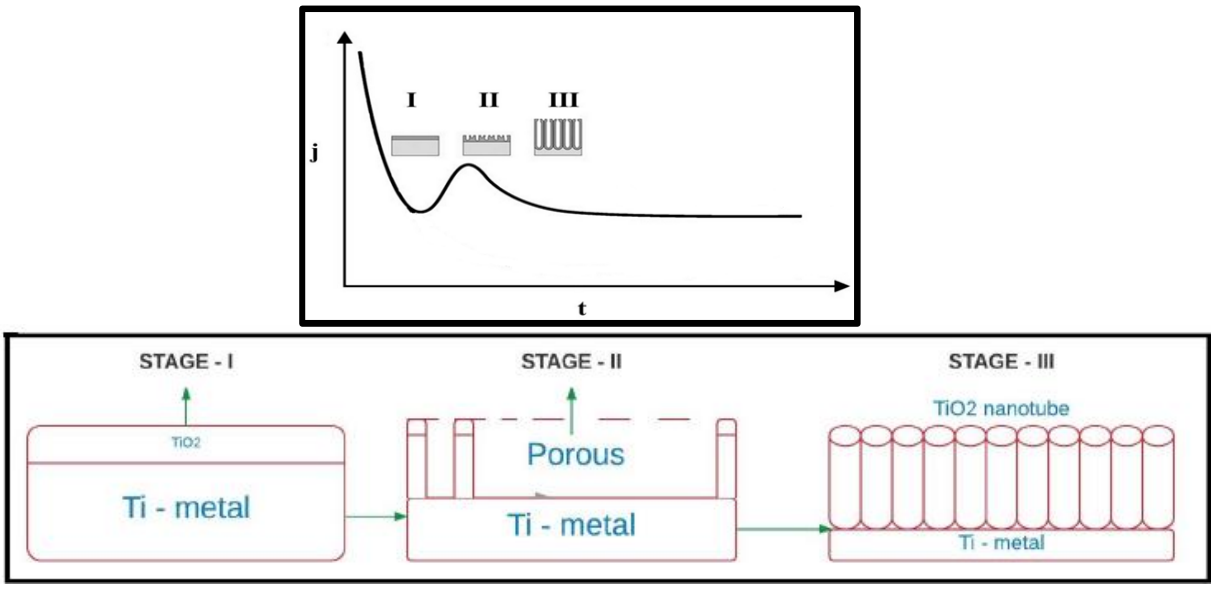

Fig II.4: *Growth process of TiO2 nanotubes by electrochemical anodization method. [82]*

The formation of nanotubes can be mainly depends upon the rate of formation of oxide and dissolution of oxide layer, which are greatly affected by factors such as anodization voltage, electrolytes concentration, temperature, water content etc. The thickness of the tubular layer remains unchanged when the rate of oxide growth and the rate of dissolution of oxide become equal. Later, the growth of nanotube length is independent on the anodization time, as define by the given voltage and electrolyte solutions.

Therefore, by increasing the applied voltage, the oxide formation and oxide dissolution rates increases, which helpful for growth of tubes length. Meanwhile, chemical dissolution is significant for the formation of vertically aligned TiO2 nanotubes, which mainly depend on both applied voltage and electrolytes concentrations [84].

II.2 Characterization techniques

II.2.1 X-ray diffraction study

X-ray diffraction (XRD) is a well-known technique for structural characterization of the material. Structure identification, determination of lattice parameters and grain size are based on the X-ray diffraction pattern. In X-ray powder diffractometry, X-rays are generated within a sealed tube that is under vacuum. A current is applied that heats a filament within the tube, the higher the current the greater the number of electrons emitted from the filament. This generation of electrons is analogous to the production of electrons in a television picture tube. A high voltage, typically 15-60 kV is applied within the tube. This high voltage accelerates the

electrons, which then hit a target, commonly made up of copper. When these electrons hit the target, X-rays are produced. The wavelength of these X-rays is characteristic of that target. These X-rays are collimated and directed onto the sample, which has been ground to a fine powder (typically to produce particle sizes of less than 10 microns). A detector detects the X-ray signals. Fig. 2.2 shows the schematic of X-ray diffractometer. The phenomenon of X-ray diffraction can be considered as reflection of X-rays from the crystallographic planes of the material and is governed by the Bragg's equation.

$$2d \sin\theta = n\lambda \qquad \text{(II.9)}$$

Where, "d" is lattice spacing, 'λ' is the wavelength of the monochromatic X-ray; 'n' is the order of diffraction and 'θ' is diffraction angle. The "d" values are calculated using above relation for known values of θ, λ and n. The X- ray diffraction data thus obtained is compared with American Standard for Testing of Materials (ASTM) or Joint Committee Powder Diffraction Standards (JCPDS) powder diffraction data to identify the unknown material. The sample used may be in the powder, single crystal or thin film form. The broadening of the XRD peaks reflects either crystallinity or the size of nanocrystal. The average crystallite size in a sample from XRD patterns is calculated using the Scherer's formula [85].

$$D = \frac{0.9\,\lambda}{\beta \cos\theta} \qquad \text{(II.10)}$$

Where, "D" is the average crystallite size, "λ" the wavelength of X-ray, 'θ' the Bragg angle and "β", line broadening at full width at half maximum (FWHM) of peak.

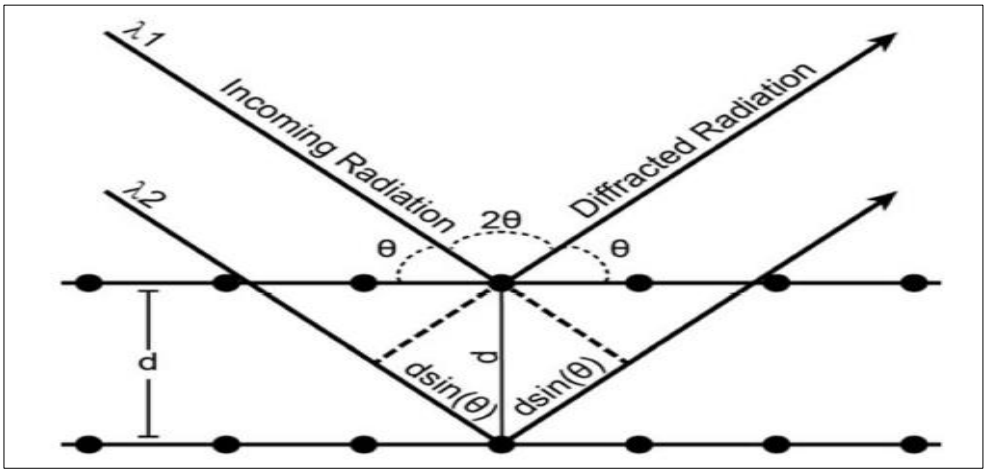

Figure II.5: *X-ray diffraction and schematic representation of Bragg's law.* [86]

II.2.2 XPS spectroscopy

X-ray photoelectron spectroscopy (XPS) is a quantitative technique which is used to measure the elemental composition of the surface (usually down to 10 nm), and find the empirical formula of the pure material, and the chemical and electronic states of the elements that exist within the surface of material. This technique requires ultra-high vacuum (UHV) conditions, pressures lower than about 10^{-9} Torr. The XPS spectra are obtained by irradiating the sample with an X-ray beam and recording the kinetic energy and number of electrons that escape from the surface, usually from work, the XPS data were collected by a SPECS system employing Al Kα radiation (10 kV; 100 W), and a pass energy of 20 eV. [87]

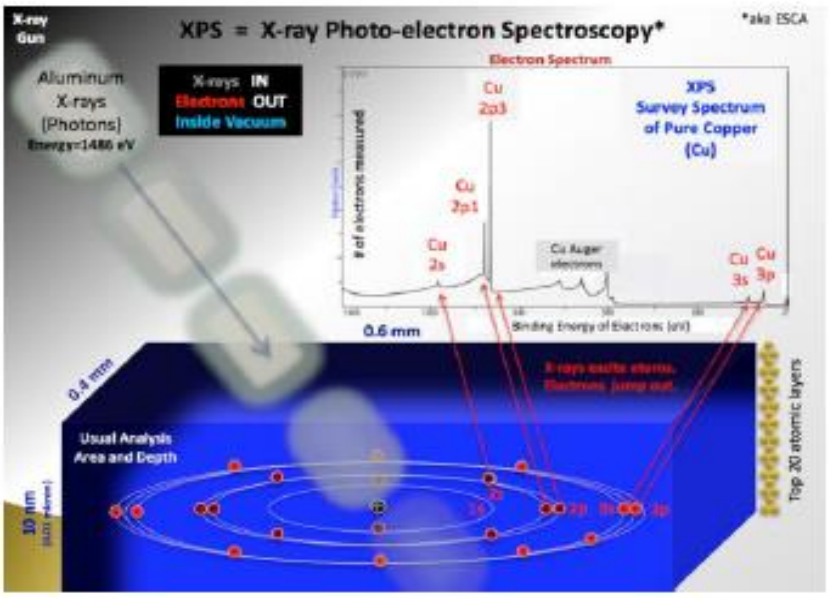

Fig. II.6: Basic components of a monochromatic XPS system.

II.2.3 Laser Raman spectroscopy

Raman spectroscopy is commonly used in chemistry to identify materials. It is a spectroscopic technique based on inelastic scattering of monochromatic light, usually from a laser source. The laser light interacts with molecular vibrations, phonons, or other excitations in the system, resulting in the energy of the laser photons being shifted up or down. As a result, it provides a fingerprint by which the molecule can be identified.

II.2.4 Scanning Electron Microscopy SEM

A scanning electron microscope (SEM) is a type of electron microscope that produces images of a sample by scanning it with a focused beam of electrons. The electrons interact with atoms in the sample, producing various signals that contain information about the sample's surface

topography and composition. The electron beam is generally scanned in a raster scan pattern, and the beam's position is combined with the detected signal to produce an image. Specimens can be observed in high vacuum, in low vacuum, in wet conditions (in environmental SEM), and at a wide range of cryogenic or elevated temperatures. The most common SEM mode is detection of secondary electrons emitted by atoms excited by the electron beam. The number of secondary electrons that can be detected depends, among other things, on the angle at which beam meets surface. By scanning the sample and collecting the secondary electrons that are emitted, using a special detector, an image displaying the topography of the surface is created.

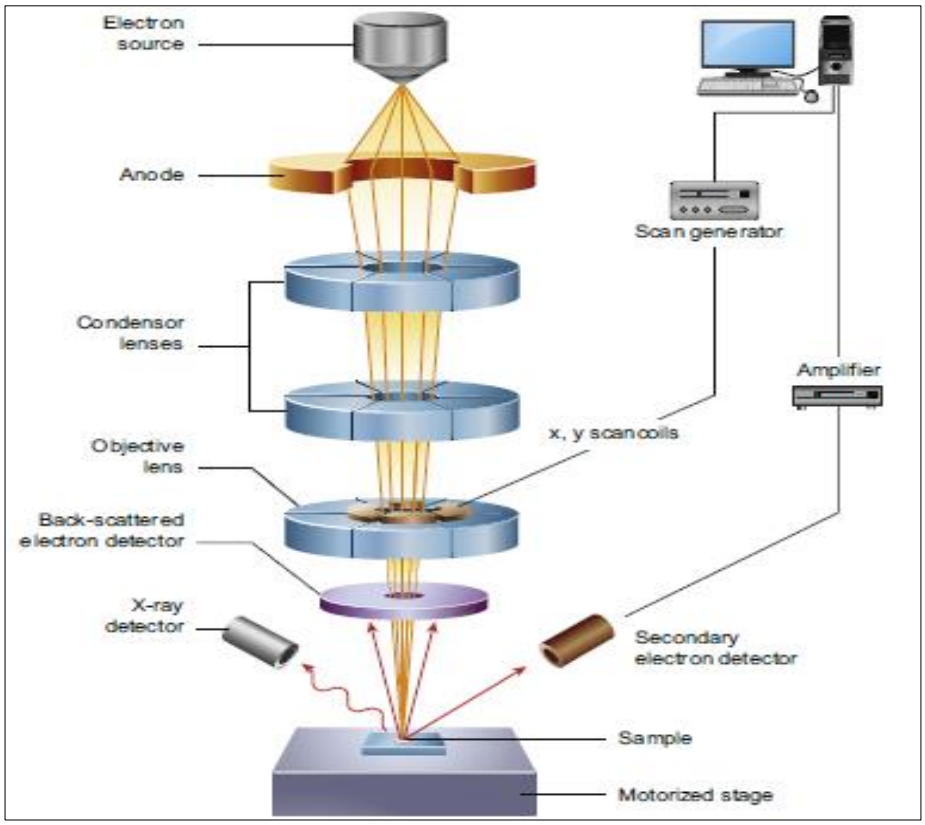

Figure II.7: *Schematic diagram of the core components of an SEM microscope* [88].

II.2.5 Energy Dispersive X-ray Spectroscopy

Energy Dispersive X-ray Analysis (EDX) technique is used to determine the elements present in the samples. To analyze the sample, it is bombarded by a focused electron beam. As shown in Fig. II.8, the applied electron beam excites the electrons in inner orbital of the atoms and removes it from the shell while leaving a hole in previous position of the electron.

The electrons of the outer shell prefer to transfer to inner orbital with lower energy and fill the vacancy. The energy difference between the outer and inner shell is released as X-rays. A detector reveals the number and the energy of X-rays emitted from the sample.

As each atom has a unique atomic structure one can detect the elements present in the material with an experimental error of about 3 %.

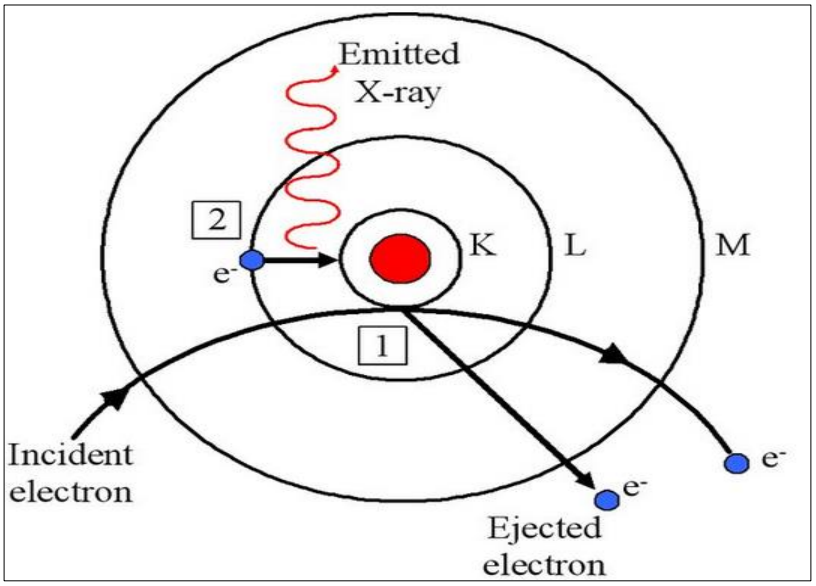

Figure II.8: *Principle of Energy Dispersive X-ray Analysis* [89]

II.2.6 Transmission electron microscopy

Transmission electron microscopy (TEM) is an indispensable technique for the structural characterization of nano-objects and nanostructures, in particular nanotubes, nanoparticles, nanocomposites … etc. It allows the observation on the atomic scale of these nanostructures and the characterization of their morphology.

In a Transmission electron microscope, the electrons are used as light sources. Lower wavelength of electrons enables TEM to get a resolution thousand times better than a light microscope, the electrons from a source such as an electron gun enter the sample and are scattered as they pass through it.

They are focused by an objective lens and are amplified by a magnifying (projector) lens, to produce the desired image. The wavelength of the electrons in the incident beam is given by:

$$\lambda = (0.0388/\sqrt{V})nm \qquad \text{(II.11)}$$

Where the energy acquired by the electron is $E = eV$ and V is the accelerating voltage expressed in kilovolts. If widely separated heavy atoms are present, they can dominate the scattering, with average scattering angle $\theta \sim \frac{\lambda}{d}$, where d is the average atomic diameter. Images are formed because different atoms interact with and absorb electrons to a different extent. A schematic representation of TEM is as shown in Figure.II.9.

A transmission electron microscope can form images by the use of the selected area electron diffraction (SAED) aperture located between the objective and projector lenses. The main part of the electron beam transmitted by the sample consists of electrons that have not undergone any scattering. The beam also contains electrons that have lost energy through inelastic scattering with no deviation of their paths, and electrons that have been reflected by various hkl planes.

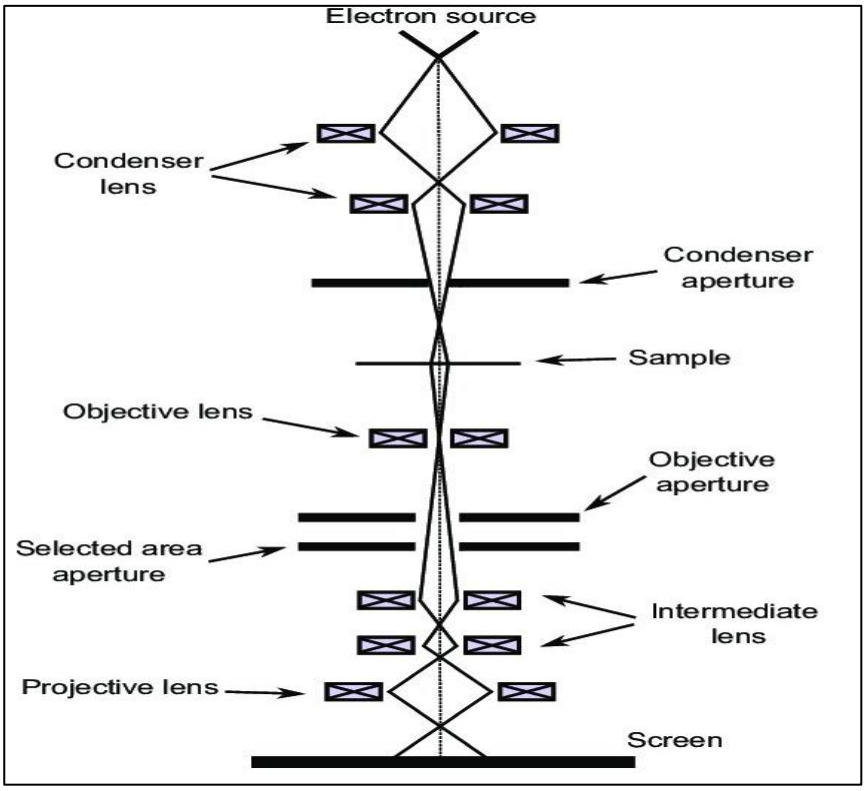

Figure II.9: *Schematic diagram of the core components of an TEM microscope*

II.2.7 UV-visible spectroscopy

Ultraviolet-visible (UV-vis) spectroscopy is used to obtain the absorbance spectra of a compound in solution or as a solid. What is actually being observed spectroscopically is the absorbance of light energy or electromagnetic radiation, which excites electrons from the ground state to the first singlet excited state of the compound or material. The UV-vis region of energy for the electromagnetic spectrum covers 1.5 - 6.2 eV which relates to a wavelength range of 800 - 200 nm.

The Beer-Lambert Law, Equation II.10, is the principle behind absorbance spectroscopy. For a single wavelength, A is absorbance (unitless, usually seen as arb. units or arbitrary units), ε is

the molar absorptivity of the compound or molecule in solution, *b* is the path length of the cuvette or sample holder (usually 1 cm), and *c* is the concentration of the solution.

$$A = \varepsilon bc \qquad \text{(II.12)}$$

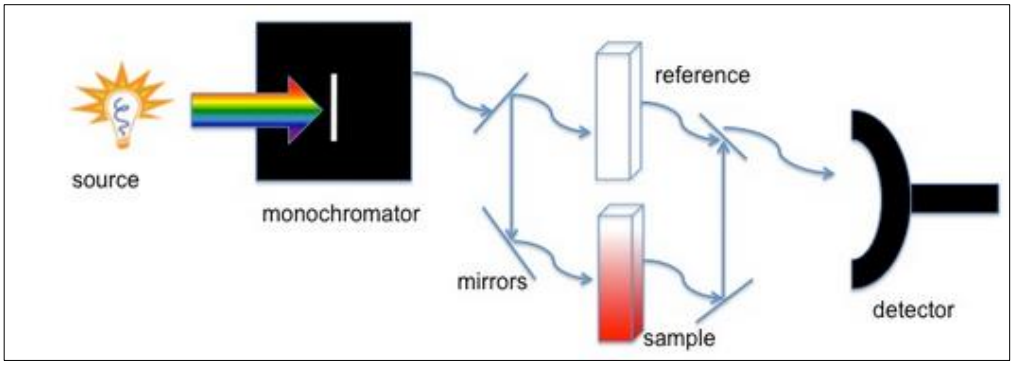

Figure II.10: Illustration of a double beam UV-vis instrument.

II.2.7.1 Optical absorption spectroscopy

Absorption spectrometry is a technique that allows us to observe not only the formation of nano-objects, nanoparticles in the solution, but also to probe the excited energy levels of the nanoparticles present in this solution, since they have levels of discrete energy, which results in the presence of absorption peaks on the optical spectrum.

The position of the absorption peaks corresponds to the energy of the excited levels. The shape and width at half maximum of these peaks tell us essentially about the particle size dispersion. The first absorption peak observed on the spectrum corresponds to the first excited level, which generally has an excitonic character.

The average width of the band gap or the gap of the nanoparticles is estimated from the position of its maximum. The position of the excitonic peak makes it possible to calculate the average value of the size of the nanoparticles.

After irradiation, the products formed are analyzed by an optical absorption spectrophotometer. The irradiated solution is placed in a quartz vessel whose optical path is known. According to the spectral domain to be analyzed, we used in our study a Perkin-Elmer Lambda 9 UV-Visible Spectrophotometer. The range of analysis ranges from 200 nm to near-infrared 3200 nm. This double-beam apparatus allows the analysis of the reference at the same time as the irradiated solution (Figure II.10).

II.2.7.2 Kubelka-Munk theory and Tauc plot

Kubelka-Munk theory provides an equation that relates the reflection of a sample under diffuse illumination to certain of its properties. In diffuse reflectance spectrum, scattered radiation is collected excluding secularly reflected light matching closely with the Kubelka-Munk function given by [90]:

$$F(R) = \frac{(1-R)^2}{2R} \qquad \text{(II.13)}$$

Where *R* is the reflectance. Kubelka-Munk parameter *F*(*R*) is related to the absorption spectrum, which can be used for obtaining the charge transition information in the range of reflectance wavelength.

In order to get the band gap value for different size samples, Tauc plot [90] has been used.

$$(h\nu\alpha)^{1/n} = A\left(h\nu - E_g\right) \qquad \text{(II.14)}$$

Where *h* is the Planck's constant, ν is frequency of vibration, α is absorption coefficient, *Eg* is band gap and *A* is proportional constant.

The value of the exponent *n* denotes the nature of the sample transition.

For direct allowed transition, *n*=1/2; for direct forbidden transition, *n*=3/2; for indirect allowed transition, *n*=2; for indirect forbidden transition, *n*=3.

Generally, the direct allowed transition has been reported for BiFeO3, *n*=1/2 is used in this work. The acquired diffuse reflectance spectrum is converted to Kubelka-Munk function. The α in the Tauc equation is substituted with *F*(*R*). Thus, in the actual experiment, the relational expression becomes:

$$[h\nu F(R)]^{\mathbf{2}} = A\left(h\nu - E_g\right) \qquad \text{(II.15)}$$

A line is drawn tangent to the point of inflection on the curve of equation, and the h value at the point of intersection of the tangent line and the horizontal axis is the band gap *Eg* value.

II.3 Electrochemical measurements techniques

II.3.1 Cyclic voltammetry

Cyclic voltammetry (CV) is one of the potentio-dynamic measurements in which a voltage is applied linearly between two values to an electrode at a fixed time against a reference electrode which has a constant potential. This technique is mainly used for providing specific information about the electrochemical reactions of electrodes such as redox reactions and charge-transfer kinetics as well as adsorption processes. The rate of voltage change with time during the measurement is known as scan rate (Vs-1). In typical voltammograms, the current of the working electrode is plotted *versus* the applied voltage. From voltammograms, the location of

redox potentials of electroactive materials as well as diffusion properties for the redox reactions can be easily determined. The typical shape of Cyclic Voltammetry is shown in figure II.11.

The most important step in characterizing any electro active material is to perform cyclic voltammetry under the selected potential window. In a three electrode system, a working electrode is immersed in the electrolyte, a potential is applied to it and the resulting current is recorded, yielding a cyclic voltammogram.

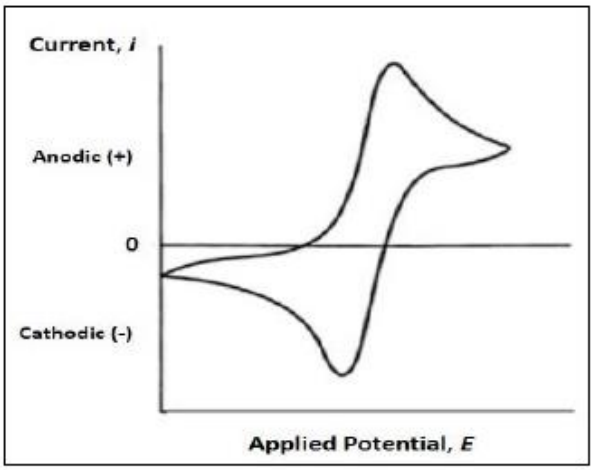

Fig II.11: *Typical shape of Cyclic Voltammetry*

A three-electrode system consisting of a working electrode, a reference electrode (usually, SCE or Ag/AgCl) and an auxiliary or counter electrode as shown in figure II.12.

In cyclic voltammetry, a reversible dc potential sweep (using a triangular potential waveform) was applied between working electrode and counter electrode and resulting current response versus a reference electrode (SCE) is measured.

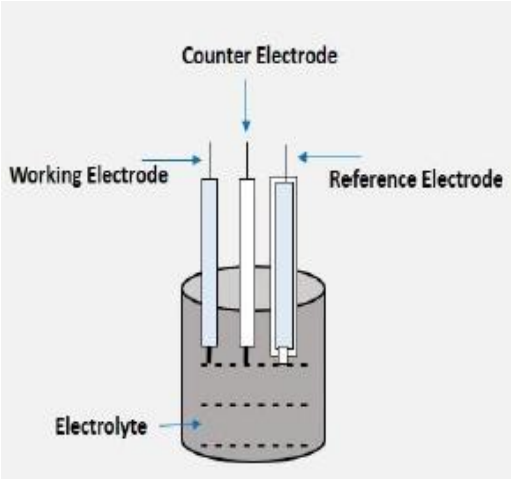

Fig II.12: *Three-electrode CV setup*

In cyclic voltammetry, on reaching t = t1 the sweep direction is inverted as shown in fig. II.13 and sweep until E_{min} then inverted and sweep to E_{max} etc. The important parameters involved are: [91]

- The initial Potential Ei
- The initial sweep direction
- The sweep rate
- The maximum potential, Emax
- The minimum potential, Emin
- The final Potential, Ef

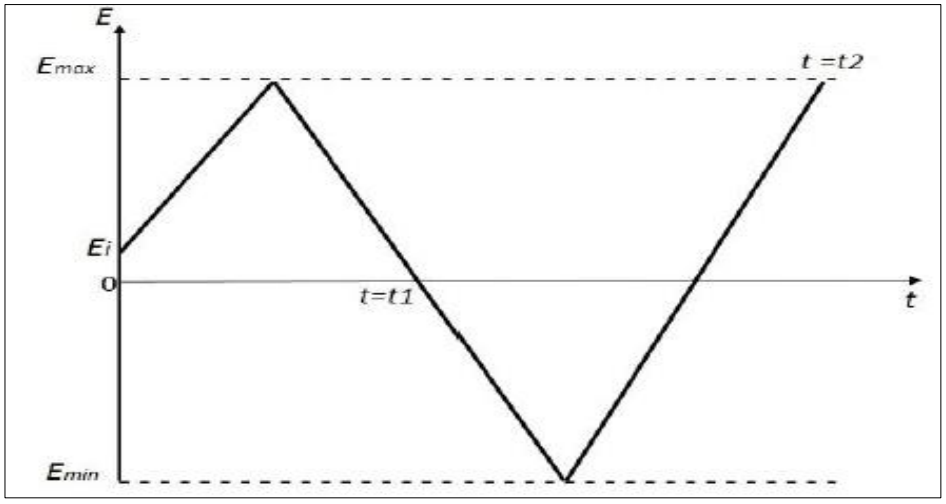

Figure II.13: Variation of applied potential for Cyclic Voltammetry

II.3.2 Galvanostatic charge discharge *(Chronopotentiometry)*

Galvanostatic cycling (CD) is widely used to calculate the capacitance and cycling stability of electrodes or devices. The principle of CD is to measure the resulting voltage simultaneously when applying a constant current to an electrode or a device between two preset voltage limits [19].

Galvanostatic charge and discharge is a more accurate technique to evaluate the specific capacitance of active materials than CV method. Positive and negative constant currents come across the working electrode to charge and discharge the electrode in a set voltage range with recording the time. A typical GCD curve is shown in Fig II.14, in which the voltage is drawn as a function of the time. Then, the specific capacitance can be determined by the potential window, current density and discharge time with the following equation:

where *I* is the current, Δt is the discharge time, *m* is the mass of electrode material, and *U* is the potential window.

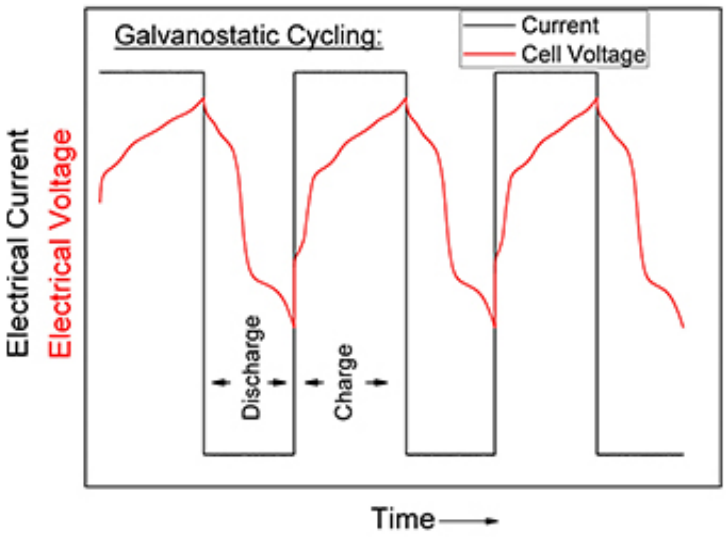

Figure II.14: *Charge-discharge curve* [92].

II.3.3 Electrochemical Impedance Spectroscopy

The equivalent series resistance, charge transfer resistance and diffusion impedance of electrochemical devices can be studied by electrochemical impedance spectroscopy (EIS). The main difference between EIS and CV that in EIS a sinusoidal voltage signal is imposed at a range of frequencies and the resulting current is measured, while a linear voltage is applied in CV.

In electrochemical impedance spectroscopy (EIS), the system under test is excited by a small amplitude ac sinusoidal signal of potential or current in a wide range of frequencies and the response of the current or voltage is measured. For typical impedance measurements, a small excitation signal is used. The system excitation caused by the time-dependent potential fluctuation has the form:

$$E(t) = E_0\cos(\omega t) \qquad \text{(II.16)}$$

Where $E(t)$ is the applied potential at time t, E_0 is the potential amplitude, and ω is the angular frequency that is defined as the number of vibrations per unit time (frequency, Hz) multiplied by 2π and expressed in rad/s. In a linear system, the output current signal $I(t)$ has amplitude I_0 and is shifted in phase by ϕ.

$$I(t) = I_0\cos(\omega t - \phi) \qquad \text{(II.17)}$$

Then, the impedance of the system $Z(t)$ is calculated from Ohm's law

$$I(t) = E(t)/I(t) = Z_0\cos(\omega t)/\cos(\omega t - \phi) \qquad \text{(II.18)}$$

By using Euler's relationship defined as: $\exp(j\phi) = \cos(\phi) + jsin(\phi)$, the system impedance is expressed as a complex function. The excitation potential input and the resulting current output are described as:

$$E(t) = E_0 \exp(j\omega t) \quad \text{(II.19)}$$

$$\mathrm{I(t)} = \mathrm{I_0 exp[j(\omega t - \phi)]} \quad \text{(II.20)}$$

Based on Ohm's law, we get the expression for the impedance as a complex number,

$$Z(\omega) = \mathrm{Z_0}\exp(\mathrm{j}\phi) = \mathrm{Z_0}(\cos\phi + \mathrm{j}\sin\phi) \quad \text{(II.21)}$$

When the real part of the impedance is plotted on the axis of the abscissa and the imaginary part is plotted on the axis of the ordinate, we get a "Nyquist plot." The example presented in fig. II.15 (a) is a graphical expression of the complex plane of the electrical equivalent circuit of fig II.15 (b). In the Nyquist plot, a vector of length |Z| is the impedance and the angle between this vector and the real axis is a phase shift, ϕ.

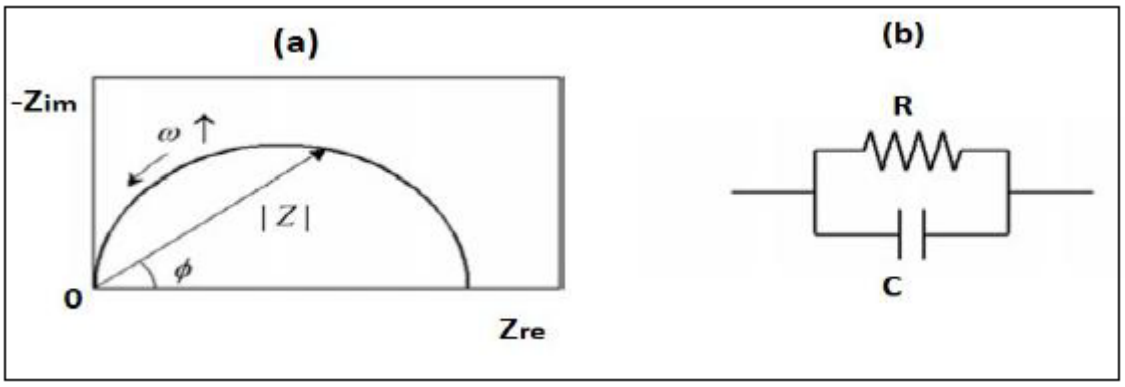

Fig. II.15. *Graphical representation of EIS and (b) its equivalent circuit*

The equivalent circuit of insertion materials includes the diffusion impedance, originating from the solid-state diffusion of the active species. Assuming a semi-infinite diffusion process, the Warburg element with an impedance of Z_w is connected in series with the resistor representing the interfacial charge transfer R_{ct} as shown in fig. II.15 (a) The Nyquist plot for the equivalent circuit features an inclined line with a slope of 45° in the low-frequency region, due to the Warburg impedance fig. II.16 (b).

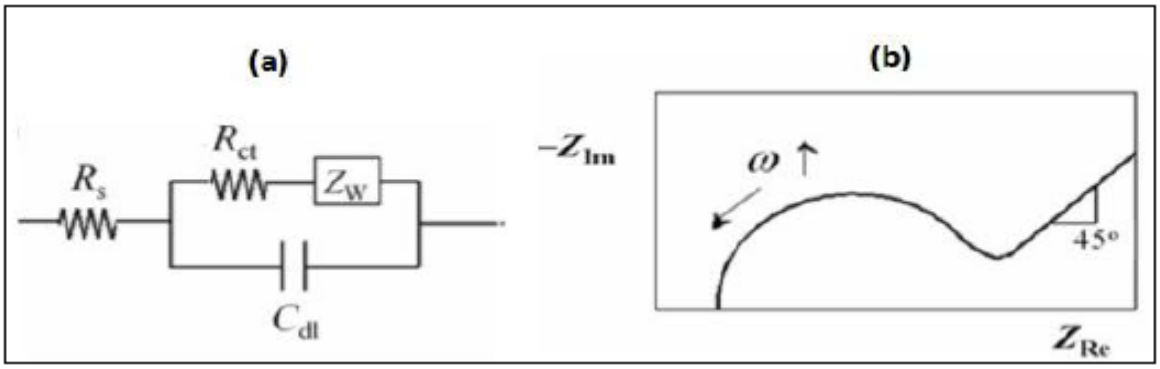

Fig. II.16. *Nyquist plot (a) Graphical representation of EIS and (b) its equivalent circuit with different parameters.*

Chapter III

Computational methodology

III.1 Introduction

The physics of condensed matter and the materials science are fundamentally concerned by the understanding and exploiting the properties of interacting electron and atomic nuclei systems.

This is well known since the development of quantum mechanics. With this, comes the recognition that at least, almost all properties of materials can be studied by suitable computation tools for solving this particular problem of quantum mechanics.

Unfortunately, the electrons and nuclei that compose the materials constitute a highly interacting multi-body system and this makes solving the Schrödinger equation extremely difficult, and as Dirac (1929) stated, progress depends on the development of approximate techniques sufficiently precise. Thus the development of density functional theory (DFT). To describe a material, one must know its properties (electronic, structural, optical ...), and this implies the knowledge of the interactions between the electrons and ions that constitute it.

III.2 Many body problems

III.2.1 Schrödinger Equation

The electronic structure of N-body system is described in nonrelativistic quantum mechanics using the equation of Schrödinger:

$$\widehat{H}\psi_i(\{r_i\},\{R_j\}) = \mathrm{E}\psi_i(\{r_i\},\{R_j\}) \quad \text{(III.1)}$$

Where $\psi(\{r_i\},\{R_j\})$ is the wave function for a molecular system consisting of M nuclei and N electrons and contains all the information of the system, $\{r_i\}$ stands for the term of the variables which describe the electrons and $\{R_j\}$ describes the nuclei.

E is the total energy and $\widehat{H}$ is the corresponding total Hamiltonian operator of the system and describing the set of interactions occurring, and hence it can be written in its exact form as follows:

$$H_{tot} = T_e + T_N + V_{ee} + V_{eN} + V_{NN} \quad \text{(III.2)}$$

$$\widehat{H}_{tot} = -\frac{\hbar^2}{2}\sum_i \frac{\nabla^2\vec{r}_i}{m_e} - \frac{\hbar^2}{2}\sum_i \frac{\nabla^2\vec{R}_i}{M_n} + \frac{1}{8\pi\varepsilon_0}\sum_{i\neq j}\frac{e^2}{|\vec{r}_i-\vec{r}_j|} - \frac{1}{8\pi\varepsilon_0}\sum_{i\neq j}\frac{e^2 Z_i}{|\vec{R}_i-\vec{r}_j|} + \frac{1}{8\pi\varepsilon_0}\sum_{i\neq j}\frac{e^2 Z_i Z_j}{|\vec{R}_i-\vec{R}_j|} \quad \text{(III.3)}$$

- T_e: is the kinetic energy of the N electrons of mass m_e.
- T_N: is the kinetic energy of the M nuclei of mass M_n.
- V_{ee}: is the repulsive coulombic electron-electron interaction.
- V_{eN}: is the attractive coulombic interaction nucleus-electron.
- V_{NN}: is the repulsive coulombic nucleus-nucleus interaction.
- r_i, r_j: are defining the positions of the electrons.
- R_i, R_j: are defining the positions of the Z nuclei.
- m_e, M_n: are respectively the mass of the electron and the nucleus.

The treatment of the N-body problem in quantum mechanics consists in solving the exact Schrödinger equation where the global wave function depends on 3N coordinates of all the particles and time, which is extremely difficult or impossible because the Modern quantum mechanics has no method to solve problems when particles are in large numbers in the system. Therefore, this equation will be simplified by various approximations, so that it can be solved.

III.2.2 Born Oppenheimer:

In order to reduce the complexity of solving the Schrödinger equation, the Born-Oppenheimer approximation [93] was introduced based on the fact that nuclei are much heavier than

electrons, and therefore much slower, than the electrons. As a result, nuclei can be considered as effectively frozen at fixed positions, while only electrons being considered as mobile. Consequently, the kinetic energy term of the nuclei is zero. The nuclei-nuclei potential term also reduces to a constant. Therefore, the above Hamiltonian equation become simplified as:

$$H_{tot} = \hat{T}_e + \hat{V}_{ee} + \hat{V}_{ext} \quad \text{(III.4)}$$

Where the electron-nuclear interaction represented by Vext. We can further explain the remaining terms as:

$$\hat{T}_e = -\sum_i \frac{\hbar^2}{2m_e} \nabla^2 r_i \quad \text{(III.5)}$$

$$\hat{V}_{ext} = -\sum_i \sum_j \frac{Z_i e^2}{4\pi\varepsilon_0 |R_i - r_j|} \quad \text{(III.6)}$$

$$\hat{V}_{ee} = \frac{1}{2}\sum_i \sum_{j\neq i} \frac{e^2}{4\pi\varepsilon_0 |r_i - r_j|} = \sum_i \sum_{j>i} \frac{e^2}{4\pi\varepsilon_0 |r_i - r_j|} \quad \text{(III.7)}$$

The Hamiltonian obtained after applying the Born-Oppenheimer approximation is simpler, but still far too difficult to solve, due to the correlation of the electron distribution interactions. Thus, Additional approximations are used including Hartree's.

III.2.3 Hartree-fock Approximation

The method of Hartree [94] reduces the N-body system into a one-particle system by considering the electrons as independent, and each of them moving in the mean field created by the other and matching an orbital to each electron. The wave function of the electronic system is considered as the direct product of the one-particle wave functions:

$$\psi(\vec{r}_1, \vec{r}_2, \dots, \vec{r}_N) = \psi_1(\vec{r}_1).\psi_2(\vec{r}_2) \dots \psi_N(\vec{r}_N) \quad \text{(III.8)}$$

In 1930, Fock [95] showed that the solutions of the Hamiltonian (III.4) violate the Pauli exclusion principle, because they are not antisymmetric with respect to the exchange of any two electrons.

$$\psi(\vec{r}_1, \vec{r}_2, \dots, \vec{r}_i, \dots, \vec{r}_j, \dots, \vec{r}_N) = -\psi(\vec{r}_1, \vec{r}_2, \dots, \vec{r}_j, \dots, \vec{r}_i, \dots, \vec{r}_N) \quad \text{(III.9)}$$

The anti-symmetrization of the electronic wave function is written by permuting two electrons for example:

Such a description thus obeys the Pauli's exclusion principle that "two electrons cannot exist simultaneously in the same quantum state, as well as the indiscernibility of the electrons". However, the Hartree's approximation doesn't contain this feature, because the electron i occupies precisely the state i. As an improvement, an antisymmetric wave function is

constructed via a Slater determinant of the individual orbitals generalized by Hartree and Fock by showing that the Pauli Principle is respected:

$$\psi(r_1, \dots, r_N) = \frac{1}{\sqrt{N!}} \begin{vmatrix} \varphi_1(r_1) & \varphi_1(r_2) & \dots & \varphi_1(r_N) \\ \varphi_2(r_1) & \varphi_2(r_2) & \dots & \varphi_2(r_N) \\ \vdots & \vdots & \ddots & \vdots \\ \varphi_N(r_1) & \varphi_N(r_2) & \dots & \varphi_N(r_N) \end{vmatrix} \qquad \text{(III.10)}$$

This equation is self-consistent and received the name of self-consistent field (SCF).

Because in deriving the Hartree equation, it depends on itself on the orbitals that are the solution of all other Hartree equations.

These Hartree-Fock equations are difficult to solve when the system studied has a large number of electrons. Electron-electron interactions produce additional energy terms in addition to the Hartree-Fock approximation, which are called correlation energy terms according to Wigner [96]. A whole category of methods, called configuration interaction, was built on this basis. Their goal is to come up with an exact solution to Schrödinger's equation.

However, the scope of calculations for very small systems is limited by the number of configurations which grows rapidly with the number of electrons involved.

To remedy this, the density functional theory was developed for the resolution of the Schrödinger equation from the electronic density which is taken as the fundamental variable describing the state of a system, and not wave functions. Thus giving a considerable conceptual simplification of this problem since it reduces the number of degrees of freedom by 3N, to the degrees of freedom of a scalar function in three-dimensional space, reducing thus an N body system to a particle system.

III.3 Density Functional Theory

The DFT consists in describing the system according to its electronic density and not the wave functions [97-99]; it was derived from the physics of the solid, where it was intended to determine the ground state properties of a system composed of a fixed number of electrons in coulombic interaction with point nuclei, with the sole knowledge of electron density. This theory was seen in 1927 by the works of Llewellyn Thomas and Enrico Fermi [100]. During which, Thomas and Fermi considered the system as a homogeneous gas and its kinetic energy as density functional where they have dismissed the interactions and neglected the exchange-correlation effects that appears between the electrons. In 1930 Dirac [101] corrected this defect by introducing the local exchange approximation to give the Thomas-Fermi-Dirac model, but it was not approvable because of its poor results.

Another model was proposed by Slater in 1951 [102] called Hartree-Fock-Slater, to reform the Thomas-Fermi-Dirac model, which was based on the study of an improved uniform gas with a local potential where it has been particularly used in solid physics. However, it was in 1964 that the DFT really began with the two fundamental theorems, demonstrated by Hohenberg and Kohn [103]. It was initially designed and applied to solid-state problems, and then expanded to chemical applications [98]. Later, thanks to Kohn-Sham's approach [104] the theorems of Honberg and Kohn find an application framework.

III.3.1 Hohenberg-Kohn Theorems

- ***First theorem:*** The total ground state energy of a interacting N electron system in the presence of an external potential is a unique functional of the electron density.

This theorem highlights a unique correspondence between the external potential and the electronic density. Since this sets the number of electrons, it also uniquely determines the wave function and thereby the electronic properties of the system. Thus, for a given system, the energy is written as follows:

$$E[\rho(r)] = T[\rho(r)] + V_{ee}[\rho(r)] + V_{ext}[\rho(r)] \quad \text{(III.11)}$$

$$E[\rho(r)] = F_{HK}[\rho(r)] + \int \rho(\vec{r})\, V_{ext}(r) dr \quad \text{(III.12)}$$

$$F_{HK} = T_e[\rho(r)] + V_{ee}[\rho(r)] \quad \text{(III.13)}$$

$\boldsymbol{F_{HK}}$ is the Hohenberg-Kohn functional containing the kinetic energy and potential energy due to the electron-electron repulsive interaction.

- ***Second theorem :*** The functional energy is minimal when the electron density coincides with the true density of the ground state.

This second theorem stems from the fact that the total energy functional of any multi-particle system has a minimum which corresponds to the ground state. The particle density of the ground state satisfies:

$$E(\rho_0) = Min\, E(\rho) \quad \text{(III.14)}$$

Hohenberg and Kohn have shown that the true density of the ground state is that which minimizes the energy E(ρ), and all the other properties are also a functional of this density. The ground state energy of an electronic system in an external potential is determined by the variational method.

III.3.2 Kohn-Sham Equations

In 1965 W. Kohn and L. Sham [104] introduced the notion of a fictitious auxiliary system of N electrons without interaction, moving in an effective potential instead of a system of N electrons interacting in an external potential, this is what makes us write the problem in the form of three interdependent equations, the Kohn-Sham equations:

The first gives the definition of the effective potential in which the electrons immerse:

$$V_{eff}[\rho(r)] = V_{ext} + V_H[\rho(r)] + V_{xc}[\rho(r)] \qquad \text{(III.15)}$$

Where:

$V_H[\rho(r)] = \frac{1}{2}\int \frac{\rho(r\prime)}{|r-r\prime|} dr'$: Hartree potential for electrons

$V_{xc}[\rho(r)] = \frac{\partial E_{xc}[\rho(r)]}{\partial \rho(r)}$: Exchange correlation potential

The second uses the effective potential in the N mono-electronic Schrödinger equations in order to obtain the single-particle (φ_i) wave functions:

$$\left[-\frac{1}{2}\nabla^2 + V_{eff}(r)\right]\varphi_i(r) = \varepsilon_i \varphi_i(r) \qquad \text{(III.16)}$$

With, ε_i and $\varphi_i(r)$ are respectively, the energy of a Kohn-Sham orbital and the particle-specific wave function.

The third shows how to access the density from the N mono electronic functions:

$$\rho(r) = \sum_{i=1}^{N} |\varphi_i(r)|^2 \qquad \text{(III.17)}$$

This formalism of Kohn and Sham is a practical and powerful tool for the resolution of an equation involving mono-electronic wave functions, because, equation (III.16) can be seen as a Schrödinger equation at a particle where the external potential has been replaced by the well-defined effective potential in equation (III.15) and can be used to determine the electron density.

III.3.3 Solving KS equations

Determining the fundamental state of the system is then equivalent to solving the Kohn-Sham equations, in a self-consistent manner, "**or Self-Consistent Field SCF**", the set of these eigenvalue equations. Where a starting density is injected into the self-coherent cycle to calculate the functionals of the initial density, we calculate V_{eff} with equation (III.15) as a second step, which allows us to solve the differential equation (III.16) for φ_i.

In the last procedure, the φ_i solutions are reinjected into the equation (III.17) to compute a new density that allows us to calculate a new potential V_{eff}... and so on. The iterative procedure continues until convergence is reached. The procedures are grouped in the diagram below.

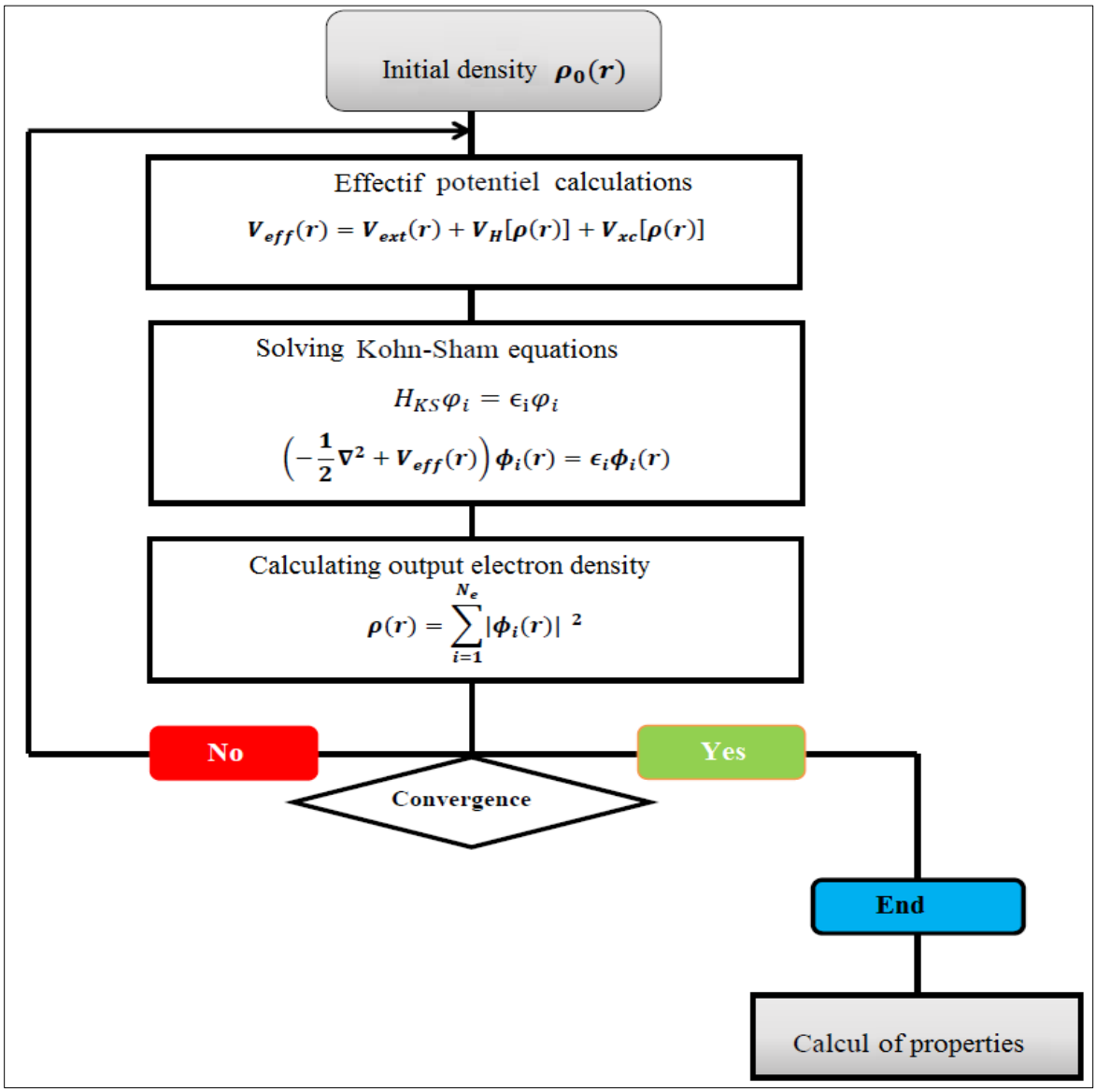

Figure III.1. *Self-consistent iteration process used to solve Kohn Sham's equations.*

III.4 The exchange-correlation functionals

The method of Kohn and Sham remains accurate in its formulation, and all its terms can be evaluated except that of exchange correlation which is not known exactly.

It is therefore necessary to approximate this exchange-correlation potential to be able to apply the DFT, because the more precise the knowledge of this potential, the more precisely the density will be obtained. Here we present standard approximations, which have been widely

used such as the local density approximation (LDA) and the generalized gradient approximation (GGA).

III.4.1 LDA approximations

The Local Density Approximation (LDA) was proposed in 1965 by Kohn and Sham [104] which treats an inhomogeneous system as being locally homogeneous, with an exactly known exchange and correlation energy:

$$E_{xc}^{LDA}[\rho(\vec{r})] = \int \varepsilon_{xc}(\vec{r})[\rho(\vec{r})]d^3\,\vec{r} \quad \text{(III.18)}$$

$$\varepsilon_{xc}(\vec{r}) = \varepsilon_{xc}^{hom}[\rho(\vec{r})] \quad \text{(III.19)}$$

Where:

ε_{xc}^{hom} is the homogeneous density of an electron gas that may be constant, but in most cases it is determined by parametrization procedures such as that of Wigner (1938) [96], Hedin et al (1971) [105], Vosko-Wilk-Nussair (1980) [106] or even Perdew-Zunger (1981) [107].

The density $\varepsilon_{xc}[\rho(\vec{r})]$ can be considered as the sum of a contribution of exchange and correlation:

$$\varepsilon_{xc}[\rho(\vec{r})] = \varepsilon_x[\rho(\vec{r})] + \varepsilon_c[\rho(\vec{r})] \quad \text{(III.20)}$$

$\varepsilon_x[\rho(\vec{r})]$ is the exchange energy for a homogeneous gas of electrons (Dirac exchange term [102]):

$$\varepsilon_x[\rho(\vec{r})] = -\frac{3}{4}\left[\frac{3\rho(\vec{r})}{\pi}\right]^{1/3} \quad \text{(III.21)}$$

The correlation energy $\varepsilon_c[\rho(\vec{r})]$ can not be expressed exactly. The approximation of this energy is established, based on an interpolation of very precise quantum Monte Carlo results on the uniform electron gas produced by Ceperley and Alder [108].

III.4.2 LSDA approximation:

In the case of magnetic materials, the electron spin provides an additional degree of freedom and the LDA must then be extended to the Local Spin Density Approximation (LSDA) approximation where the energy of exchange and correlation becomes a functional of both up and down spin densities:

$$E_{xc}^{LSDA}[\rho_\uparrow, \rho_\downarrow] = \int \varepsilon_{xc}(\vec{r})[\rho_\uparrow(\vec{r}), \rho_\downarrow(\vec{r})]\, d^3\vec{r} \quad \text{(III.22)}$$

III.4.3 GGA approximations

The generalized gradient approximation (GGA) [109] is an improvement of LDA and LSDA in the point where the electron gas is in its real form, i.e, non-uniform and non-local, which holds account the inhomogeneity of the electronic density. Therefore, the exchange-correlation energy depends on the electronic density $\rho(r)$ and the gradient $\nabla\rho(r)$ as follows:

$$E_{xc}^{LSDA}[\rho(\vec{r})] = \int \rho(r)\, \varepsilon_{xc}^{GGA}[\rho(\vec{r})|\nabla\rho(r)|]d^3r \qquad \text{(III.23)}$$

Where ε_{xc}^{GGA} represents electron exchange-correlation energy, in a non-homogenously interacting electron system.

In the case where a polarization of the spins is taken into account, the exchange and correlation energy is described as follows:

$$E_{xc}^{GGA}[\rho_\uparrow(r), \rho_\downarrow(r)] = \int \rho(r)\, \varepsilon_{xc}^{GGA}[\rho_\uparrow, \rho_\downarrow, \nabla\rho_\uparrow(r), \nabla\rho_\downarrow(r)]d^3r \qquad \text{(III.24)}$$

Despite the many successes of LSDA and GGA, it can not be said that these methods are perfect for approximating the exchange-correlation potential.

III.4.4 DFT + U approximation

For highly correlated systems that contain a transition metal or rare earths with d or f orbitals, partially filled, it is difficult to correctly describe and predict the properties of their excited states by the L(S)DA and GGA approaches [110]. So to improve the results, an attempt was proposed by Dudarev et al [111] in the context of the correction of the DFT called DFT + U (LSDA + U, GGA + U), where U is the effective Coulomb repulsion intra-site between localized electrons (Hubbard term).

The fundamental principle of this approximation is to add the additional term U to the potential LSDA or GGA for each orbitals d and f, in order to obtain the good gap and the good magnetic properties for the magnetic materials. The DFT + U is based on a Hamiltonian, which is called Hubbard's Hamiltonian ($\widehat{H}$) and is written in the following form:

$$\widehat{H}_{Hubbard} = \frac{U}{2}\sum_{m,m',\sigma} \hat{n}_{m,\sigma}\hat{n}_{m',-\sigma} + \frac{(U-J)}{2}\sum_{m\neq m',\sigma} \hat{n}_{m,\sigma}\hat{n}_{m',\sigma} \qquad \text{(III.25)}$$

$\hat{n}_{m,\sigma}$ is the operator that gives the number of electrons occupying an orbital of magnetic quantum number m and of spin σ at a particular site. J is the parameter that corresponds to the exchange energy. U is the spherically averaged Hubbard parameter where;

$U = E(d^{n+1}) + E(d^{n-1}) - 2E(d^n)$, this parameter describes the energy cost for placing an extra electron on a particular site and it depends on the spatial extension of the wave functions and screening.

Therefore, the DFT+U contains the energy contributions previously accounted for by the functional DFT. According to the form:

$$E^{DFT+U} = E^{DFT} + E_{HUb} - E_{dc} \qquad \text{(III.26)}$$

Where, E^{DFT} is the contribution of energy by the standard DFT (LSDA or GGA), E_{HUB} is the correction of electron-electron interaction energy and E_{dc} is the double counting term that corrects contributions to the total energy included in both E^{DFT} and E_{HUB}.

The expression proposed by Dudarev et al [111] for the evaluation of energy E^{DFT+U} is as follows:

$$E_{DFT+U} = E_{DFT} + \frac{(U-J)}{2}\sum_{m\sigma}\left(\hat{n}_{m,\sigma} - \hat{n}^2{}_{m',\sigma}\right) \quad \text{(III.27)}$$

m, σ: The number of Kohn-Sham orbital occupancies such as, the total number of electrons for a given angular momentum and spin.

Finally, the value of U can be determined by three different methods, which are:

- Either from the additional calculations called "constraint LSDA calculations" [112]
- Either from the experimental results.
- By the regular variation from 2 eV to 8 eV.

III.4.5 Modified Becke Johnson Potentiel mBJ

The most commonly used approximations (LDA, LSDA, GGA, and DFT + U) can not accurately predict the gap energy of semiconductors and insulators, where they underestimate the value of this energy.

For this, in 2006 Becke and Johnson [113] proposed a version of the exchange potential (BJ). It was modified and published by Tran and Blaha in 2009 [114] to become the modified Becke Johnson Potential (mBJ), which makes it possible to calculate the gap energies of the solids with a better precision. It is written according to the following form:

$$V_{x,\sigma}^{TB-mBJ}(r) = cV_{x,\sigma}^{BR}(r) + (3c-2)\frac{1}{\pi}\sqrt{\frac{5}{6}}\sqrt{\frac{t_\sigma(r)}{\rho_\sigma(r)}} \quad \text{(III.28)}$$

$\rho_\sigma(r) = \sum_{i=1}^{N_\sigma}\left|\phi_{i,\sigma}(r)\right|^2$ Electron density

$\mathrm{t_\sigma(r)} = \frac{1}{2}\sum_{\mathrm{i=1}}^{\mathrm{N_\sigma}} \nabla\, \phi^*_{\mathrm{i},\sigma}(\mathrm{r})\nabla\phi_{\mathrm{i},\sigma}(\mathrm{r})$ Kinetic energy density

The parameter c is given by the following relation:

$$c = \alpha + \beta\left(\frac{1}{V_{cell}}\int\frac{|\nabla\rho(r\prime)|}{\rho(r\prime)}d^3r'\right)^{\frac{1}{2}} \quad \text{(III.29)}$$

With: V_{cell} is the volume of the elementary cell, α and β are two independent parameters whose values are: α = - 0.012 and β = 1.023 $Bohr^{1/2}$. These two parameters are obtained according to an adjustment to the experimental results.

And $V_{x,\sigma}^{BR}$ in equation (III.28) represents the potential of Becke-Roussel (BR) [115] which has been proposed to model the Coulomb potential created by the exchange hole, and it is given by the following formula:

$$V_{x,\sigma}^{BR}(r) = -\frac{1}{b_\sigma(r)}\left(1 - e^{-x_\sigma(r)} - \frac{1}{2}x_\sigma(r)e^{-x_\sigma(r)}\right) \quad \text{(III.30)}$$

Where: The term $x_\sigma$is determined from a non-linear equation containing $\rho_\sigma(r)$, $\nabla\rho_\sigma(r)$, $\nabla^2\rho_\sigma(r)$, $t_\sigma(r)$, and the term $b_\sigma(r)$ is calculated by the following relation:

$$b_\sigma(r) = \left[\frac{x_\sigma^3(r)e^{-x_\sigma(r)}}{8\pi\rho_\sigma(r)}\right]^{\frac{1}{3}} \quad \text{(III.31)}$$

III.5 Full-Potential Linearized Augmented Planewave Method

The choices made to simplify the resolution of Kohn Sham's equations are based mainly on two points:

Indeed, different calculation methods have been developed based on the formalism of the DFT. The choices made to simplify the solving of Kohn Sham's equations are mainly based on two points:

1- The choice of the wave functions basis to project the mono-electronic Kohn-Sham states, these bases of wave functions are classified in three types as follows:

- Linear combination of atomic orbitals **LCAO**
- Plane waves **PW**
- Linearized augmented plane wave **LAPW**

2- Choice of the form of the effective potential generated by an infinite number of nuclei or ions, that is to say, the external potential, where we can cite three forms of the potential:

- The jellium model.
- The pseudopotential method.
- The all electron method

In this manuscript, we are interested only in the description of a single approach implemented in our "WIEN2K" calculation code: **Full-Potential Linearized Augmented Planewave Method** (FP-LAPW).

III.5.1 Augmented Plane wave Method

In 1937, Slater [116] stipulated that the solution of the Schrödinger equation for a constant potential is a plane wave, with a view of a base that uses functions other than plane waves, whereas for a spherical potential it is a radial function.

However to describe the crystalline potential it is necessary to introduce the Muffin tin approximation, according to this, the unit cell is divided into two types of regions, illustrated in Figure III.2, such as:

- The region inside atomic sphere "tin muffin" defined by spheres of radius Rα Rβ, respectively, which do not overlap. The latter is considered as the first region, in which the potential is spherically symmetrical and the radial solutions of the Schrödinger equation are employed.
- The second region that describes the remaining interstitial region with basic waveband expansion and potential is considered constant.

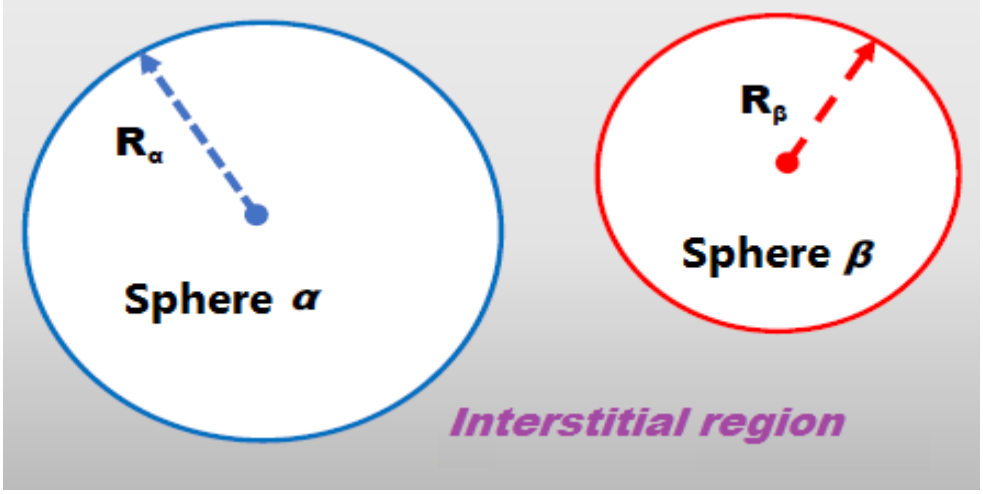

Figure III.2: *Distribution of the unit cell into atomic spheres α & β and into interstitial region.*

The two regions are defined by the wave functions S and I respectively for spherical and interstitial regions as follows:

$$\varphi_s(r) = \sum_{lm} A_{lm} U_l(r) Y_{lm}(r) \qquad \text{where} \quad r < R_\alpha \qquad \text{(III.32)}$$

$$\varphi_I(r) = \frac{1}{\Omega^{1/2}} \sum_G C_G e^{i(G+K)r} \qquad \text{where} \quad r > R_\alpha \qquad \text{(III.33)}$$

Where Ω is the volume of the cell, A_{lm} and C_G are the coefficients of development in spherical harmonics, $Y_{lm}(r)$ is the position in polar coordinates inside the sphere. K is the wave vector in the irreducible Brillouin zone (IBZ), G vector of reciprocal space. The function $U_l(r)$ is the numerical solution of the radial part of the Schrödinger equation with the energy E_l written in the form:

$$\left\{-\frac{d^2}{dr^2}+\frac{l(l+1)}{r^2}+V(r)-E_l\right\}rU_l(r)=0 \qquad \text{(III.34)}$$

$V(r)$ and E_l respectively represents the Muffin-tin potential and the linearization energy.

The radial functions indicated by equation (III.34) are orthogonal to any proper state of the core, where this orthogonality disappears on the border of the sphere [117, 118]. The overlap of these is constructed from:

$$(E_2-E_1)rU_1U_2=U_2\frac{d^2rU_1}{dr^2}-U_1\frac{d^2rU_2}{dr^2} \qquad \text{(III.35)}$$

With U_1 and U_2 are the radial solutions corresponding respectively to energies E_1 and E_2. Slater introduces an approximation, called the muffin-tin approximation (MT), where he justifies the particular choice of these functions [118-121], presenting the plane waves as solutions of the Schrödinger equation in a constant potential.

The fact that the representations defined in the expressions (III.32) and (III.34) are continued on the limits of the MT spheres, is necessary, therefore the coefficients A_{lm} must be defined according to the coefficient C of the plane waves existing in the interstitial regions. Where the latter is expressed as follows:

$$A_{lm}=\frac{4\pi i^l}{\Omega^{1/2}U_l(R_\alpha)}\sum C_G j_l(|K+G|R_\alpha)Y_{lm}(K+G) \qquad \text{(III.36)}$$

j_l is Bessel's function and the origin is taken at the center of the sphere. R is the radius of the MT sphere.

In this method (APW), the plane waves C_G and the parameters of the energy E_l are called the variational coefficients, where the coefficients A_{lm} are determined from these two coefficients C_G and E_l. On the other side, the individual functions indicated by G also become compatible with the radial functions in the spheres, where we can obtain augmented plane waves (APW).

III.5.2 Linearized Augmented Plane wave Method

The linearized augmented plane wave method (LAPW) [122, 123] was proposed in 1975 by Anderson [124] in which, he conceives a linearization of the APW method, where this method was intended to solve the Kohn and Sham equations in order to find the density of the ground state. In those equations, the energy of each radial wave function at the inside of atomic spheres MT is linearized, taking a linear combination of the radial functions $U_l(r)$, $Y_{lm}(r)$ and their derivatives $\dot{U}_l(r), Y_{lm}(r)$, with respect to energy.

$$\phi(r) = \begin{cases} \frac{1}{\Omega^{1/2}} \sum_G C_G e^{i(G+K)r} & r > R_\alpha \\ \sum_{lm} \left[A_{lm} U_l(r) + B_{lm} \dot{U}_l(r) \right] Y_{lm}(r) & r < R_\alpha \end{cases} \quad \text{(III.37)}$$

Where the $U_l(r)$functions have the same determination established in the APW method (Equation III.35), B_{lm} are coefficients of the same nature as the coefficients A_{lm} and they correspond to the function $\dot{U}_l(r)$, in which the function $U_l(r)$, $Y_{lm}(r)$ must satisfy the following condition:

$$\left\{ -\frac{d^2}{dr^2} + \frac{l(l+1)}{r^2} + V(r) - E_1 \right\} r\dot{U}_1(r) = rU_1(r) \quad \text{(III.38)}$$

III.5.3 Full Linearized Augmented Plane wave Method

In the Full Potential Linearized Augmented Plane Waves (FP-LAPW) method [125], no approximation is made for the shape of the potential or the charge density. They are rather developed in harmonics of the network inside each atomic sphere, and in Fourrier series in the interstitial regions. Which is at the origin of the name "Full-Potential".

This method thus ensures the continuity of the potential at the surface of the sphere MT and is developed in the following form:

$$V(r) = \begin{cases} \sum_K V_K e^{iKr} & r > R_\alpha \\ \sum_{lm} V_{lm}(r) Y_{lm}(r) & r < R_\alpha \end{cases} \quad \text{(III.39)}$$

In the same way, the charge density is developed in the form:

$$\rho(r) = \begin{cases} \sum_K \rho_K e^{iKr} & r > R_\alpha \\ \sum_{lm} \rho_{lm}(r) Y_{lm}(r) & r < R_\alpha \end{cases} \quad \text{(III.40)}$$

III.6 WIEN2k package

The Wien2k is a simulating calculation code developed by Blaha, Schwartz and Luitz [126, 127] from the Institute of Chemistry of materials in the Technical University of Vienna (Austria).

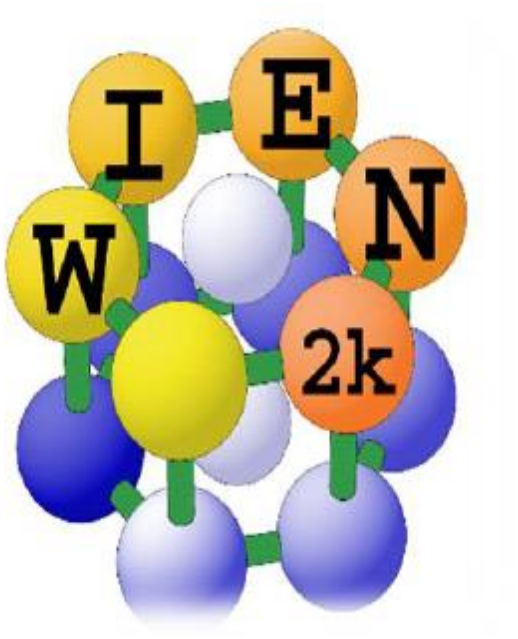

This code was first distributed in 1990, it has been continuously revised since then and has undergone several updates. The versions launched later are named according to the year of their publication (WIEN93, WIEN95 and WIEN97… WIEN2016… etc.). This simulation code is a computer program written in FORTRAN language and works under a UNIX operating system, it is based on the density functional theory and method (FP-LAPW). It consists of several independent programs which are linked by a C-SHEL script allowing to perform self-consistent calculations and for each calculation we will specify the important procedures which are as follows:

III.6.1. Insert of parameters:

In this step, we fill an input file called **case.struct** (Meaning: material name. Struct) with the following atomic parameters:

- Type of the crystal lattice.
- The space group.
- The lattice parameters (a, b and c in Bohr or Å).
- The angles (α, β and γ).
- The atom's positions inside the cell (x, y and z).
- The radii of muffin-tin (RMT), given in atomic units (radius of Bohr).

III.6.2. initialization:

After having generated this file "case.struct", we carry out the initialization by the command "init_lapw" to start several programs and executing in a successive way; these programs are as follows [128]:

- **NN:** It is a program which gives for each atom, the list of its first neighbors and the distances between the closest neighbors. Thus it makes it possible to determine the atomic radius of the sphere and checks the overlapping of the muffin tin spheres; the output file for this program is called **cas.output nn.**
- **SGROUP:** This program makes it possible to determine the space group of the structure which is defined in the file cas.struct, and all the point groups of nonequivalent sites,

thus a new structural file is produced with the appropriate type of network called cas.struct-sgroup.

- **SYMMETRY:** is a program, which lists the symmetry operations of the spatial group and saves them in the file called "case.struct_st", it determines the point group of the different atomic locations and highlights the quantum numbers (l, m) for spherical harmonics materialized in file "case.in2_st".
- **LSTART:** A program, which generates the atomic densities and determines how the different orbitals are treated in the calculation of the band structure, like core states with or without local orbitals.
- **KGEN:** generates a k-mesh in the irreducible part of the Brillouin zone (B.Z).
- **DSTART:** this program generates an initial charge density for the SCF cycle "self-consistent" cycle by superimposing the atomic densities generated in LSTART, the information will be written in the file "case.clmsum".

III.6.3. Self-consistent calculation

When the initialization steps are complete, the SCF "Self Consistent Field" cycle processes are then launched and iterated until the solution converges.

- **LAPW0:** Generates the potential from the density.
- **LAPW1:** Calculates the matrix coefficients of the Hamiltonian in the LAPW wave base and finds, by diagonalization, the eigenvalues and the eigenvectors.
- **LAPW2:** It determines the Fermi level, the expansions of valence electron densities made up of electron densities inside each MT sphere and in the interstitial region.
- **LCORE:** Calculates the core states inside the M spheres, keeping only the spherical part of the potential.
- **MIXER:** calculates the new electron density by mixing the electron densities of the core, semi-core states and valence states in order to generate the input density for the next iteration.

These main calculation steps using the Wien2k code are illustrated in Figure I.4 below:

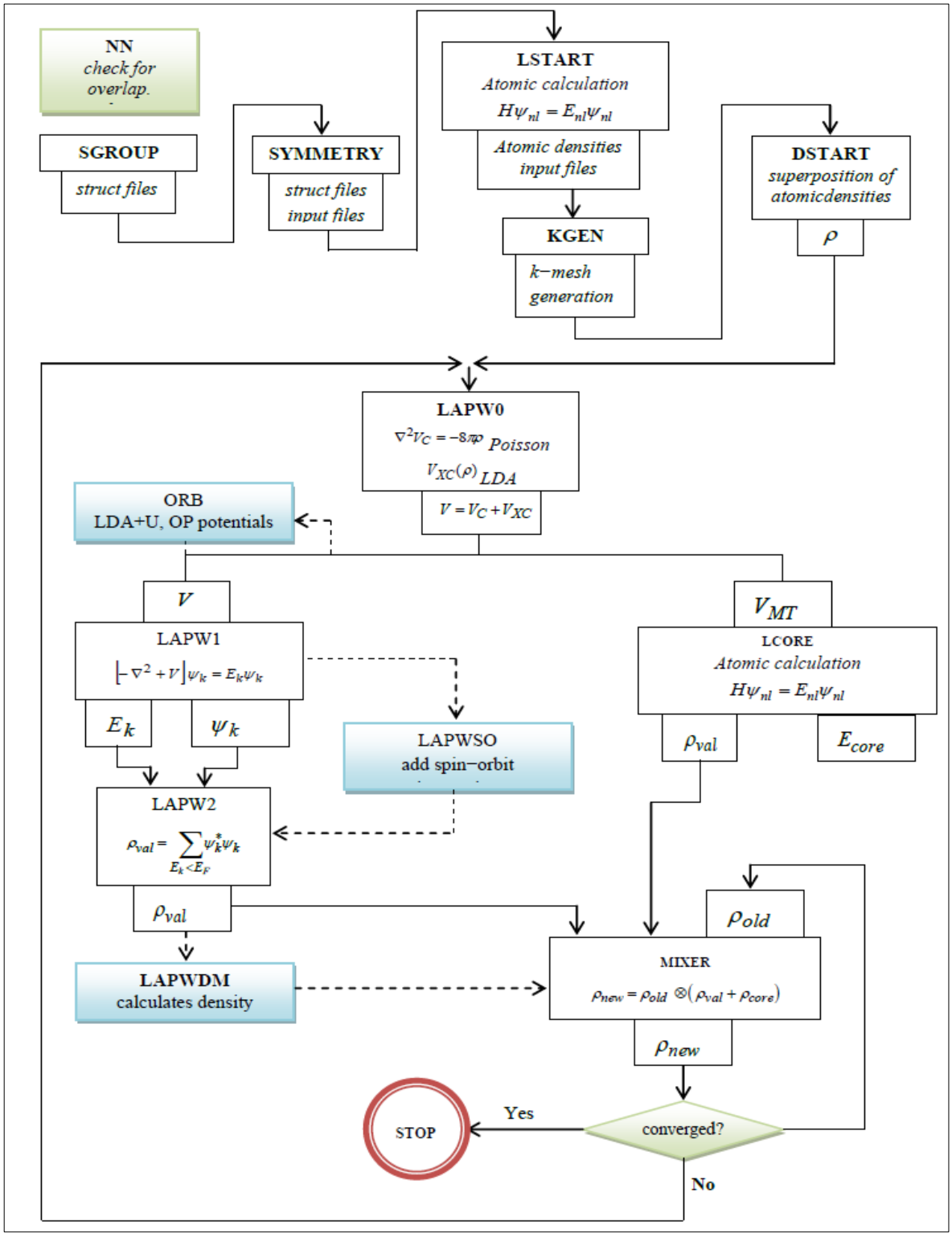

Figure III.3: *Program flow in Wien2k.*

III.6.4. Determination of properties

Once the Self Consistent Field SCF has been completed, several properties can be determined, including: the band structure, the density of states, the charge density and the optical properties... etc.

Chapter IV

Structural, optical and electronic properties of copper oxide CuO

IV.1 Introduction:

Copper oxide CuO is considered one of the oldest semiconductor materials studied since 1920 with the chemical formula CuO. It has attracted the attention of the scientific community because of its interesting physical properties as a p-type semiconductor and its narrow band-gap energy (Eg) ranging from 1.2 to 2.06 eV [129]. This semiconducting nature gives it a real importance in several applications in different scientific and industrial fields such as: such as gas sensors, magnetic storage media, spintronic [130-134], photovoltaic cells [135,136], supercapacitors [137,138], lithium-ion batteries [139,141] and photocatalysis [142].

Previous work carried out in several research laboratories has also developed many techniques and theoretical and experimental methods in order to determine the physical properties of semiconductor materials.

Theoretical studies based on analytical models of numerical simulations, among these methods, the theory of functional density (DFT), based on Ab initio techniques [145,146], which allow to model solid materials like CuO and to study its electronic structure and its physical properties.

There have been many experimental researches to evaluate copper oxide properties at nanoscale in different synthesis forms (thin films, nanoparticles…). The synthesis procedure plays a crucial role in controlling the size, the shape of the nanostructure and hence detecting different properties of the material. Various methods are used for the synthesis of CuO nanoparticles including sol-gel [147], solid-state reaction, microwave irradiation and thermal decomposition. Among all the processes sol-gel method was reported as having many advantageous aspects as pointed out by Chand & al [147], such as producing materials at ultra-low temperatures, synthesizing almost any material, co-synthesizing two or more materials simultaneously, controlling the microstructure, the physical, the mechanical and the chemical properties of the final products etc..[148].

The aim of this chapter is to present our results on copper oxide according to two parts:

The first part being to present a theoretical study leading to investigate the structural, electronic, optical properties for CuO supercell (nanoscale approach), which are obtained by means of ab initio calculations within the framework of the density functional theory (DFT) using the potential Becke-Johnson modified (mBJ) implemented in the Wien2k code.

The second part we are reporting the experimental approach used in our study for the production of copper oxide NPs via the sol-gel method through the reduction of copper acetate in water as a solvent. The as-prepared nanoparticles are characterized by X-ray diffraction (XRD), UV-Vis spectrophotometer and transmission electron microscopy (TEM). The obtained nanoparticles are then annealed at different temperatures to study the effect of temperature and particles size on their morphological, optical and potential photocatalytic properties.

The photocatalytic activity of the obtained NPs examined using the degradation of methylene blue (MB) under UV and visible light in four different annealing temperature to see how we can control the photodegradation of the material for each temperature.

IV.2 Abinitio study on CuO

The structural, electronic and optical properties of CuO copper oxide have been examined using the Linearized Augmented Plane Wave (FP-LAPW) method [125] implemented in the Wien2k code [128] in the framework of the DFT. Non-relativistic calculations were performed. Generalized Gradient Approximation (GGA) suggested by Perdew, Burke and Ernzerhof (PBE) is used for evaluating the exchange correlation energy [149] for structural properties, and the modified Becke and Johnson (mBJ) potential for electronic and optical properties. The latter

approach is reputed to give good results for the band gap as well as the band structure of the material. The cut-off vector that defines the separation between heart states and valence states is -8 Ry. The muffin-tin radius is chosen to be respectively 1.66 a.u, 1.34 a.u for the Cu and O atoms respectively. The cutoff energy as well as the number of k points, have been optimized so that the total energy converges with an accuracy of 10^{-5} Ry. The electronic configuration of copper and oxygen are [Ar] 3d104s1 and [He] 2s22p4 respectively. For more accuracy with experimental work, supercell is built containing 46 atoms.

IV.2.1 Structural properties:

The optimized three dimensional (3D) crystal structures of 2×2×2 supercell containing 46 atoms of Cu and O and primitive cell of CuO containing 6 Cu atoms and 2 O atoms are illustrated in Fig. X. The optimization is ended by minimizing the energy from the structure with respect to the volume of the system cell.

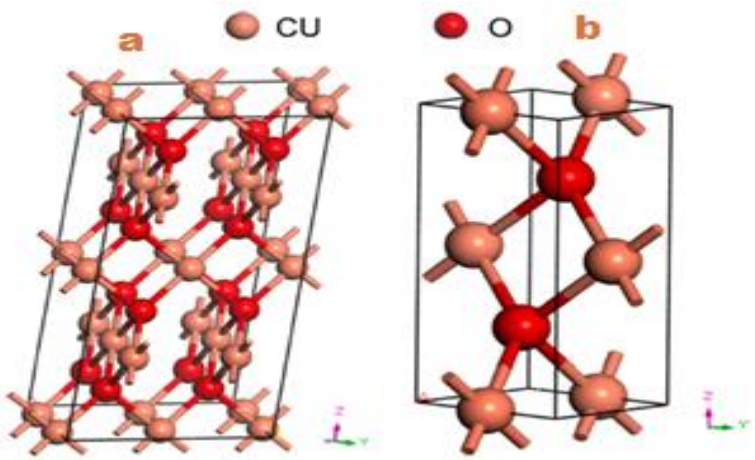

Figure IV.1: *crystal structure of CuO (a) (2×2×2 supercell) and (b) primitive cell.*

The CuO material crystallizes under ambient conditions (temperature and pressure) in the monoclinic structure [150-153], which belongs to the C2/c space group. The calculations of total energies according to the volume were carried out in order to have the parameters of the network and the modulus of compression. These parameters are calculated by adjusting $Etot$ by the Murnaghan state equation [154] given by the following formula:

$$E(\mathrm{V}) = \mathrm{E}_0(\mathrm{V}) + \left[\frac{\mathrm{B}_0\mathrm{V}}{\mathrm{B}\prime(\mathrm{B}'-1)}\right] \times \left[\mathrm{B}_0\left(1-\frac{\mathrm{V}_0}{\mathrm{V}}\right) + \left(\frac{\mathrm{V}_0}{\mathrm{V}}\right)^{\mathrm{B}\prime} - 1\right] \qquad \text{(IV.1)}$$

Where :

E and V are the total energy and the lattice volume respectively.

E_0 and V_0 are the total energy and the lattice volume at equilibrium respectively.

B_0 and B' are bulk modulus and its pressure derived respectively.

The compression modulus is evaluated at the minimum of the curve E (V) by the relation:

$$B_0 = V\frac{\partial^2 E}{\partial V^2} \qquad \text{(IV.2)}$$

The variations of the total energy as a function of the volume are shown in the figure (IV.2).

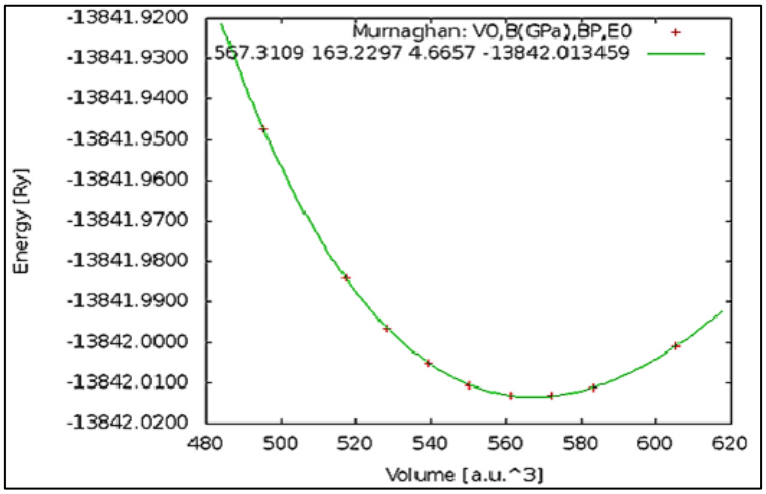

Figure IV.2: *Variation of total energy as function of volume.*

Table IV.1*: Comparison of CuO monoclinic structural parameters*

	Lattice parameters (Å)				Interatomic distances			Volume (Å^3)
CuO	a(Å)	b(Å)	c (Å)	γ(Å)	d_{Cu-Cu}	d_{Cu-O}	d_{O-O}	V
Our work	*4.685*	*3.390*	*5.139*	*99.54*	*2.88*	*1.96*	*2.63*	*81.08*
Theoretical results[155]	*4.36*	*3.86*	*5.16*	99.54	____	____	____	____
Experimental values[156]	*4.6915*	*3.4127*	*5.2527*	*99.54*	*2.9*	*1.95*	*2.62*	____

The lattice parameters of the monoclinic copper oxide are compared with experimental results and other calculations are grouped in Table IV.1.

IV.2.2 Electronic properties:

IV.2.2.1 Band structure

The electronic band structure (BS), total density of states (TDOS) and partial density of states (PDOS) have been used to find out the electronic structure of CuO. The band structure gives information about the nature of the material; i.e. conductor, semiconductor and insulator.

The density of states (DOS) of a system describes the number of states occupied at each energy level in statistical and solid state physics [157].

Fig IV.3&4 illustrates the diagram of BS of pure monoclinic CuO obtained by the GGA and mBJ approximation respectively. Fermi level is indicated by the red line. We can clearly see that there is a difference between the two calculation methods. From fig IV.3, we can see that three electronic levels crossed the Fermi surface, which is set at 0, thus there is no energy gap and CuO is predicted to have a metallic or semi-metallic ground state, Heinemann and Nolan have also reported a gap value of 0 eV for the pure CuO [173,174].

In the other hand, the band structure calculated by mBJ shows no electronic levels crossed by the Fermi surface. Our calculated band gap value is energy gap 1.89 eV is also close to the experimental values between {1.7-3.5 eV} [175,176].

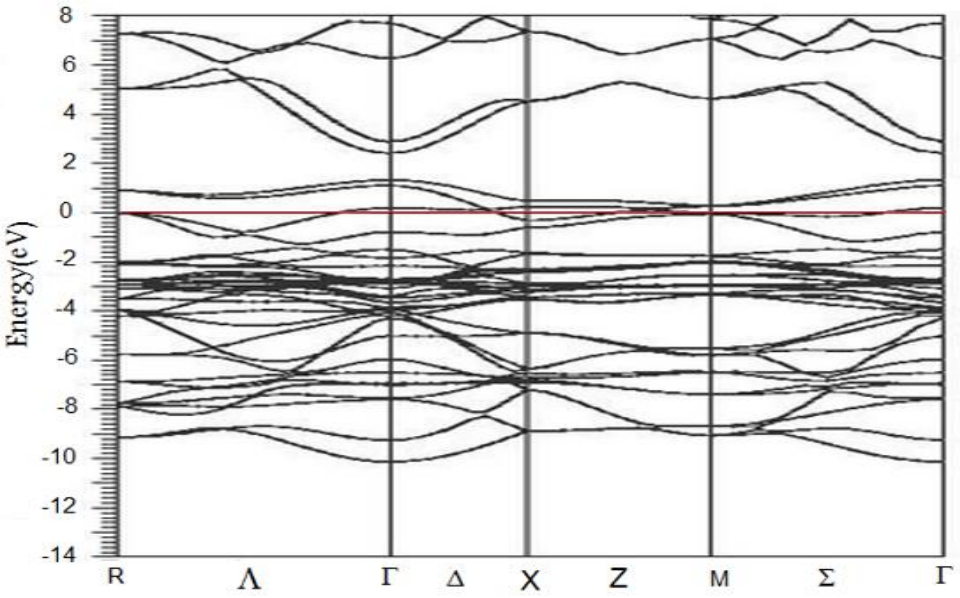

Figure IV.3: *Band structure of pure CuO obtained by the GGA-PBE approximation.*

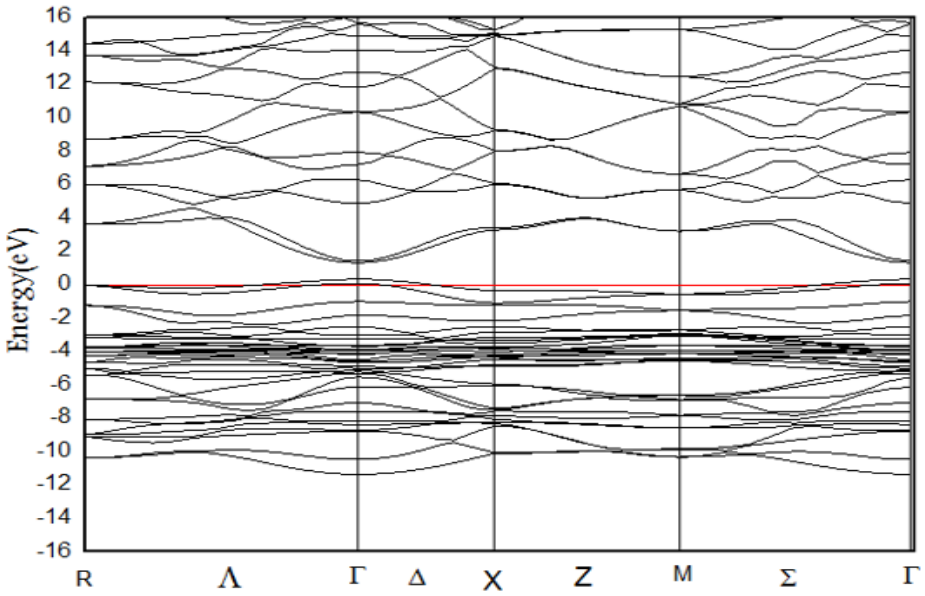

Figure IV.4: *Band structure of pure CuO obtained by mBJ approximation.*

IV.2.2.2 Density of states:

The density of the states quantifies the number of electronic states having a given energy in the material considered. In other words, it represents the number of states available to electrons. It is a function that only depends on energy. The projected total and partial densities of states (DOS), between −9 and 3 eV calculated respectively by the mBJ method and illustrated in figure IV.5, the Fermi level is taken as the origin of the energies.

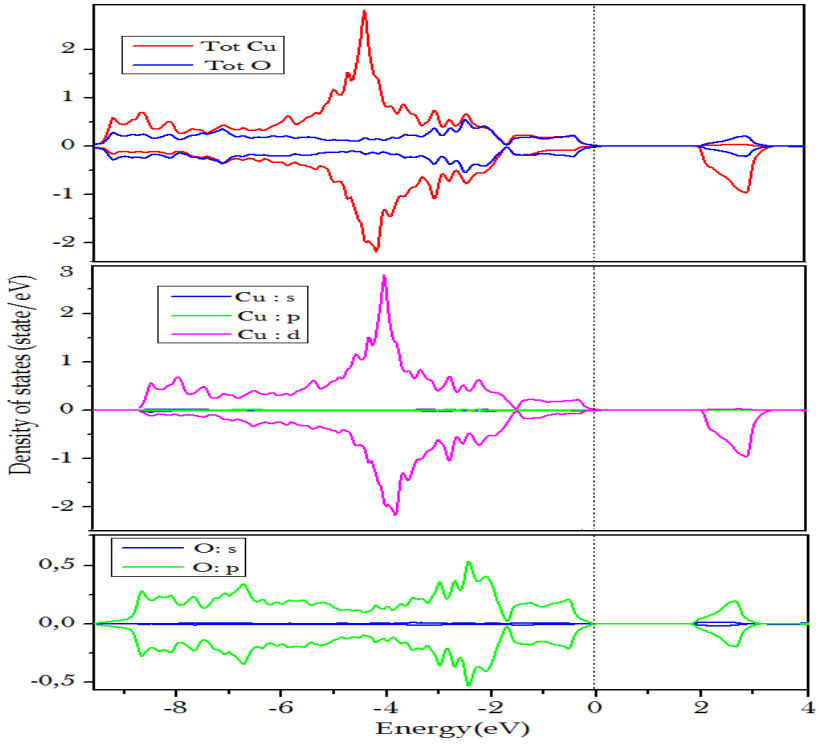

Figure IV.5: *The total and partial density of states of pure CuO by mBJ approximation.*

The figure reveals that the first valence region is located between [-9.5 eV, -2.05 eV], this region is entirely composed of a contribution from the 2p and 2d states of oxygen and copper respectively, this is mainly due to the hybridization between O "p" states and Cu "d" state. The second valence band is located between [-1.85 eV and 0.02 eV]. These are mainly "d" states of Cu and a small amount of O "p" states. The last region [1.98 eV to 3.16 eV] is a conduction band dominated mainly by the p-O states and the peaks of the d-Cu states. We note that there is no symmetry between the spin up and down configuration of the state density of the copper element, which indicates that it is responsible for obtaining an antiferromagnetic structure. These suggest that the mBJ method proves good agreement with other theoretical results [158-160].

IV.2.3 Optical properties

It is of great interest to know the different ways in which light interacts with matter in solid state physics, for example absorption, transmission, reflection, scattering and emission. Studying the optical properties of solids has proven to be a powerful tool in our understanding of the electronic properties of materials.

Thus, the DFT makes it possible to calculate all the optical properties, namely the refractive index, the extinction coefficient, the absorption coefficient, which are deduced from the complex dielectric function ε (ω).

IV.2.3.1 Dielectric function ε (ω):

The dielectric function ε (ω) is used to describe the material's linear response to electromagnetic radiation, which is linked to the interaction of photons with electrons. The dielectric function is determined by the electronic transitions between the valence band and the conduction band. It is calculated by evaluating the matrix elements in representation of the impulse.
It brings into play a real part (the dispersive part) and an imaginary part (absorptive part), using the formalism of Ehrenreich and Cohen, in the form of the following formula:

$$\varepsilon(\omega) = \varepsilon_1(\omega) + i\,\varepsilon_2(\omega) \qquad \text{(IV.3)}$$

The imaginary part $\varepsilon_2(\omega)$ is given by the following relation:

$$Im\ \varepsilon(\omega) = \varepsilon_2(\omega) = \frac{4\pi^2 e^2}{m^2\omega^2}\sum_{i,j}|< i|M|j >|^2 \times \left(f_i(1-f_i)\right)\delta(E_f - E_i - \hbar\omega)d^3k \qquad \text{(IV.4)}$$

M represents the matrix elements for the transitions between the valence band and the conduction band, with e and m are the charge and the mass of the electron respectively. ω is the frequency of the incident photon, f_i is the Fermi distribution function for the i^{th} state, E_i the energy of the

electron in the i^{th} state; i and j are initial and final states, respectively. The imaginary part $\varepsilon_2(\omega)$ of the dielectric function depends on the electronic transition at the origin of the absorption.

The real part $\varepsilon_1(\omega)$ of the dielectric function can be obtained from the imaginary part $\varepsilon_2(\omega)$ using the following Kramers-Kronig relation:

$$\varepsilon_1(\omega) = 1 + \frac{2}{\pi}\int_0^{\infty} \frac{\varepsilon_2(\omega')\omega' d\omega'}{\omega'^2 - \omega^2} \qquad \text{(IV.5)}$$

Figures IV.6 (a,b) show the evolution of the imaginary and real part of $\varepsilon(\omega)$ respectively in the energy range [0-13] eV, obtained by the mBJ method.

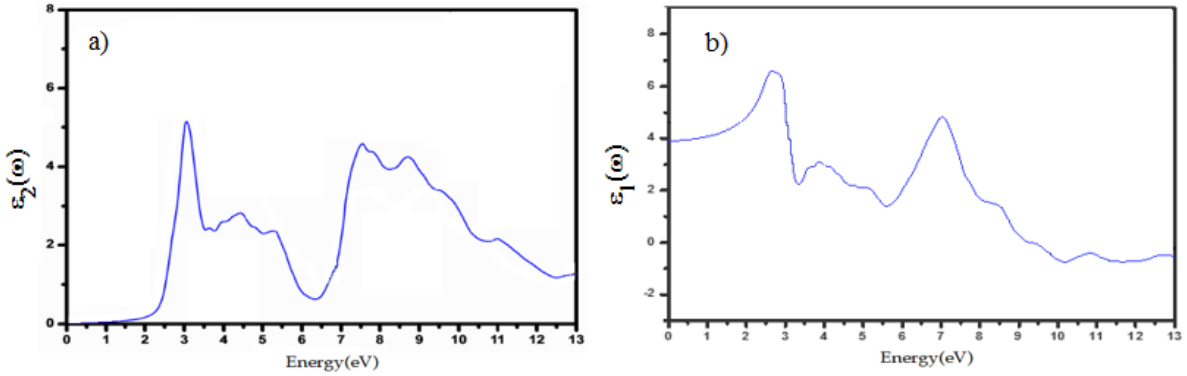

Figure IV.6: *Imaginary part (a) and real part (b) of the dielectric function.*

The imaginary part of the dielectric function is directly linked to the electronic band structure in a material.

Analysis of the peaks in this section for copper oxide (CuO) reveals threshold peaks at 3.04 eV, in agreement with the others theoretical results [158-160]. We also note the existence of another peak near 7.54 eV, these peaks are mainly due to the transition of the electrons from the Cu '2d orbitals 'and O' 2p '.

The Figure shows a high intensity peak around 2.62 eV. The intensity of $\varepsilon_1(\omega)$ begins to increase with energy until reaching peaks at 7.02 eV then decreases until crossing zero at 9.41eV.

IV.2.3.2 Absorption coefficient $\alpha(\omega)$:

The absorption coefficient $\alpha(\omega)$ characterizes the part of energy absorbed by the solid. It determines how far light of a particular wavelength can penetrate a material before it is absorbed. The absorption coefficient depends on the material and also on the wavelength of the light that is absorbed. The absorption function can be calculated by the following relation:

$$\alpha(\omega) = \frac{2\pi\omega}{C}\sqrt{\frac{-\mathrm{Re}(\varepsilon(\omega)) + |\varepsilon(\omega)|}{2}} \qquad \text{(IV.6)}$$

The evolution of the absorption coefficient is shown in Figure IV.7. We notice that the absorption starts from the energies 1.92 eV. The absorption coefficient begins to increase until reaching a first maximum at 3.1 eV, then another for energies 5.39 eV, then, it begins to decrease until reaching a minimum for an energy of approximately 6.37 eV. We also note that the maximum absorption is located in the energy range [6.7-11 eV].

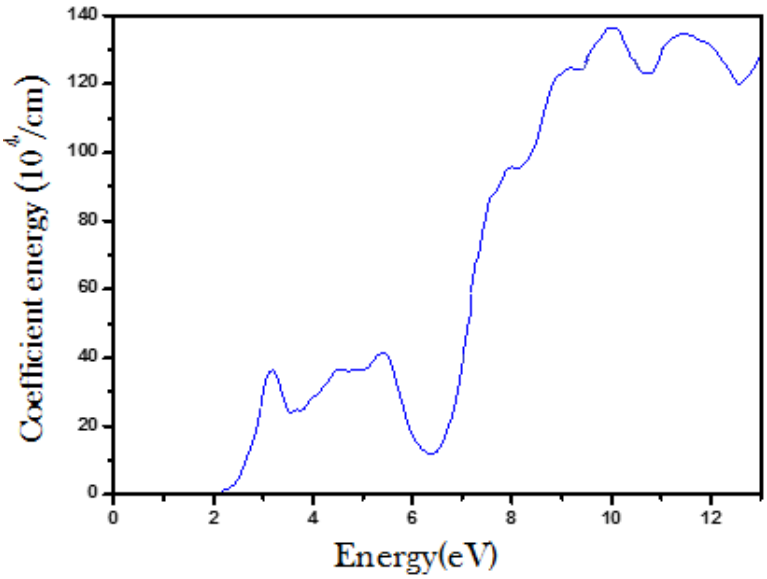

Figure IV.7: *The absorption coefficient.*

IV.2.3.3 Optical conductivity σ (ω):

The term "optical conduction" means electrical conduction in the presence of the electric field included in light. The real part of the optical conductivity is calculated according to the following relation:

$$Re\ \sigma(\omega) = \frac{\omega}{4\pi} Im\ \varepsilon(\omega) \qquad \text{(IV.7)}$$

The variation of the optical conductivity is shown in the figure (IV.8). From Figure (IV.8), the optical conduction starts from the energies of about 1.81 eV. This value represent the optical energy gap and arrives at a maximum level for 3.04 eV. Indeed, in the region [1.32-6.65 eV], it reach a minimum at 6.3 eV then it begin to increase again to arrive at another maximum greater than the first at 8.67 eV.

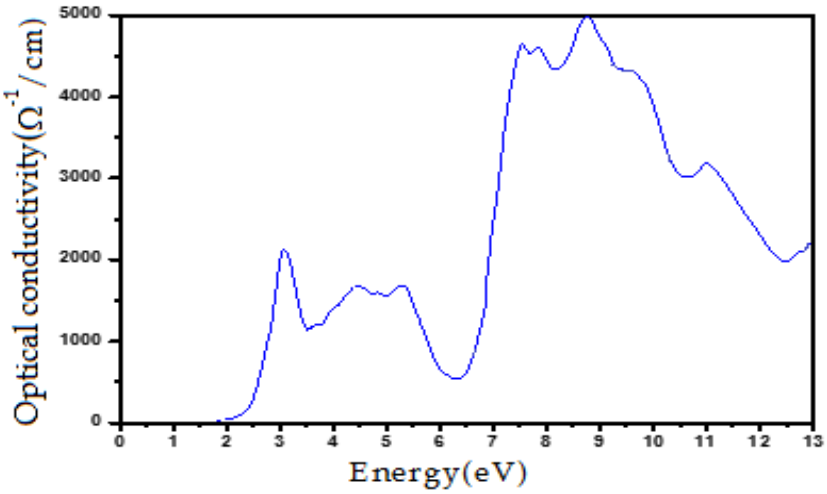

Figure IV.8: *The variation of the optical conductivity as a function of energy (eV).*

IV.2.3.4 Refractive index n (ω):

When designing optoelectronic devices, one always needs to know the spectrum of the refractive index [161], which can be obtained from that of the dielectric function.

The propagation of a light beam through a translucent medium is described by the refractive index n, this latter is defined by the relationship between the velocity of light in free space c and that in the medium υ according to the relationship:

$$n = \frac{c}{\vartheta} \qquad \text{(IV.8)}$$

The refractive index depends on the frequency of the light beam, this effect is called dispersion. The refractive index n (ω) is calculated by the following relation:

$$n(\omega) = \left[\frac{\sqrt{\varepsilon_1^2 + \varepsilon_2^2} + \varepsilon_1}{2}\right]^{1/2} \qquad \text{(IV.9)}$$

The refractive index represents the dispersion behavior of the material. Its evolution is shown in the following figure:

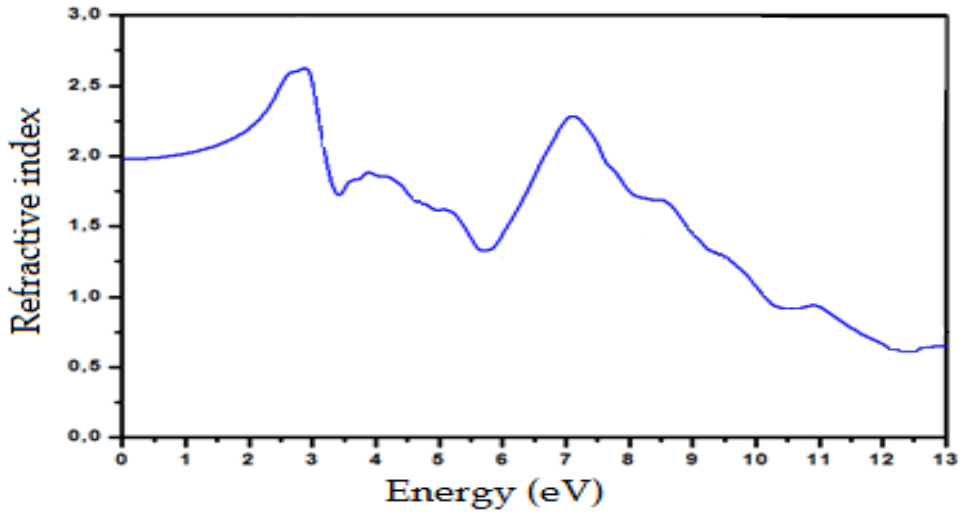

Figure IV.9: *Variation of Refractive index spectra as a function of energy (eV) of pure CuO.*

Indeed, the refractive index could be linked to the static dielectric constant by $n\,(0)=\sqrt{\varepsilon_1}(0)$ [162].

According to the figure (IV.9), the spectra begin to increase until reaching a maximum at 2.87. The refractive index begins to decrease to a minimum, at energies 5.59 eV, then they increase for another maximum to 7.07 eV, in this case, the intensity is higher, the spectra decrease until it crosses 1, from this minimum, the variation of the index of refraction is low and therefore the dispersion is very low. We note that the dispersion phenomenon is very important in the visible spectrum region.

IV.2.3.5 Reflectivity *R*(ω):

The reflection phenomenon which occurs at the front and rear surfaces is described by the reflection coefficient which represents the ratio between the energy reflected and the energy incident on the surface. It can be determined from the real and imaginary parts of the dielectric function, given by the following relation:

$$R(\omega)=\left|\frac{1-n(\omega)}{1+n(\omega)}\right|^2 \qquad \text{(IV.10)}$$

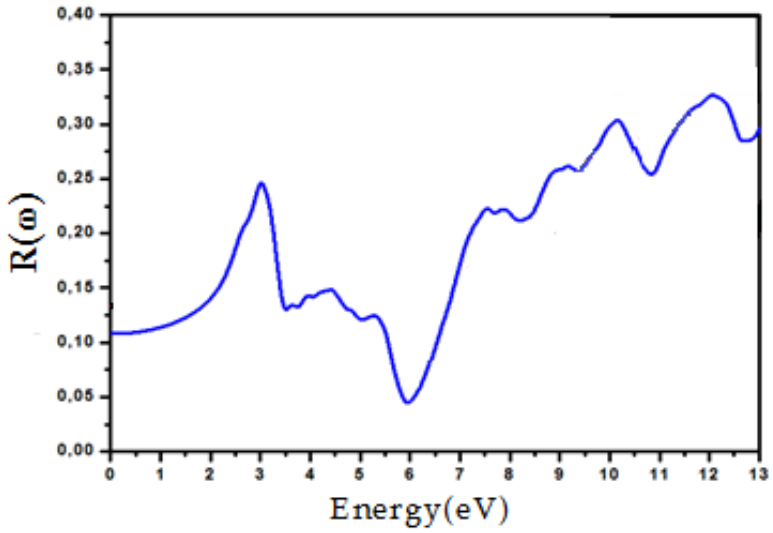

Figure IV.10: *The reflectivity spectra of CuO.*

Figure IV.10 illustrates the reflectivity spectrum of copper oxide CuO.

Reflectivity represents the amount of energy reflected relative to the incident energy. The static values of the reflectivity are 0.1. It begins to increase until reaching maximum values of 3.02 eV. The average values of the reflection coefficient in the visible spectrum region as well as in the [7-13 eV] region show that the material is semi-transparent in this energy region. We note that the maximum reflection occurs when $\varepsilon_1(\omega)$ goes towards negative values.

IV.3 Experimental study: Effect of annealing temperature on CuO NPs properties

IV.3.1 Synthesis protocol of CuO NPs

IV.3.1.1 Precursor used:

The quality of the powders produced by the sol gel route depends closely on the properties of the precursors used.

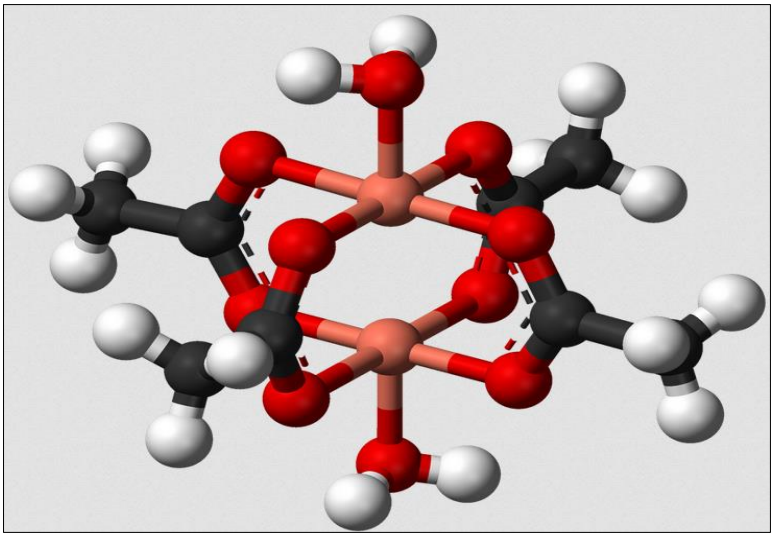

Figure IV.11: *Structure of* copper (II) acetate hydrate; *Atoms: Cu-pink, O-red, C-black, H-white,* taken from [163]

The precursor used in this study is copper acetate monohydrate, a chemical compound with the formula [(Cu(CH3COO)$_2$),H_2O], an hydrated derivative form of copper acetate, which is used as an important reagent for the synthesis and production of various inorganic and organic compounds among them the copper oxide in its two forms CuO(II) and Cu2O(I).

The properties of the precursor are listed in Table IV.2:

Table IV.2: *Copper (II) Acetate Monohydrate Properties [164]*

Compound Formula	$C_4H_8CuO_5$
Molecular Weight	199.65
Melting Point	115° C
Boiling Point	240° C
Density	1.88 g/cm^3 at 20° C
Solubility in H2O	Soluble in water (72 mg/ml at 20° C)
Solubility	Soluble in alcohol, slightly soluble in ether and glycerin.

IV.3.1.2 Preparation of the solution:

For the synthesis of CuO nanoparticles in the sol-gel process, 1.98 g of (Cu(CH3COO)$_2$, H_2O) as a precursor were dissolved in 100 ml of water and stirred for 1 hour to get a homogenous solution. Then 0.8 M of NaOH was added to this solution maintained at 60°C under constant stirring during 2 hours.

IV.3.1.3 Centrifugation treatment:

To separate the solid phase from the liquid of the solution, the obtained black precipitate is centrifuged at 5000 rpm during 40 min, washed twice with distilled water, once with absolute ethanol to remove all kinds of impurities.

IV.3.1.4 Drying of powders:

Drying is a low temperature heat treatment to evaporate the solvents trapped in the structure of wet powders. Conventional drying is carried out at atmospheric pressure, either at room temperature or in an oven (but always at a temperature below the boiling point of the solvent).

In our study, the powders obtained after filtration (centrifuged) were dried at 50 °C for 18 h in air.

IV.3.1.5 Heat treatment:

It appears necessary to thermally treat the raw powder in order to obtain crystallized nanoparticles. So in order to evaluate the effect of the temperature on their different physical properties, the samples were annealed under four different on temperatures: 200, 400, 600 and 800°C respectively. For all reactions, the copper acetate, NaOH concentrations, temperature and time of the reaction were maintained constant.

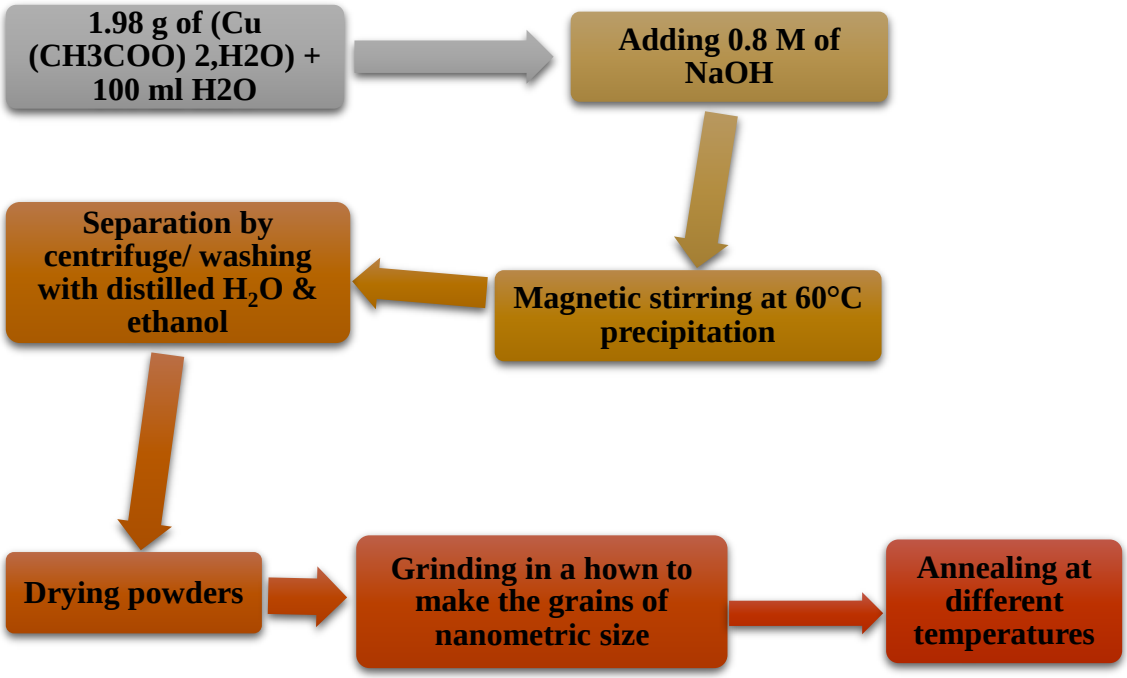

Figure IV.12: *Schematic representation of the CuO NPs production stages by the sol-gel route.*

IV.3.2 Characterization methods

The obtained powders were characterized by X-Ray Diffraction with the use of the Panalytical XPERT-PRO powder diffractometer with the Cu-Kα radiation. The Rietveld refinement was performed using MAUD (material analysis using diffraction) software. The Rietveld routine was performed in the 2θ range from 10° to 90°, using an angular step of 0.03°/min and exposure time of 3s. The morphology of the prepared CuO nanoparticles was carried out using the FEI Transmission Electron Microscopy (TEM, Tecnai G2 12 TWIN, 120KV) with a LaB6 filament. The UV-Visible absorption spectra were recorded using the UV-Visible Perkin Elmer spectrophotometer (Lambda 900), we added Powders into the water and sonicated in an ethanol bath for 10 min to form a homogeneous suspension with the concentration of about 0.1g/5ml.

IV.3.3 Photocatalytic activity

The activity of the annealed CuO NPs was evaluated using methylene blue (MB) under a UV-source functioning as a lamp of the spherical shape of 125W A-B-C (200–600 nm) irradiation. A solid sample (200 mg) was preliminary dispersed in 100mL of a dye solution (10 mgL−1). Before UV irradiation, an adsorption-desorption equilibrium is establishing by stirring during 10 min, based on the kinetics studies shown in (Fig. IV 19), the solution is then, exposed to UV light under magnetic stirring. At each selected time, the suspensions is centrifuging at 14000 rpm for 15 min, and the supernatants are stored in the dark. The concentration of dye remaining in solution C (mg.L−1) is measuring by using a UV-visible spectrophotometer (PerkinElmer Lambda II).

IV.3.4 Results and discussion

IV.3.4.1 *Structural properties*

X-ray diffraction measurements were carried out to study the crystal structure and crystalline quality. (Fig IV.13) represents the XRD patterns of synthesized CuO nanoparticles annealed at 200, 400, 600 and 800 °C, respectively.

It is clear that the intensity of crystalline peaks increases with the increase in temperature indicating the improvement in the crystallinity of samples. Simultaneously, the peaks became narrower as the temperature increase showing the increase in crystallite size and a decrease in the full width at half maximum (FWHM), which indicates a possible change in the grain size of CuO [165,166] that can be well seen from (Table IV.3). In addition, this decrease in the (FWHM) values with the growing temperature indicates the enhancement of the crystallite size of the CuO nanoparticles.

Further, it can also be seen that the major peaks (002) and (111) located at 2θ values, see (Table IV.3) correspond to the characteristic diffraction of monoclinic phase of CuO (JCPDS NO-65-

2309), which concurs Hemanth et al. [148], XRD results thus confirm synthesis of pure and well crystalline CuO nanoparticles without any impurity.

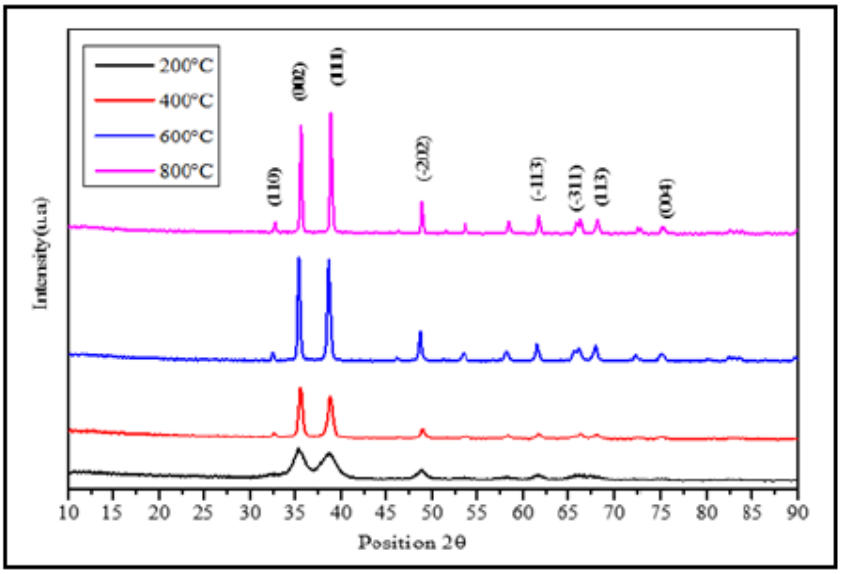

Figure IV.13: XRD patterns of CuO NPs, at different Temperature

Particle size can be calculated by Debye- Scherrer's formula,

$$D = K.\lambda.\beta \cos\theta \qquad \text{(IV.11)}$$

where D is the diameter of the crystallite size, K is the shape factor (the typical value is 0.9), λ is the wavelength of the incident beam, β is the broadening of the diffraction line measured in radians at half of its maximum intensity (FWHM), and θ is the Bragg's angle [167].

Table IV.3: *FWHM values for the two major peaks and particle size values of annealed CuO samples.*

Temperature	(hkl)	2θ	FWHM	Particle size (D)	Particle size from TEM
200°C	002	35.35	0.3296	5.45nm	9.84nm±1.02
	111	38.69	0.8378		
400°C	002	35.62	0.3296	19.35nm	53.41nm±1.77
	111	38.81	0.4615		
600°C	002	35.45	0.2637	68.07nm	131.55nm±3.67
	111	38.63	0.3296		
800°C	002	35.67	0.2637	172.33nm	188.33nm±2.76
	111	38.88	0.2637		

The structural parameters for all the calcined samples were refined using Rietveld refinement method, and are given in (Table IV.4). All the CuO nanoparticles were crystallized in the

monoclinic (tenorite) structure with a space group of C2/c (No.15). The observed lattice parameters agree well with the reported data in the standard JCPDS mentioned before. An example of the observed, calculated and the difference refined XRD patterns of samples annealed at 800°C are shown in Fig. IV.14. There is good agreement between the observed and calculated patterns. Further, there is no appreciable change in the lattice parameters of low-temperature calcined samples.

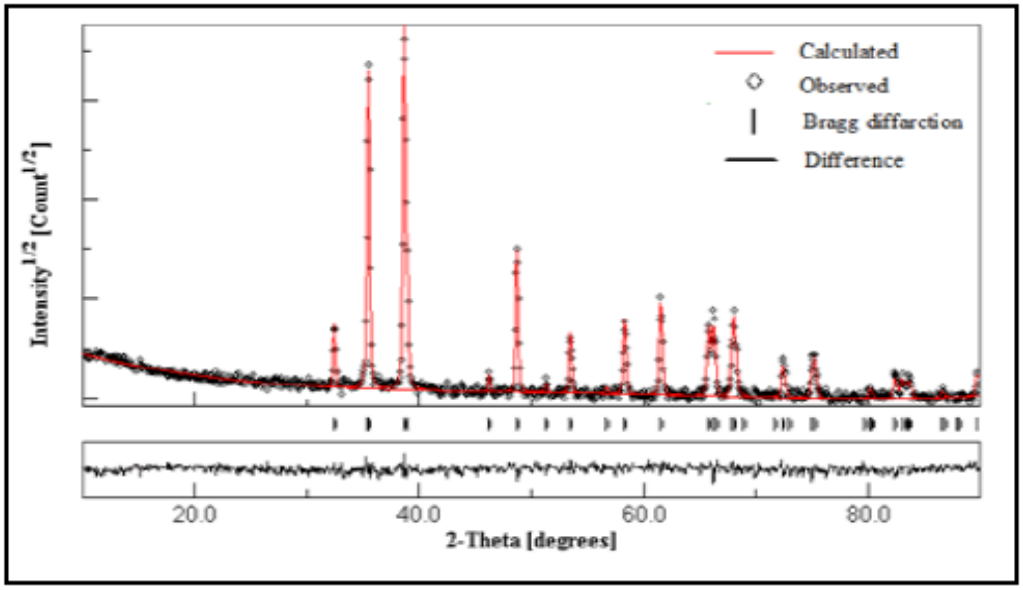

Figure IV.14: Rietveld refinement patterns of X-ray diffraction data for CuO NPs annealed at 800°C.

Table IV.4. Rietveld refined structural parameters for annealed CuO nanoparticles.

Annealed samples	Refined R-Factors			Lattice parameters			
	R_{wp}	R_{exp}	R_{Bragg}	a	b	c	β
200°C	13.729	3.215	8.602	4.6869	3.4306	5.1361	99.298
400°C	10.269	4.123	7.847	4.6808	3.432	5.1336	99.32
600°C	13.62	3.6	9.07	4.68	3.42	5.1331	99.41
800°C	11.33	4.058	5.504	4.69	3.42	5.13	99.49

IV.3.4.2 Morphological studies

(Fig IV.15) (a), (b), (c) and (d) exhibit TEM images and size distribution of CuO nanoparticles annealed at 200°C, 400°C, 600°C and 800°C respectively. As observed from the figure above, the CuO NPs, which were annealed at 200°C and 400°C, are spherical, self-assembled and consisting of particles with unfortunate fusion and aggregation. As the annealing temperature increases to 600°C and 800°C, the sizes of particle are no quite uniform compared with temperatures of 200°C and 400°C as observed from the TEM results, the particles size are not small anymore and begins to agglomerate and becomes larger than those of lower annealing temperature.

This increase of NP's size with calcination temperature is mainly caused by the agglomeration of particles, which means that at raised temperatures, the atoms possess enough energy (the energy needed for oxide molecules to assemble into crystals). Therefore, this energy is communicated to the system by increasing the temperature. Therefore, the molecules are allowed to immigrate towards steady positions and as a consequence, the intensity of peaks and grains size increase.

The histogram of TEM image of CuO NPs confirms that the particle sizes of NPs lie in the range (9-189 nm) (Fig IV.15), which is in good agreement with those calculated by the Scherrer-Debye formula from the XRD analysis, see (Table IV.13). The size distribution was obtained by measuring each particle diameter. The random orientation of particles allows for a statistical measure of the size distribution to be generated, and the mean value is calculated for each distribution.

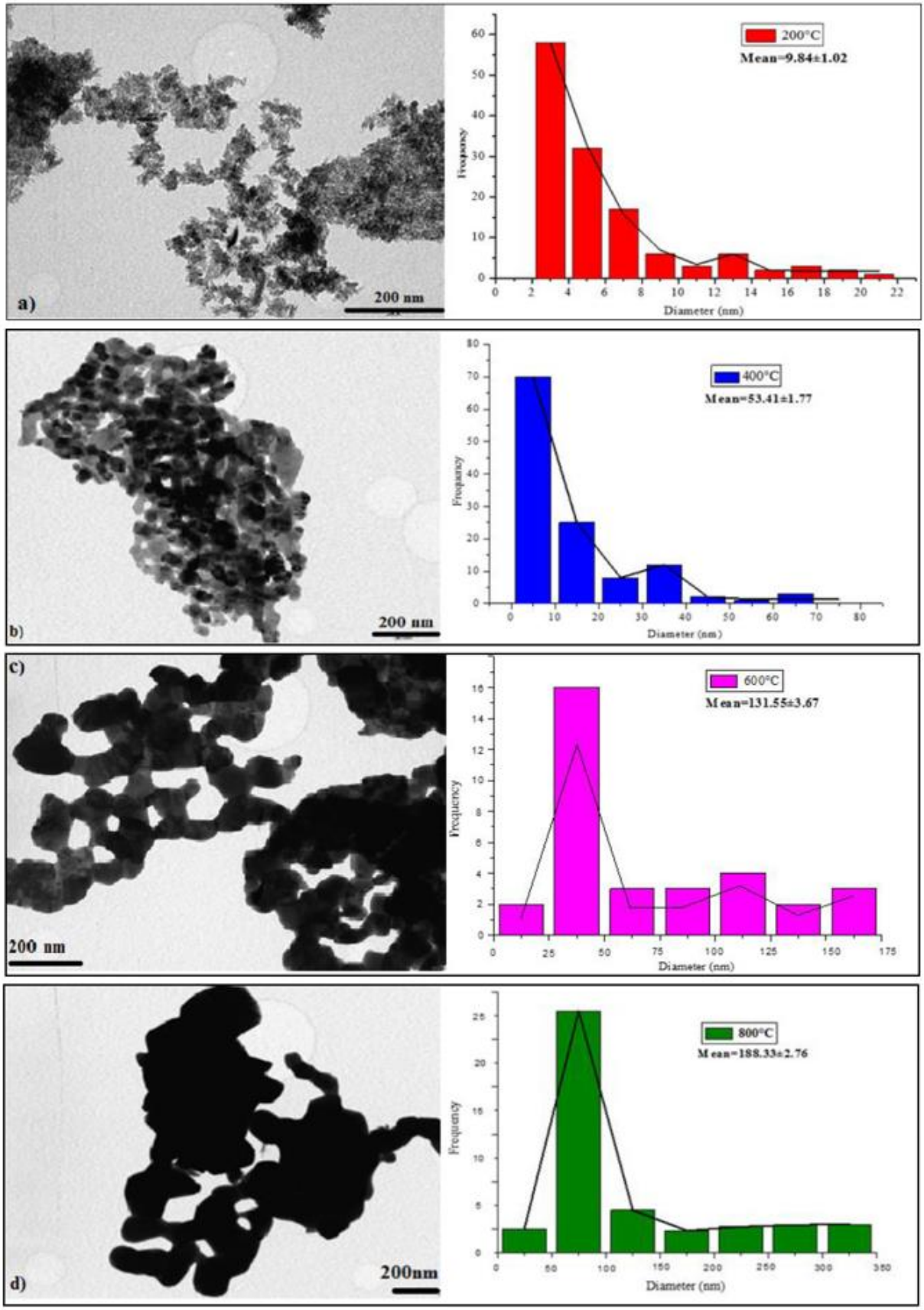

Figure IV.15: *TEM images and particle size distribution of CuO NPs annealed at a) 200°C, b) 400°C, c) 600°C and d) 800°C respectively.*

IV.3.4.3 Optical properties

The optical properties of CuO nanoparticle are determined from absorbance measurements from UV-Vis spectrophotometry in the range of 250-1000 nm. The optical absorption spectrum was used to characterize optical absorption properties of obtained CuO samples [168]. Figure IV.16 shows the UV-Vis absorption spectra of the samples annealed at different temperatures.

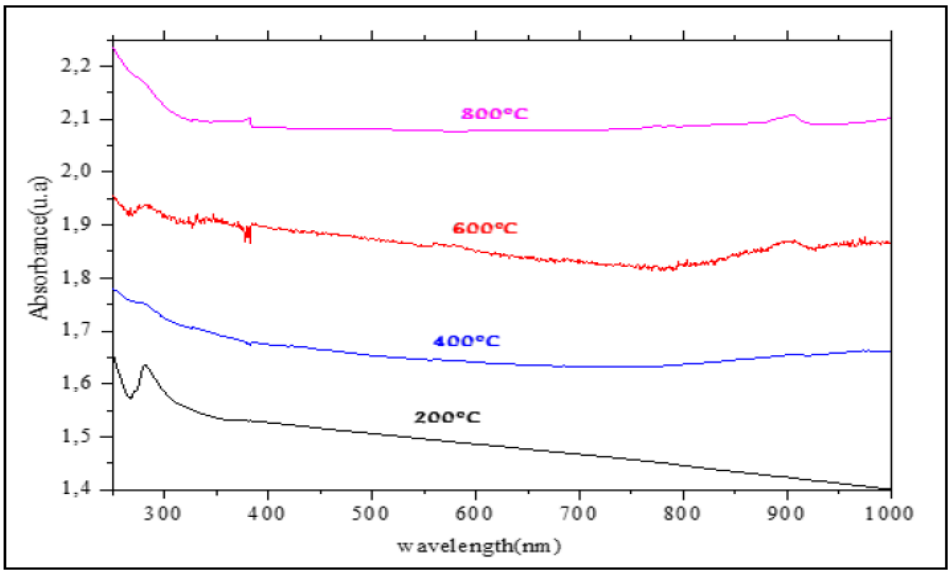

Figure IV.16: *Variation of the absorption coefficient of CuO nanoparticles as a function of wavelength.*

IV.3.4.3.1 Determination of the Band gap value

The band gap Eg, can be estimated from the absorption spectra by using the relation (Willardson and Beer):

$$(\alpha h\nu) = A(h\nu - E_g)^n \qquad \text{(IV.12)}$$

Where E_g is the gap energy of the material, ν is the frequency of the incident radiation, h is Planck's constant, α is the absorption coefficient in cm^{-1}. A, is a constant related to the material and the matrix element of the transition, and n is a coefficient depending on the nature of the transition (n = 1/2 for the direct allowed transition or 2 for an indirect transition).

The absorption coefficient is obtained using the relation

$$\alpha . d = \ln\left(\frac{1}{T}\right) \qquad \text{(IV.13)}$$

Where the transmittance T is calculated from the measured absorbance using the Beer-Lambert law,

$$B = -\log_{10} T \qquad \text{(IV.14)}$$

'd' represents the path length of the wave in centimeter (1cm) 13.

The linear relationship was obtained by plotting $(\alpha h\nu)^2$ against photon energy (hν). (Fig IV.17) represents $(\alpha h\nu)^2$ versus hν plots indicating that the absorption edge was due to a direct allowed transition. The line fit to the $(\alpha h\nu)^2$ versus hν plot is obtained by fitting a straight line to the linear portion of the curve. The value of optical band gap was determined by extrapolating the values of the coefficient of absorption α to zero. The values of the band were found to be 3.83 eV, 3.3 eV, 2.56 eV and 2.25 eV for the temperatures 200, 400, 600 and 800 °C respectively, as (Fig IV.17) shows.

(Fig IV.18) shows the variation of band gap and grain size with temperature, based on it, it is clear that the band gap decreases with the increase in temperature while the grain size increases. It has been observed that the band gap was maximum (3.83 eV) when the grain was minimum (9.84 nm) at 200 °C while it was minimum (2.25 eV) with a grain size of 205 nm at 800 °C.

Our results indicate a slight blue shift in the direct band edge as the particle size is reduced. Such a blue shift has also been reported in the literature for CuO quantum dots [169] where the blue shift has been attributed to the quantum confinement effects of nanoparticles [170].

The observed increase in the direct band gap values of CuO with the decrease in NNPs size is attributed to the quantum confinement effect [170].

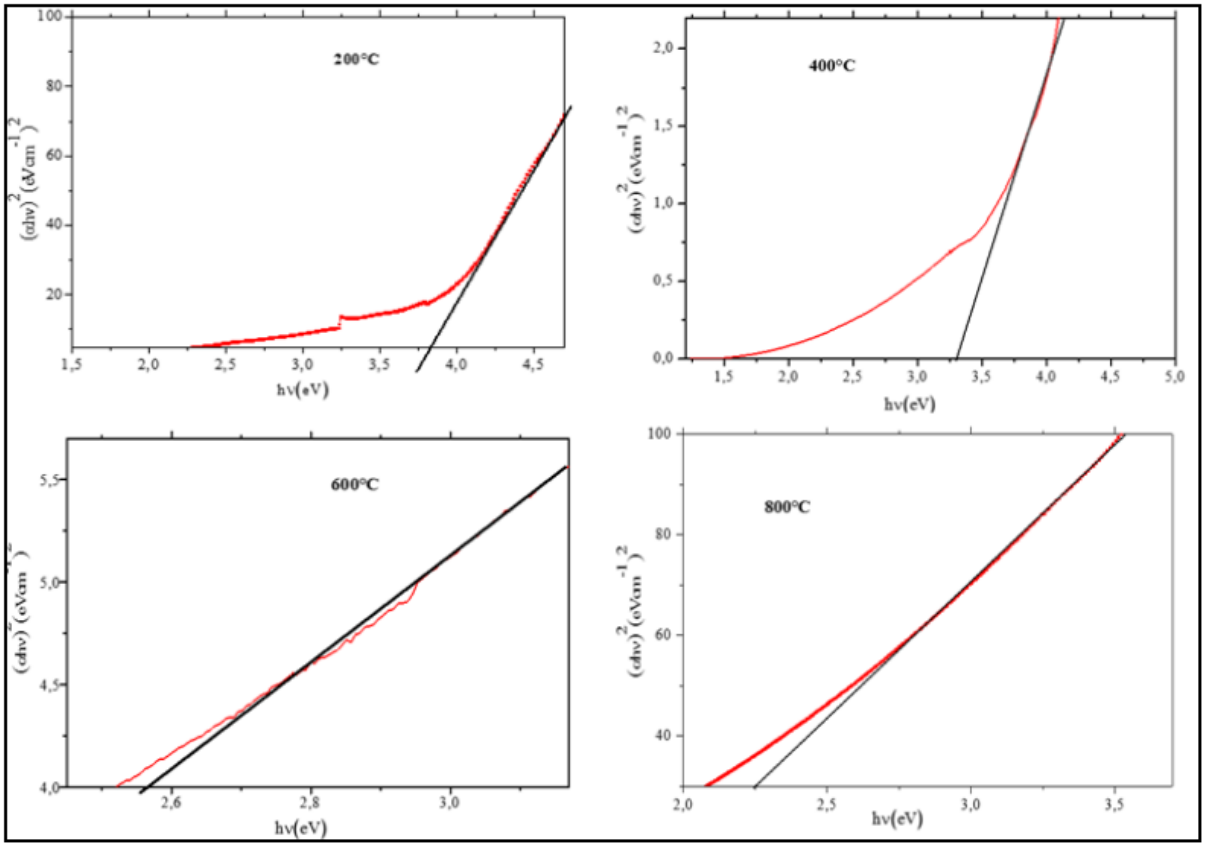

Figure IV.17: *The plot of αhυ2 vs photon energy for 200, 400, 600 and 800°C respectively.*

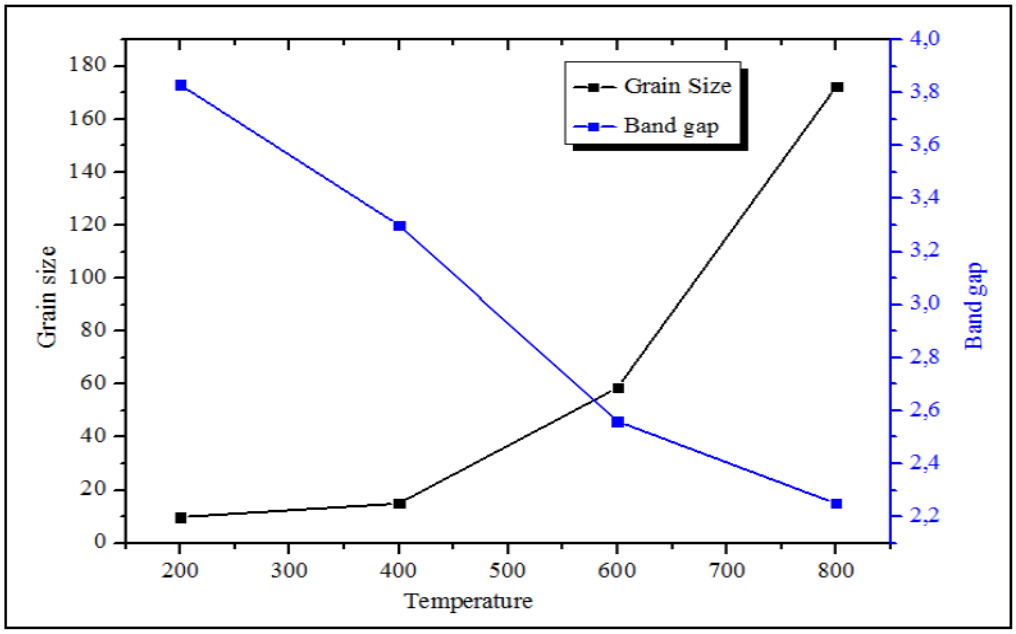

Figure IV.18: *The variation of band gap and grain size with temperature*

IV.3.4.4 Photocatalytic activity

For the investigation of the possible mechanism of adsorption between samples (CuO NPs) and MB, the kinetics of the photodegradation reaction was studied using the Lagergren pseudo-first order kinetics model [171]:

The amount of MB adsorbed at equilibrium was calculated by using the following equation (IV.15) and represented in (Fig IV.19-a):

$$q_t = \frac{(C_0 - C_t)}{m} V \qquad \text{(IV.15)}$$

Where C_0 and C_t are the initial and final concentration of MB in the solution (mg/L) respectively, qt(mg/g) is the amount of MB dye absorbed, V is the volume of MB dye in ml and m is the initial mass of CuO catalyst used (mg).

The pseudo-first-order and second order kinetics equations are given as follows:

$$\ln(q_e - q_t) = \ln(q_e) - \frac{k_1}{2.303} t \qquad \text{(IV.16)}$$

$$\frac{t}{q_t} = \frac{1}{k_2 q_e^2} + \frac{t}{q_e} \qquad \text{(IV.17)}$$

Where, q_e and q_t are the amount of the dye adsorbed on the adsorbent (mol/g) at equilibrium and time t, k_1 is the rate constant (min^{-1}) representing the pseudo-first-order kinetics, and k_2 is the adsorption of pseudo-second-order rate constant (mol/g.min). The pseudo-second-order adsorption kinetic plot is shown in (Fig IV.19-b), the correlation coefficient obtained R^2 is 0.99141 i.e., close to 1 which shows that it follows a pseudo-second-order reaction and which indicates that the equilibrium was established between MB dye and CuO NPs within 10 min.

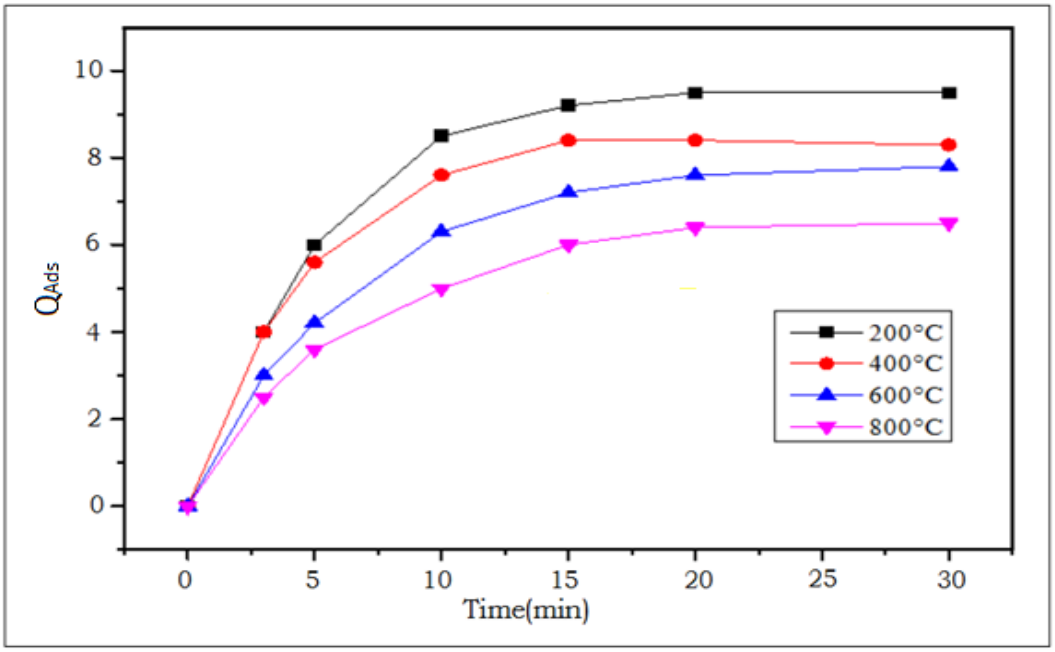

Figure IV.19-a: amount of MB adsorbed *on annealed CuO NPs.*

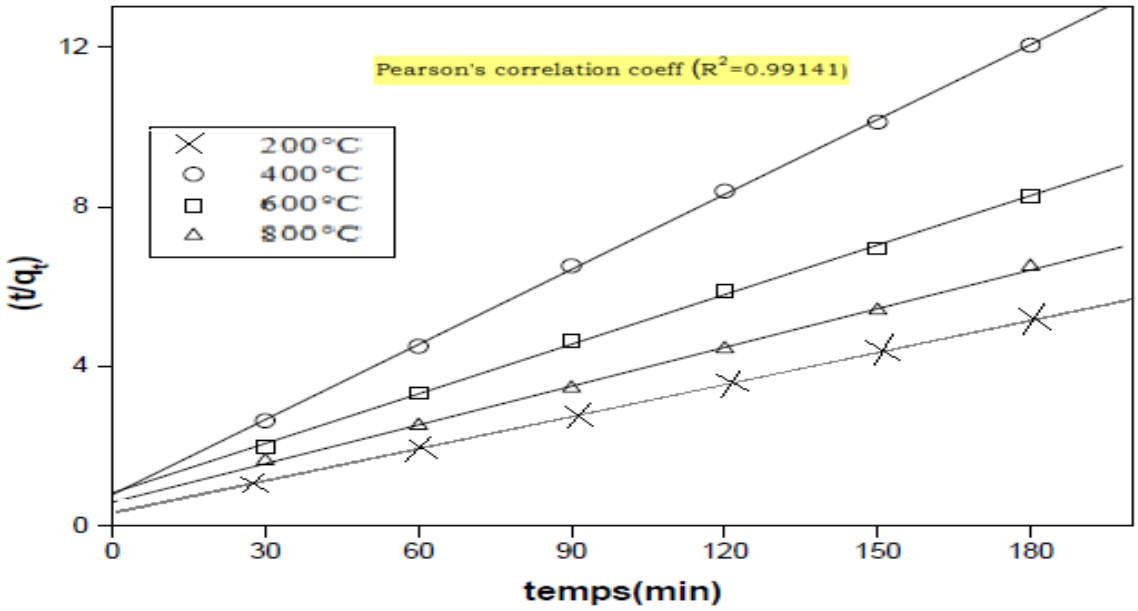

Figure IV.19-b: *Kinetics of methylene blue adsorption on annealed CuO NPs.*

Figure IV.20 shows the linear plots of C/C0 versus time for the photodegradation of MB on the CuO NPs samples annealed at 200°C, 400°C, 600°C and 800°C under visible light after 400 min illumination.

The absorption spectra of the samples were recorded by measuring the absorbance at 664 nm corresponding to the maximum absorption wavelength of MB with UV–visible absorption spectroscopy. The concentration of MB is proportional to the absorbance of MB according to the Beer–Lambert law, so the degradation efficiency of MB can be calculated by:

$$R(\%) = \frac{C_0 - C}{C_0} * 100 = \frac{A_0 - A}{A_0} * 100 \qquad \text{(IV.18)}$$

where A_0, A, and C_0, C are the absorbance and concentration of MB when the reaction time is 0 and *t*, respectively.

The results show that the photocatalytic activity of the samples depends on the temperature that means in another term, the NPs size. It was found that almost 60.75%, 68.3%, 75.89%, and 80.03% of methylene blue dye were degraded after 540 min UV illumination for samples annealed at 200, 400, 600, 800°C respectively. It is obvious that the photocatalytic activity of CuO samples annealed at higher temperature (800°C) have better photocatalytic activity, and this could be associated with their big particles size, so naturally exhibiting large specific surface sites which have been exposed for dye molecules, compared to those annealed at lower temperature, small particles size, smaller surface area.

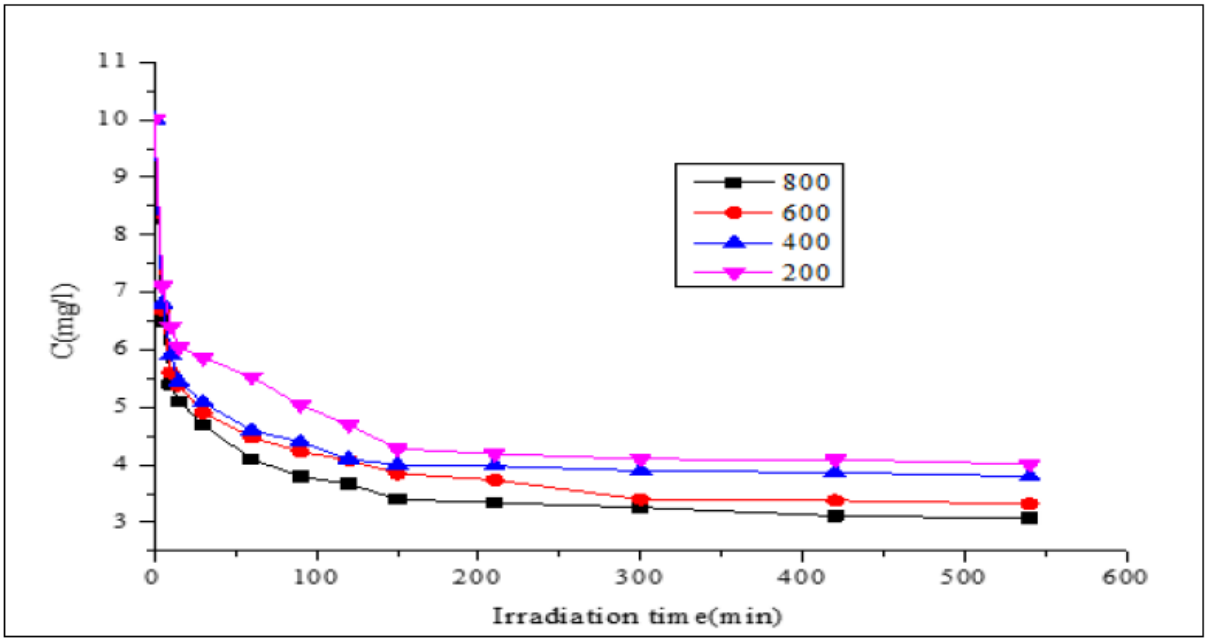

Figure IV.20: *Photodegradation of MB on CuO NPs annealed at 200, 400, 600 and 800°C*

IV.4 Conclusion

In the first part of this chapter, we studied the electronic, structural and optical properties of pure CuO using the generalized gradient approximation GGA and the mBJ approach. We've calculated the value of the gap energy of pure CuO, the band structure, the density of states, the dielectric function, the reflectivity, the refractive index, the absorption coefficient and the optical conductivity, the results which were obtained are in good agreement with the other theoretical and experimental results. In the second part, CuO NPs were synthesized by sol-gel combustion method. X-ray diffraction measurements revealed that the crystallite size, lattice parameters and crystallinity of CuO nanoparticles have enhanced with the elevation in annealing temperature.

TEM analysis indicated that the grain size evaluates proportionally with the evolution of temperature, which was well confirmed by XRD results. UV-Visible analysis indicated also that by reducing the NP's size the band gap raise to the higher values which was well confirmed in other way by Jin Zhong Zhang that when reducing in NP's size, the density of states becomes more quantized [172], (effect of reducing temperature, lack of excitement for the electron), so increasing in the band gap. On the other hand, the optical band gap of the CuO nanoparticles was found to be higher as compared to a bulk value indicating a blue shift of band gap, which has been attributed to the quantum confinement effect. Photocatalytic degradation of methylene blue was carried out the as-synthetized nanoparticles at four different annealing temperatures under visible light irradiation. The results have shown that the photocatalytic activity of the samples depended on the annealing temperature that they endured, so in our experiment, the photodegradation efficiency was promoted by increasing the annealing temperature so by augmenting the CuO NPs size.

Chapter V

Electrochemical study on CuO/Pt-TiO2 composite material

V.1 Introduction

TiO2 has been one of the most extensively studied metal oxides because of its remarkable optical and electrical properties and its potential utilization as low cost material for Photocatalysis [177,178], photovoltaic cells [179], dye sensitized solar cells (DSSC) [180], gas sensors [181] and energy storage devices [182]. Due to the wide band-gap (Eg = 3.2 eV), it is believed that TiO2 behaves as a very attractive material for the development of optoelectronic devices, such as light emitting diodes [44], and photodetectors. However, this advantage could limits the application of visible light [183], since it can only show photocatalytic activity under UV light

irradiation ($\lambda < 387.5$ nm) that accounts for only a small portion of solar energy (approximately 5%), in contrast to visible light for a major part of solar energy (approximately 45%). Such fundamental limitation is occurring also for the electrochemical due to the limited conductivity [8], which is also due to the wide energy gaps of TiO2 phases, that makes the material rather ineffective for most potential applications. Therefore, many researches were done to find optimal solutions for this limitation, including reduction of the energy gaps by doping with both transition metal [185-187] and nonmetal dopants [188,189]. Transition metals exhibits a unique d electronic configuration and spectral characteristics, which make the transition metal doping, the one of the most effective approaches to extend the absorption edge of TiO2 to visible light region. Which either inserts a new band into the original band gap or modifies the conduction (CB) or valence band (VB), improving the photocatalytic activity of TiO_2 to some degree [190-192]. Transition metals doping methods have become hotspots of the research on TiO2 compound since that introducing these impurities could generate donor or acceptor states in the band gap and thereby increase the concentration of charge carriers. Consequently, numerous research efforts concerning the doping or modification of TiO2 material have been made to eventually improving its properties. Although, copper oxide Cu(II)O, as was discussed previously, a semiconductor with a narrow band gap of 1.7 eV and has long been known for its catalytic capabilities and have promising applications in many fields including catalyst, lithium ion batteries and gas sensor [193,194], was reported alone, having a specific capacitance less than 100 $F.g^{-1}$ [195].

It is worth mentioning that improving electrical conductivity of electrode materials and advancing its surface material would help to enhance its electrochemical properties. So far, TiO_2 nanotubes TNTs based composite materials have been used widely for electrochemical capacitor applications [9]. Therefore, TNTs conductivity substantial improvement is needed for supercapacitor electrode materials because of its limited conductivity [196]. For instance, Yan & al found that noble metals like gold, silver, and platinum, exhibit high conductivity and can facilitate effective transport of electrons that arise from the oxidation/reduction of pseudocapacitors to the current collectors [197].

Due to the unique advantages of Pt, these metals facilitate and orient numerous chemical reactions by their mere presence or their high catalytic ability and power. The presence of the Pt nanostructures as catalysts entails having major possible active surface, which can deliver a maximum possible number of catalytically active sites [198], which makes it possible to improve

the conductivity of electrons and ions and consequently gives a higher reversible capacitance at a high rate. Although their scarcity and expensiveness, it has proved that, their integration with other sustainable and inexpensive materials makes it possible to optimize their properties and minimize their consumption [197]. In addition, Platinum is characterized by its chemical stability against oxidation, its resistance to corrosion and its high durability and lifespan, which allows the electrode to operate more efficiently over a longer period [199]. Therefore, combining these interesting properties by elaborating CuO/Pt-TiO_2 (CPTNTs) composite, results in durable electrodes with an appreciative electrochemical performance, cyclic stability as well as lower value of charge transfer resistance. At last, to give a theoretical and more rational aspect to this work, density functional theory-DFT-was used to investigate the electronic properties for the TiO_2 and (Cu, Pt) co-doped TiO_2.

In this chapter, detailed results and discussion related to the characterization of CPTNTs composite material are presented to emphasize the possibility to fabricate Pt-TiO2 Nanotubes (PTNTs) as a current collector, the introducing of CuO nanoparticles into the system will be also discussed to explore then its electrochemical and conducting properties. Additionally, first-principles calculations were employed to investigate in detail the structural, electronic, optical and transport properties of Cu and (Cu, Pt) co-doped TiO2, to understand further its electrochemical behaviors. These results obtained throughout this study were able to demonstrate that this new and firstly reported nanocomposite is a noticeable candidate for high performance supercapacitors.

V.2 Synthesis and elaboration of CuO/Pt-TiO2 (CPTNTs) material

V.2.1 Preparation and surface treatment of Ti substrates

Titanium foil was primarily cut into small rectangular pieces of 2 x 1 cm^2, as shown in Fig. V.1, and cleaned via ultrasonication in ethanol and acetone then rinsed with DI water, and finally dried with a hair dryer.

V.2.2 Anodic oxidation (growth of TiO2 NTs):

The electrochemical anodization was conducted in a two-electrode system using a DC power supply (K. Source Meter 2400, Keithley Instruments), with the Ti substrate as working electrode and steel foil as the counter electrode, under a constant 60 V anodic potential for an anodization time of 2 h at room temperature (25 °C). The electrolyte consisted of (35; 55; 10 wt. %) of ethylene glycol, glycerol and H_2O respectively with 0.4 M of NH_4F.

In order to convert the amorphous phase to the crystalline phase (anatase phase), the samples were heat-treated for 60 min at 300 °C in air.

V.2.3 Platinum sputtering on TiO2 NTs

Platinum nanoparticles were loaded on TiO2 NTs by DC magnetron sputtering (DC-MS) deposition method.

The deposition was performed in a sputter coater (Sputter coater Emitech K575X) under an argon work pressure of 2.0 Pa at room temperature, with a discharge current of 40 mA for a time rate of 30 s. The TiO2 NTs surface was located at a distance of 40 mm from the Pt target. The control of deposition rate was performed in situ by the optional 10454 consisting of a controller and quartz crystal oscillator built into the Q150T device system.

Figure V.1: *K575X turbo Sputter Coater used for Pt NPs deposition*

V.2.4 Electrochemical deposition of Cu NPs and thermal oxidation

In order to electrodeposit the Cu NPs into the as obtained Pt-TNTs oxide electrode, an electrochemical deposition was done in a conventional two-electrode system in 0.1 M CuSO4 and 3 M lactic acid aqueous solution. The concentrated lactic acid plays a role for the copper ions stabilization [67]. Then, the pH of the solution was adjusted with NaOH. A pulsed galvanostatic mode was rationally chosen, by applying 50 mA/cm^2 within 30 cycles to get a uniform deposition. In order to investigate the effect of oxidation of copper, thermal oxidation was done

by annealing sample at 400°C in 90 min to oxidize then copper into copper oxide and to get the CuO/Pt-TiO2 composite material.

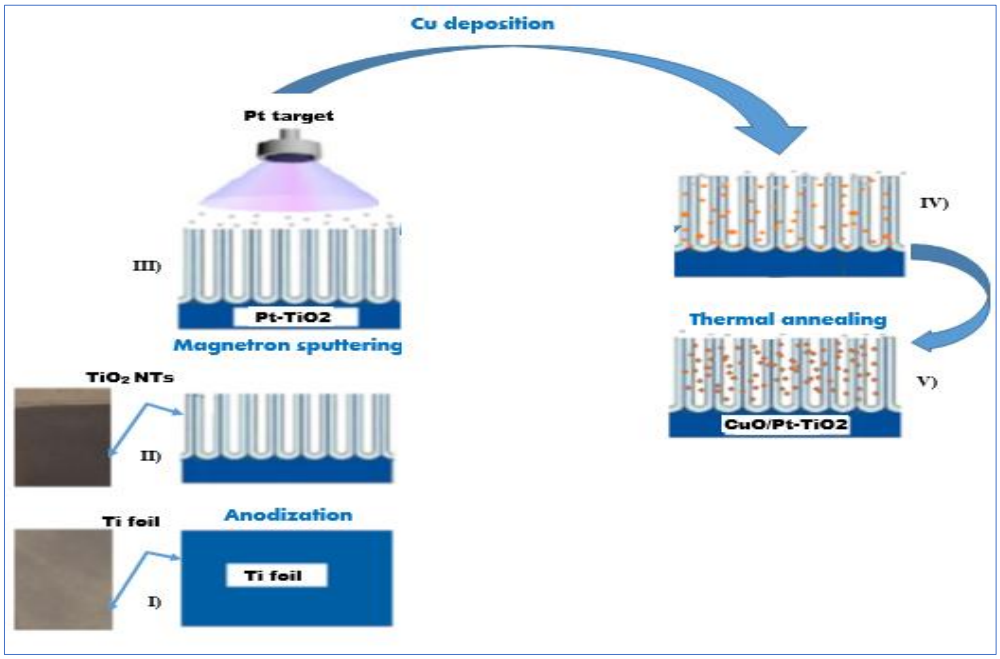

Figure V.2: *Schematic representation of synthesis of Cu/Pt-TiO2 NTs composite material (CPTNTs).*

V.3 Physicochemical characterization of (CPTNTs) electrode material:

The surface morphology and microstructure of the as synthetized materials were determined using a high-resolution scanning electron microscope (SEM, Ultra Plus, ZEISS, Germany), equipped with an energy dispersive X-ray spectroscopy package (INCA, Oxford, UK) to identify and quantify the nature of the chemical elements present in the sample. X-ray diffraction measurements (XRD, X'Pert Pro diffractometer PANalytical, Holland) as well as Raman scattering (Raman microscope, Senterra, Bruker, Germany) were carried out to determine the crystalline structure and phase behavior of the material.

V.3.1 X-ray diffraction analysis

XRD patterns of the TNTs and CPTNTs are shown in Fig.V.3 a, the anatase phase of TiO2 appears to be present in both of the samples, according to (JCPDF PDF 075-2550), which are assigned as A. The peaks, which are centered at 2θ values of 40.05, 52.87, and 70.05, comes from Ti metal substrates, and they are presents in each of the samples. The CPTNTs exhibits few additional peaks located at 35.57, 38.32, 39.06 belonging to (−111) (111) and (200) planes which

correspond to the CuO (JCPDS PDF 089-5897), and the peak appearing at 35.12 *hkl* (311) is that of platinum (JCPDS no 070-2057).

V.3.2 Laser Raman spectroscopy

The Raman spectra (Fig. V.3b) exhibits five characteristic peaks, the intense one that is located at 151.5 cm^{-1} is assigned as Eg peak along with 202.8 and 614.24 cm^{-1} are as low intense Eg, one B1g peak appears at 383.3 cm^{-1} and the (A1g + B1g) peak appear at about 514.51 cm^{-1} which corresponds to the anatase phase. The symmetric stretching, the anti-symmetric bending and the symmetric bending vibrations of O–Ti–O are the origins of the Eg, A1g and B1g active modes, respectively [204].

CuO (II) oxide belongs to the C_{2h}^{6} $(C2/c)$ space group ascribed to the structure of the tenorite, with two molecules in the primitive cell. As reported before, by Chrzanowski and Irwin [205], there are 12 vibrational modes at the zone center, which are scattered in the network as follows: $\Gamma = 4Au + 5Bu + Ag + 2Bg$, the Ag + 2Bg are the only Raman active modes.

It can be seen from the Raman spectrum for sample CuO/ Pt-TiO2 composite represented in Fig. V.3 b, that the 3 peaks which corresponds to 280.6, 329.73 and 620.84 are assigned to Ag and two Bg vibrational modes, these wavenumbers are almost close to those reported in the literature (288, 330 and 621 cm − 1) by Xu et al. [206].

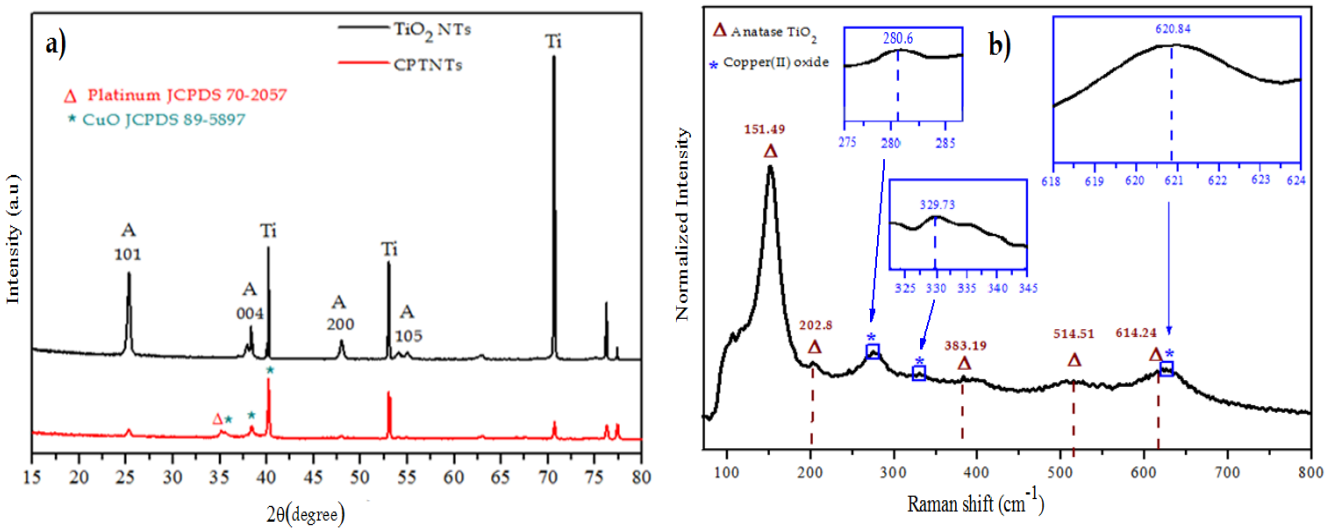

Figure V.3: *(a) XRD spectra of a TNTs and CPTNTs composite, (b) Raman spectrum of CPTNTs.*

V.3.3 SEM & compositional study (EDX)

The SEM images reveals that the nanotubes pores opening are almost circular in shape as observed from the top and cross section view of TNTs, Fig. V.4 (a-c) and they are vertically

oriented from the surface of Ti metal substrate with tubular channels. The average size of the NTs is 60-70 nm in width with around 2.7 µm in uniform length. Elemental composition of these nanotubes show the presence of Ti and O species along as shown in Fig. V.4 d, also the weak appearance of F peak is maybe due to the presence of F^- ion from NH4F in the anodization electrolyte. Since their tubular channels offer a rigid support structure to permit a feasible loading of various designated electroactive materials, few amount of Pt nanoparticles were loaded uniformly in TiO2-NTs, constituting a hyperfine layer over the entire TiO2-NTs network. On the other hand, this layer contributed to the growth of CuO NPs on its surface during the electrochemical deposition.

The CuO nanoparticles deposited onto the inner surface and interface of the Pt-sputtered TNTs are shown in Fig. V.4 (e-h). Figure V.4 e-g, represents the top view as well as the corresponding cross-section of SEM images, it should be mentioned, that the CuO nanoparticles are dispersed uniformly all along the material lattice, within uniform shapes, suggesting the effectiveness of the preparation method of this composite. EDS results, presented in Fig. V.4 h, confirms the presence and the distribution of copper, platinum, titanium and oxygens atoms that integrate the material.

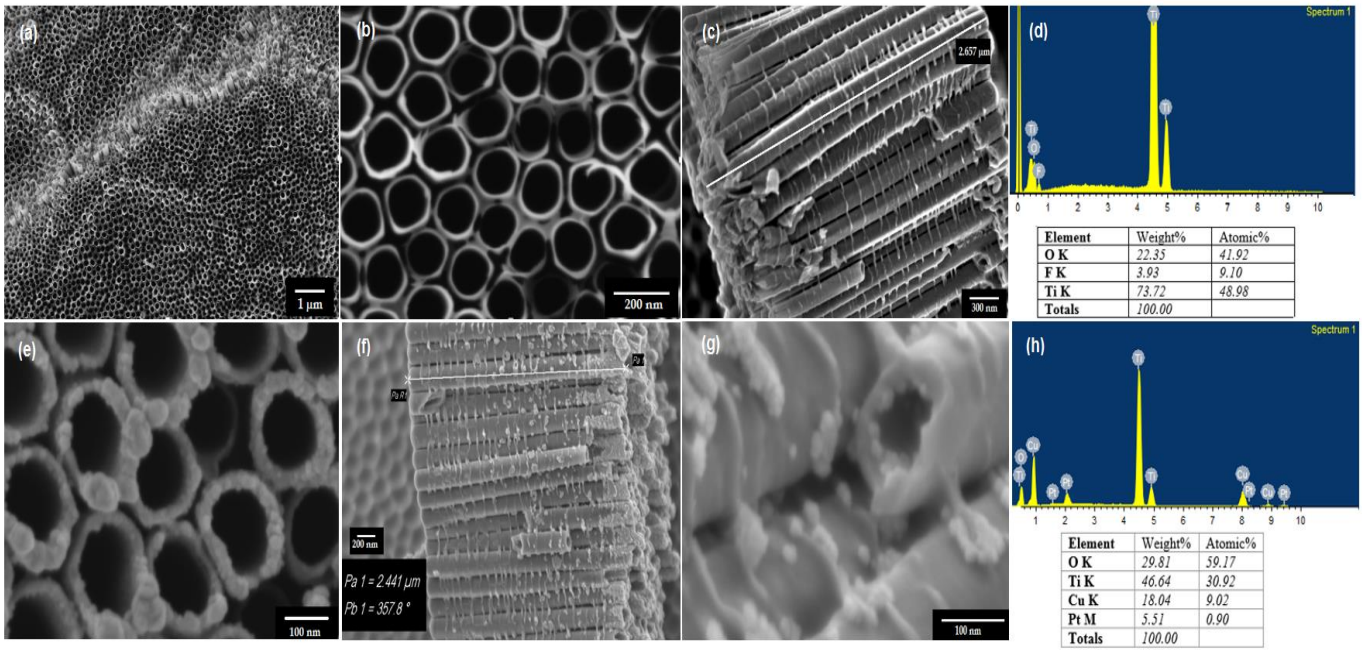

Figure V.4: *(a-d) SEM images of TiO2 NTs (TNTs) and (e-h) CuO/Pt-TiO2 (CPTNTs) composite.*

V.3.4 TEM transmission electron Microscopy

TEM images shown in Fig. V.5 a, b confirms the alignment of the TiO2 NTs and could confirms the inner shape of the nanotubular structure of these nanotubes, which is in accordance with the above SEM Results. We could clearly observe the uniformly distributed CuO nanoparticles with a small average diameter of 30 nm on the inner surface of the Pt-TNs, as depicted in Fig V.5. The inner diameter of the CuO coated on Pt/TiO2 nanotubes decreased compared to the pristine TiO2 nanotubes owing to the uniform deposition of the CuO on the surface of the TiO2 nanotubes. TEM and SEM imagery results, both agrees with the as-found results see Fig. V.4 (e-h).

V.3.5 XPS spectroscopy

Results of X-ray photoelectron spectroscopy (XPS) are shown in Fig. V.5. The typical peaks of Ti 2p, O1s, Cu 2p, and Pt 4f in the survey spectrum can be, clearly seen in Fig. V.6 a.

The peaks located at ca. 458.5 and 464.2 eV corresponds to the titanium peaks of Ti 2p3/2 and 2p1/2, respectively (Fig. V.6 b), which confirms the presence of Ti^{4+} ions in the lattice [207]. The other peak O1s located at 532 eV represents the lattice O^{2-}anions bonding to the metal cations in the Ti–O bond [208, 209].

The high-resolution Cu2p spectra are shown in Fig. V.6 c. The peak at 933.2 eV is attributed to Cu2p3/2, whereas the peak at 953.61 eV is corresponding to Cu2p1/2, indicating the existence of CuO nanoparticles with the +2 oxidation state of Cu [210]. In addition, satellite peaks of Cu2p3/2 and Cu2p1/2 were observed as peaks (S1) and (S2), respectively, characteristic of a partially filled d-orbital ($3d^9$ in the case of Cu^{2+}) [211].

Moreover, in Fig V.6 d, the binding energies located at 70.6 and 74.0 eV are the peaks of Pt0 4f7/2 and 4f5/2, as well the peaks located at 71.5 and 75.0 eV are attributable to the bond of Pt-O [184].

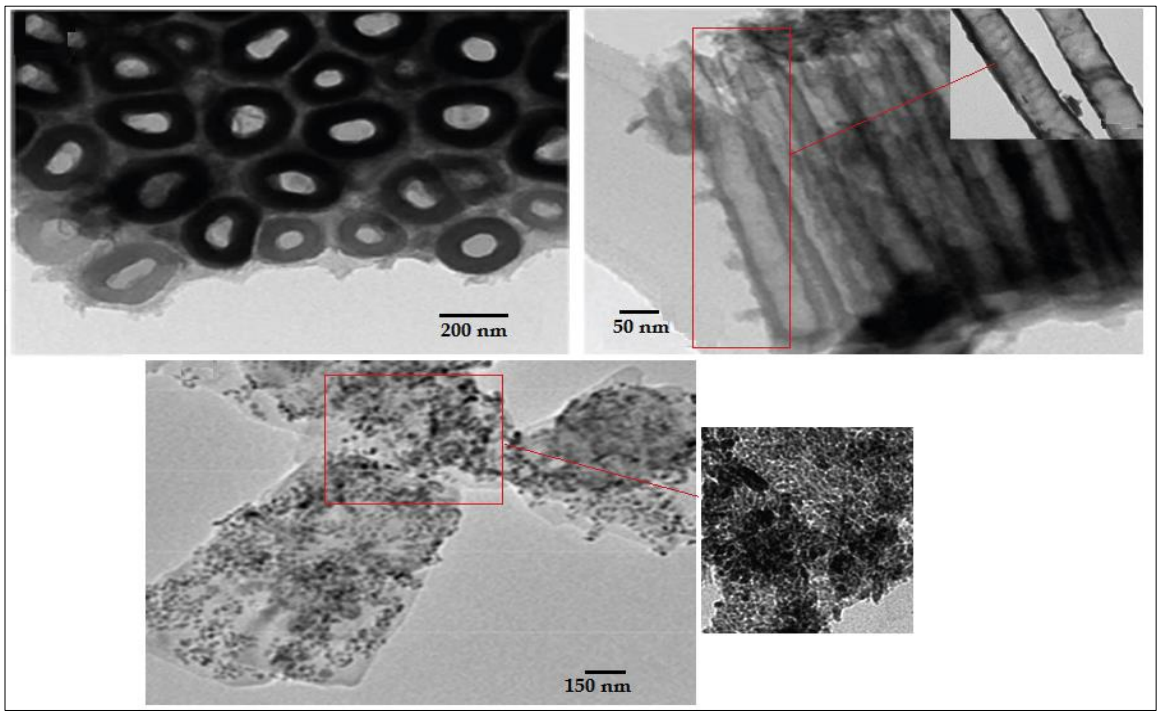

Figure V.5: *Typical TEM images of the TNTs: top view and cross section (a), TEM images of the CPTNTs electrode (b).*

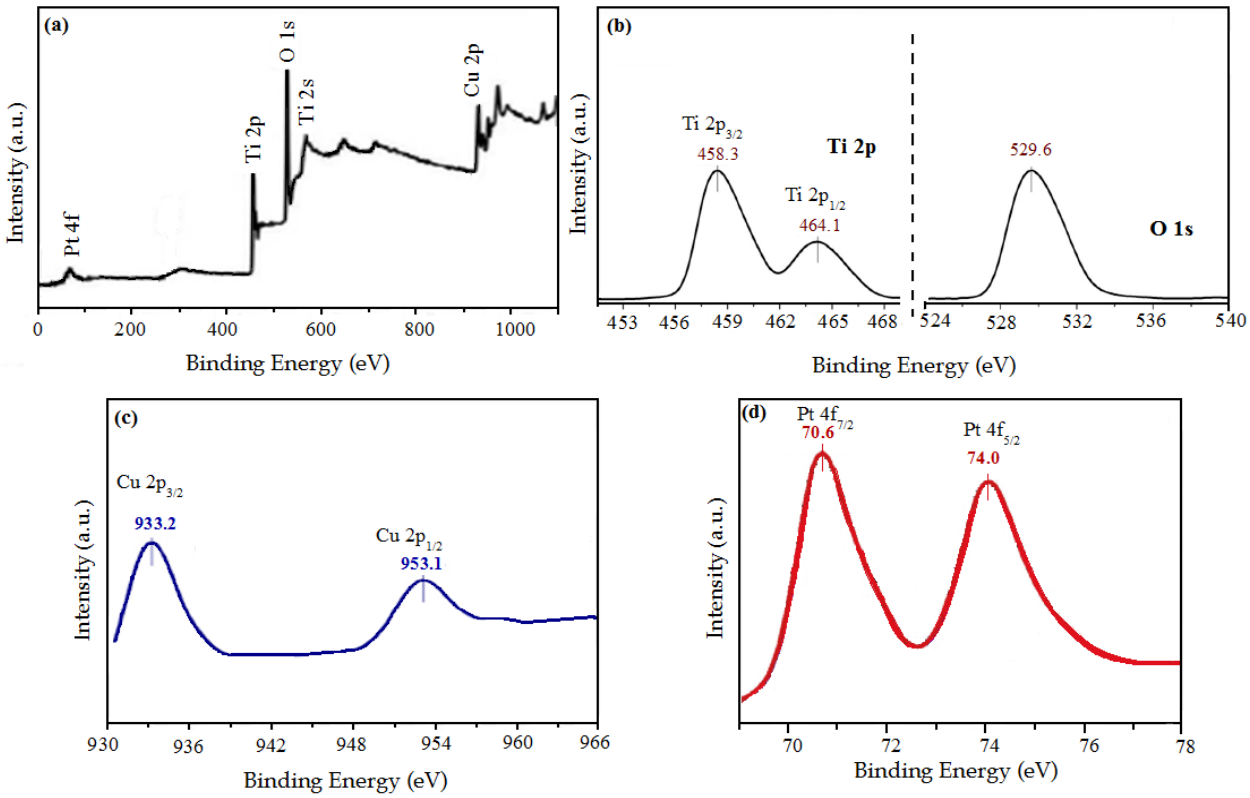

Figure V.6: *General XPS spectra for the CPTNTs electrode (a), High-resolution XPS spectrum of Ti 2p and O 1s region (b); of Cu 2p region (c); of Pt 4f 5/2 and Pt 4f 7/2 core-level lines (d).*

V.4 Electrochemical measurements

Electrochemical impedance spectroscopy (EIS) and cyclic voltammetry (CV) measurements were performed with an electrochemical workstation (ZAHNER IM6e, Kronach, Germany), galvanostatic charge–discharge measurements with the Source Meter 2400 (Keithley). The electrochemical performance of the different electrodes was characterized in 1 M Na2SO4 aqueous electrolyte at room temperature using a three-electrode setup with a Pt mesh as counter and an Ag/AgCl as a reference electrode.

The specific capacitance C_{sp} (F.g^{-1}) was calculated from CV curves using Eq. (V.1) [200, 201]:

$$C_{sp} = \frac{1}{m\nu(V_c - V_a)} \int_{Va}^{Vc} I(V)dV \qquad \text{(V.1)}$$

where C_{sp} is specific capacitance (F/g), m is active mass of materials, ν is scan rate (mV/s), I is the response current (mA), $V_c - V_a$ (V) is the potential range window. Further, the capacitance measurements were carried out from the galvanostatic charge and Eq. (V.2) was used to obtain specific capacitance values from galvanostatic charge discharge curves:

$$C_{sp} = \frac{I*t}{m*\Delta V} \quad \text{(V.2)}$$

where *I* represents the charge–discharge current, *t* the discharge time; ΔV is the corresponding potential window and *m* is the active mass of CuO/Pt-TiO2 composite electrode [19].

To evaluate more the supercapacitive behavior of the material, energy, and power density (*P*; W Kg^{-1}) were calculated according to the following equations [202, 203]:

$$E = \frac{1}{7.2} C_{sp} * V^2 \quad \text{(V.3)}$$

$$P = 3600 * \frac{E}{\Delta t} \quad \text{(V.4)}$$

V.4.1 Cyclic voltammetry (CV)

Figure V.7 a shows the cyclic voltammetry curves for the pristine TNTs at different scan rates, in the potential window ranging from -0.4 to 1.2 V, a redox reaction peaks located at -0.06 V and 0.17 V, which is attributed to the transition between TiO_2 and Ti(OH)3 by the reaction:

$TiO_2 + 2H_2O + e^- \leftrightarrow Ti(OH)3 + OH^-$ [45].

Figure V.7 b compares the CV responses for TiO2- NTs and Pt-TiO2 NTs electrode at a scan rate of 100 mVs^{-1}. One can clearly see that the CV curve of Pt-TNTs electrode has a considerably larger integrated area as well as higher current response than that of TNTs electrode, which can be attributed to the higher electrical conductivity, present in noble metals such as platinum that facilitates the transport of charge carriers [197].

In Fig. V.7 c, it is shown, that the CV curves for Pt-TiO2 electrode recorded at different scan rates exhibit an unchanged quasi-rectangular shape from 5 to 100 mV/s, indicating excellent capacitive behavior and high rate capability of this electrode. Figure V.7 d shows the calculated specific capacitance of the Pt-TNTs based on the CV curves. The specific capacitance of the Pt-

TNTs electrode as calculated is found to be 18.94 mF cm−2 at a scan rate of 5 $mV.s^{-1}$, which is about 13 times more than pristine TNTs electrode (1.65 $mF.cm^{-2}$).

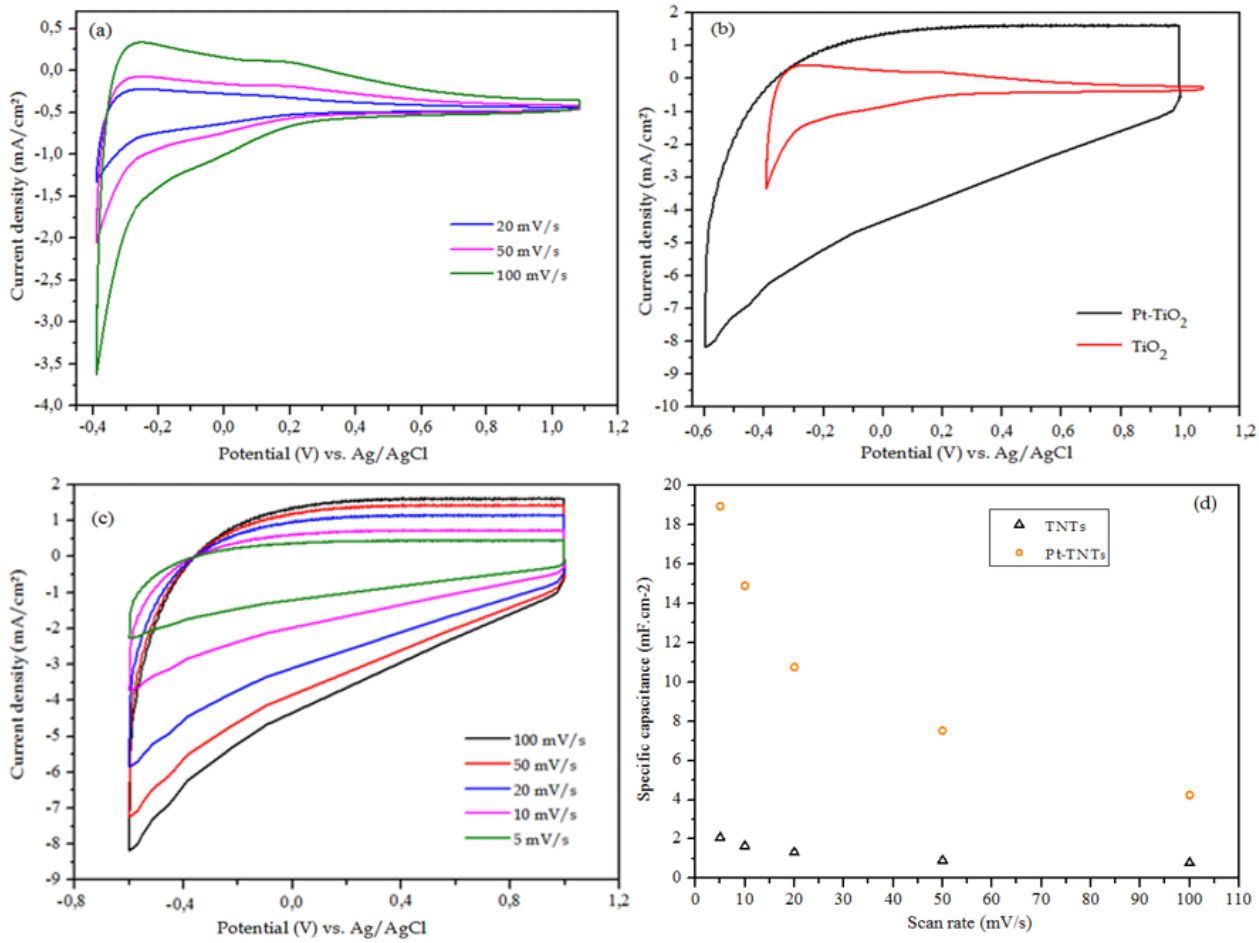

Figure V.7: *CV curves of TiO2-NTs at different scan rate* ***a)****, Pt-TiO2-NTs at 100 mV s−1* ***b)****, CV curves of Pt-TNTs at various scan rate* ***c)****, Specific capacitance of TiO2-NTs and Pt-TiO2-NTs at various scan rates* ***d).***

CV curves of the CPTNTs (CuO/Pt-TiO2-NTs) composite measured at various scan rate in the potential range -0.4 to 0.8 V is provided in (Fig. V.8 a), they are consisting of a pair of strong redox peaks indicating that the capacitance characteristics of this material are mainly governed by faradaic redox reactions, which can be described as follows:

$$2CuO + Na^{+} + e^{-} \leftrightarrow Cu2OONa \qquad (V.5)$$

The pseudo-capacitance behavior can be explained by these redox transition between Cu(I) and Cu(II) species and vice versa [46].

V.4.2 Galvanostatic charge-discharge (GCD)

GCD measurements were carried out in 1 M Na2SO4 at different current densities ranging from 0.5 to 5 A g^{-1}, to understand the rate capability of the obtained CPTNTs composite.

As shown in Fig. V.8 b, GCD curves present similar charge-discharge procedure at different current densities indicating its electrochemical reversibility [212].

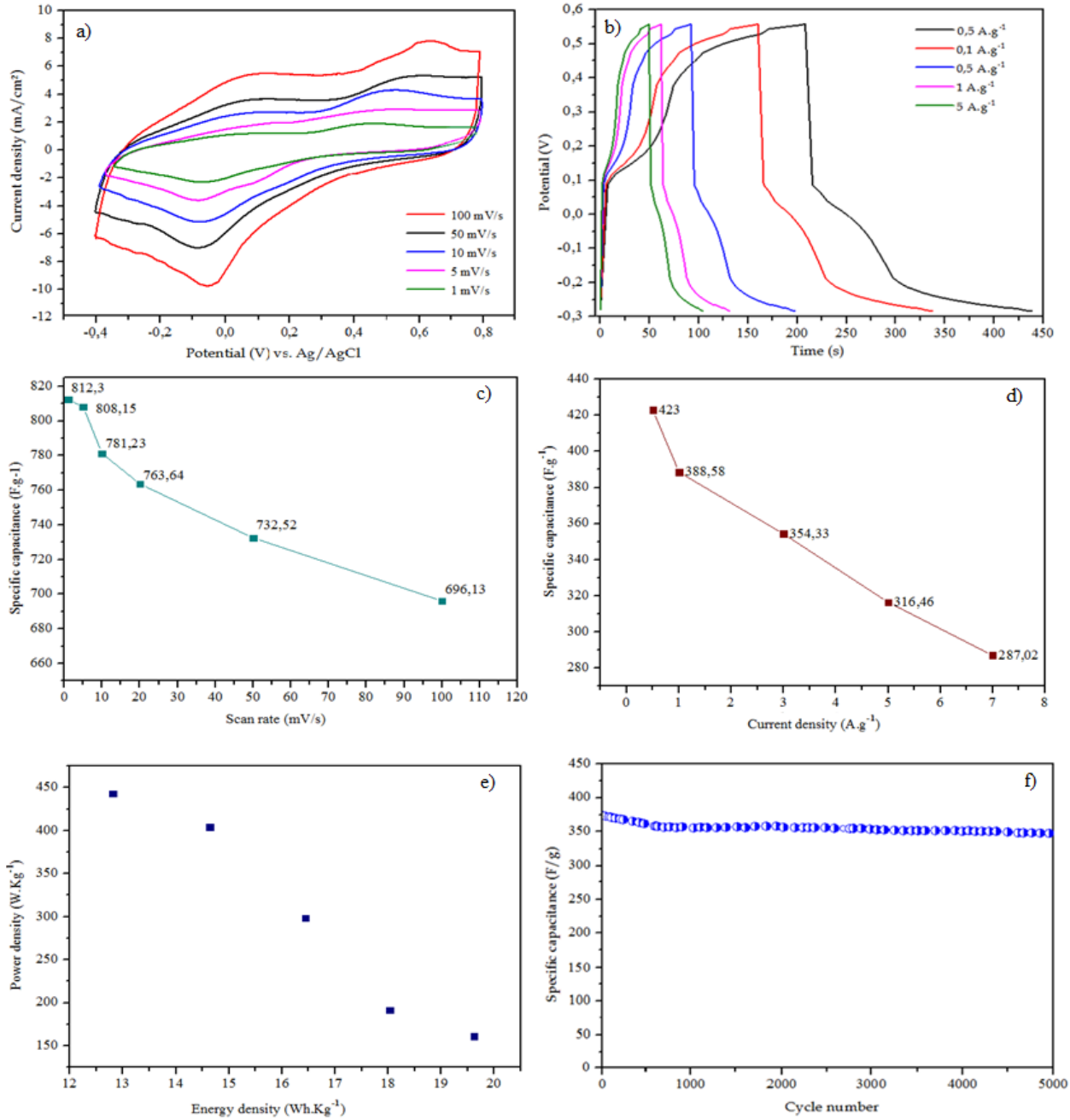

Figure V.8: *(a) CV curves of CPTNTs at 100mV.s^{-1}, (b) GCD curves of CPTNTs, (c-d) Specific capacitance of CPTNTs at various current densities and scan rates, (e-f) Ragone plot and cyclic stability of CPTNTs.*

Moreover, the relationship between voltage and charge/ discharge time is not linear and it can be seen at the same time that, the charge and discharge profiles of the electrode are slightly curved, confirming the existence of a pseudocapacitive charge storing mechanism, which is in a good accordance with the results of cyclic voltammogram test.

During the charge–discharge process, a reversible redox reaction has occurred [the redox reactions given in formula above (Eq. V.5)]; and during the charge procedure, the Cu^{+} can be oxidized to Cu^{2+}, while during discharge procedure, the Cu^{2+} will be reduced to Cu^{+}.

Figure V.8 c, d shows the corresponding specific capacitance values extracted from cyclic voltammetry and charge discharge curves respectively. As shown in Fig. V.8 c, d, the specific capacitance decreases with the increase in discharge current density. The reduction in specific capacitance of active materials at high current densities is mainly attributed to the poor utilization of materials, Fig. V.8 d.

Figure V.8 e show the Ragone plot of CPTNTs material, the energy and power density values elicited from galvanostatic charge–discharge curves, calculated using formulas in Eqs. (V.3) and (V.4). The maximum specific energy obtained for the CPTNTs electrode is 18.03 Wh/kg and power of 192.33 W/kg when the current is 0.5 $A.g^{-1}$, and it is also interesting to note that the specific energy remains at 12.81Wh/kg at a specific power of 445 W/kg after increasing the current density to 7 A/g.

As shown in Fig. V.8 f, 93% of the initial specific capacitance is retained after 5000 cycles, which reveals that CPTNTs electrode has good cyclic stability. Furthermore, specific capacitance and cyclic stability are found to be the best among the previously published transition metal related supercapacitor materials. A comparison is made with the current material and those reported in literatures, as shown in Supplementary Table 1; see Supporting Information for more details.

V.4.3 Electrochemical impedance spectroscopy (EIS)

Figure V.9 b shows the Nyquist plots of electrochemical impedance spectra of the Pt-sputtered TiO2- NTs and CuO/Pt TiO2 composite material (CPTNTs).

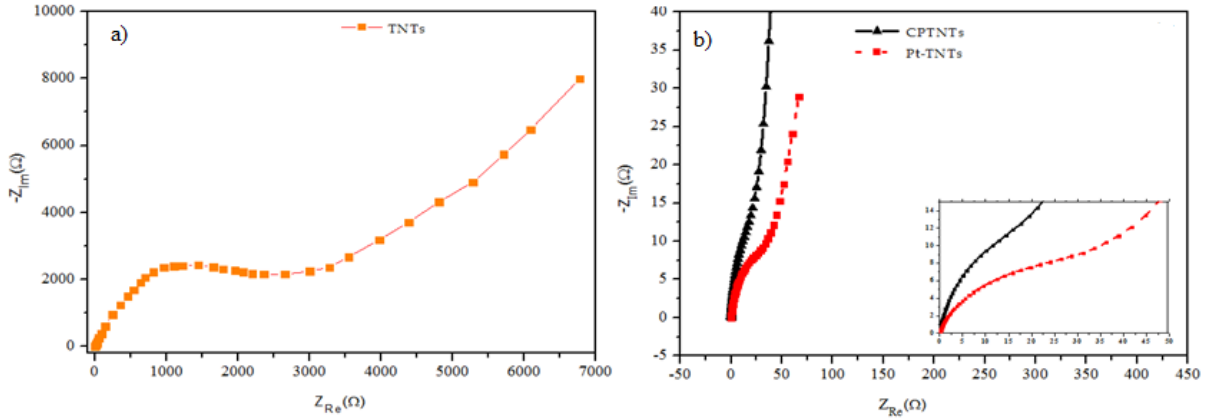

Figure V.9: *EIS spectra of pristine TiO2-NTs (a) and Pt-TiO2-NTs and CPTNTs (b).*

As can be seen from the plot is that the semicircle of the CPTNTs is smaller than the Pt-TiO2, which is smaller than the pristine TiO2- NTs presented in Fig. V.9 a. From this, we can determine an approximate value of the charge–transfer resistance (Rct) at the electrode/electrolyte interface, this electrochemical charge transfer resistance Rct is determined by measuring the diameter of the semicircles starting from the Nyquist plots. These values are found to be (13.72 Ω) for CPTNTs (31.83 Ω) for Pt-TiO2 and (2.65 KΩ) for TiO2-NTs, which leads to enhanced charge transfer ability of CPTNTs material and proves its benefit for electronic/ionic transport that can lead to an improvement in the his electrochemical performances. In addition, this is further confirmed by the results gotten from the first principles calculations.

V.5 Ab initio investigation on Cu and (Cu, Pt) codoped TiO2

V.5.1 First principle calculations

First-principles calculations were carried out using the Modified Becke and Johnson (mBJ-GGA) generalized gradient approximation in order to investigate electronic properties, based on density functional theory (DFT) as implemented in WIEN2k package simulating code [213]. Tetragonal structure of anatase TiO2 has been obtained by positioning Ti1, Ti2, O1, O2, O3 and O4 atoms at (0, 0, 0) (0.5, 0.5, 0.5) (0, 0.5, 0.5) (0.5, 0,0.5) and (0.5, 0.5, 0), respectively, with *I41/amd* as space group.

To proceed into the doping and co-doping of TiO2 by Cu and Pt, two Ti atoms are substituted with one Cu and Pt atoms. Here, one Ti atom was substituted with one Cu or Pt atom for a doping concentration of 3.125%, 6.25%, and 12.5% respectively.

In the package, we consider a 3×3×2 supercell of TiO2, which contains a consistent volume of atoms, 96 atoms (32 Ti atoms and 64 O atoms). The energy cutoff parameter is chosen RMT × Kmax equal to 7, where RMT is the average radius of the muffin tin (MT) spheres, and Kmax is the cutoff for the wave function basis, the RMT values of Pt, Cu, Ti and O atoms are taken as 1.97, 1.92, 1.88 and 1.61 a. u., respectively. The schematic view of doped and the undoped TiO2 has been shown in fig V.10.

For a best convergence, the total energy has been converted to 10^{-5} Ry/unit cell in the present self-consistent calculations. The k-points were selected through script method by the k-mesh of 4 × 4 × 4 and convergence is set by iteration process up to 0.1×10^{-5} Ry.

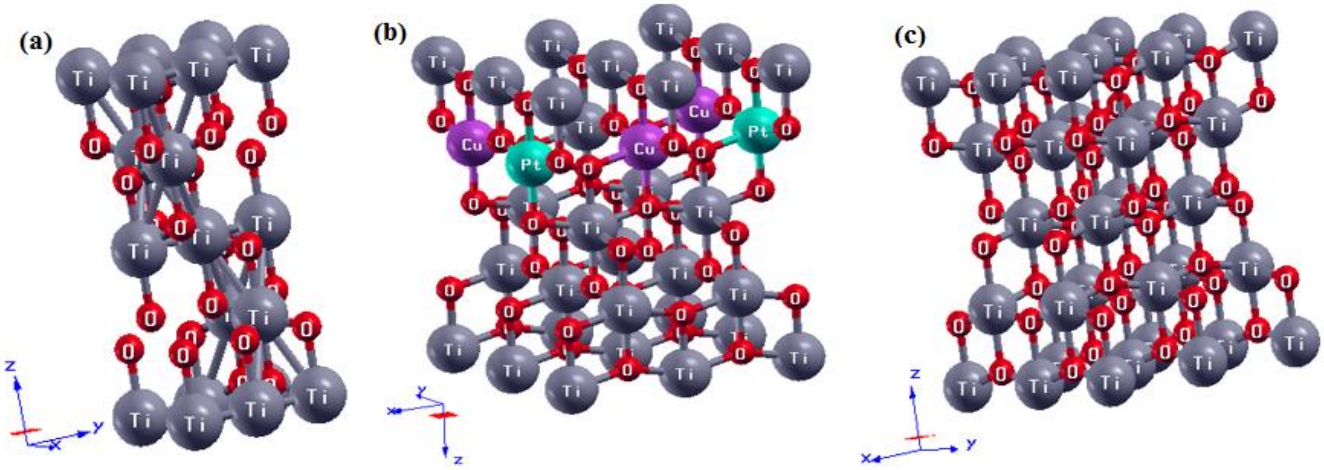

Figure V.10: *Crystal structures of elementary TiO2 (a), supercell TiO2 (b) and (Cu, Pt) co-doped TiO_2 (c).*

V.5.2 Structural properties

The total energy as a function of the unit cell volume around the equilibrium V0 with the aid of Murnaghan's equation [154]. The volume optimization curve is shown in figure V.11. The optimized crystal lattice parameters found are on the basis of successful convergence of the cycle. A comparison of these results with available literature has been given in Table 1, where we can clearly see that the obtained results are matching closely with previous theoretical and experimental results.

And according to the calculations performed on pure anatase, the use of the corrected DFT method weather DFT+U, mBJ or scissor operators leads to improved accuracy in terms of

energetic and crystallographic data and energy gap. The overall characteristics of the energy band structure calculated in the research are consistent with those of previous investigations.

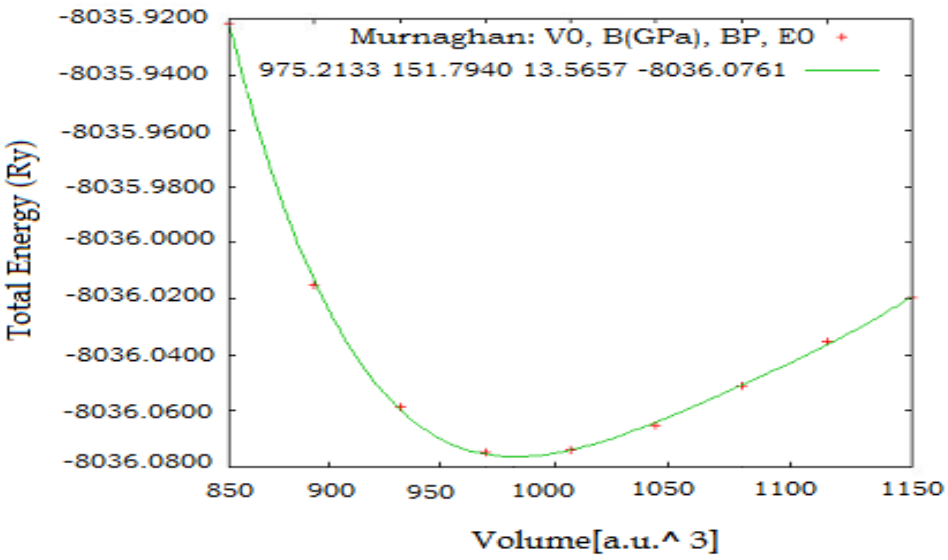

Figure V.11: *The variation of total energy as a function of volume of anatase TiO2.*

Table V.1: Comparison between calculated structural data with other experimental works.

Structural Data				Eg (eV)	Note
a (Å)	c (Å)	c/a	Ti-O		
3.72034	9.3530	2.514	1.925	2.19	GGA:PBE [Present work]
3.7760	9.4860	2.512	1.985	3.205	GGA:PBE-mBJ [Present work]
3.792	9.4875	2.502	1.901	3.2	LDA+U [214]
3.880	9.497	2.448	_____	3.16	LDA+U [215]
3.785	9.5117	2.513	_____	3.20	[214]
3.885	9.690	2.4942	2.0155	3.203	GGA:PBE scissor operator [216]

V.5.3 Electronic properties:

To compare the electrical conductivity of the two materials, electronic properties such as the band structures and density of states of the undoped and doped system were investigated as illustrated in Figs. V.12 and V.13.

The calculated band structure of TiO2 is illustrated in Figure. V.12, the top of valence band approximately locates near the F-point and the bottom of the conduction band locates at the G-point, which relatively approves with other researches, the indirect band gap semiconducting nature of anatase TiO2 [66, 216]. The calculated band gap value for anatase TiO2 is 2.19 eV is consistent with the reported theoretical results [220], but is underestimated compared with the experimental value (Eg = 3.23 eV). By applying the mBJ we can see that the band gap value of TiO2 is increased to 3.205 eV, which has the error very small compared with the experimental value of 3.23 eV, which accords other research having a band gap ranging between {2.7 eV and 3.45 eV} when employing the mBJ approximation [63,217,218]. The theoretical result is far from 3.37 eV obtained from experiment, indicating that the underestimation always exists in the band gap calculations, caused by the lower exchange correlation between electrons made by GGA function.

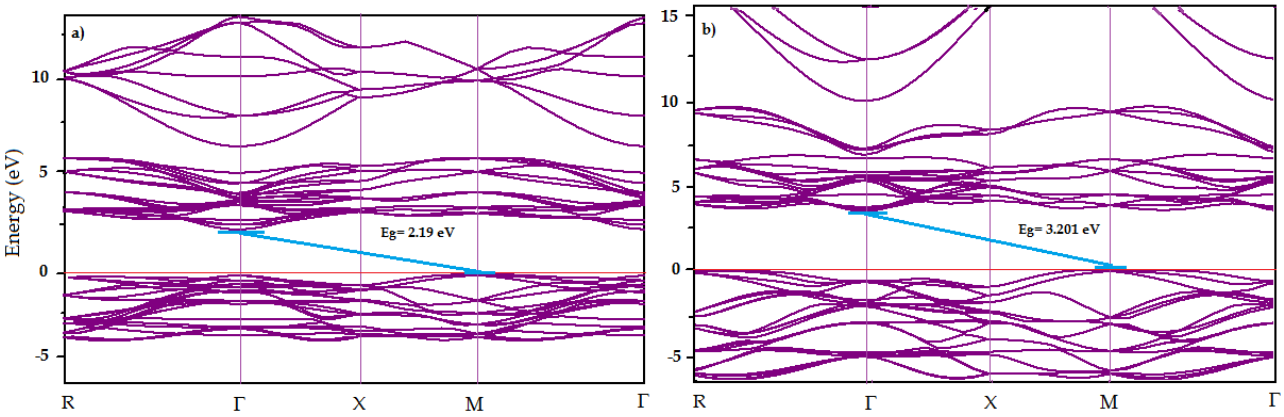

Figure V.12: *Band structure of pure anatase TiO2 with GGA approximation (a) and mBJ (b).*

However, we noticed a significant difference in band gap between the undoped and (Cu, Pt) doped and codoped TiO2, Fig.V.13. After the doping, the band gap is decreased slightly to the value of 2.56 eV for Cu doped TiO2 and 1.75 eV for (Cu, Pt) codoped TiO2, extracted from the band structure showed in Fig. V.13, this decrease in band gap is due to a charge transfer between d orbital of Pt, Cu and Ti. It is worth mentioning that the lower band gap means the higher electrical conductivity [219].

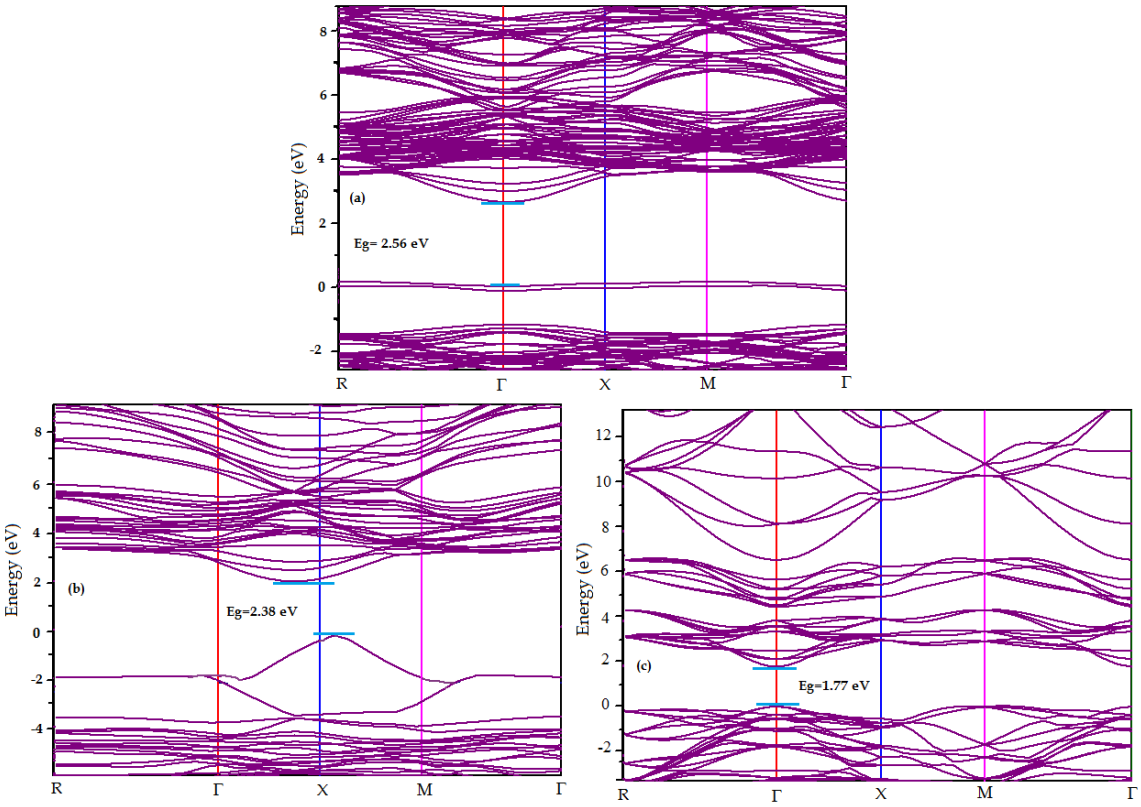

Figure V.13: *Band structure of Cu doped anatase TiO2 with mBJ approximation for various doping concentration, $Ti_{1-x}Cu_xO$ with x = 0.03125 (a), $Ti_{1-x}Cu_xPt_xO$ x = 0.03125 (b) and x=0.625 (c).*

The total density of states (TDOS) and partial density of states (PDOS) for Cu doped and (Cu, Pt) codoped anatase TiO2 in comparison with those of pure anatase TiO2 are shown in Figure V.14. The partial DOS of anatase TiO2, Fig.V.14.a, indicates that the valence bands are dominated by O 2p states with a mixture of Ti 3d states. The mixture is a manifestation of hybridization between O 2p and Ti 3d states. The conduction band has two sub-bands: the lower *t2g* and the upper *eg* and they are split thanks to the O octahedral crystal field.

Based on the DOS calculation, it is observed that the 3d states of Cu is mainly appearing at the valence band, particularly, dominated at the top and bottom of valence band in Fig. V.14. (b) and (c). The Cu and Pt dopant in Cu-doped or either in Cu, Pt codoped TiO2, is the reason behind the presence of the enhanced d states at the uppermost valence band which concords previous theoretical results [155]. The hybridization between the O 2p states or Ti 3d states with the Cu 3d states and Pt 5d states which are delocalized, contribute to the formation of impurity energy levels. This, therefore, can form energy levels in the band gap or hybrid between a minimum

conduction band and a maximum valence band. This finally allows the photogenerated electron-hole pairs to separate, thus contributing to the migration of the photo-excited carriers and the photocatalysis process. [58]

As observed in fig V.14, for pure anatase TiO2, $Ti_{1-x}Cu_xO$ (x=0.03125) and $Ti_{1-x}Cu_xPt_xO$ (x=0.0625), a significant gap value is equal to 2.56, 2.384 and 1.77 eV respectively. This is due to the increasing of d electronic states of Cu-doped TiO2 at the uppermost valence band, which lead to the band gap narrowing, the same behavior was reported earlier by Guo et al [221]. These results are also confirmed in the band structure plotted in figure above.

Thus, Cu, Pt co-doped TiO2, exhibits higher electrical conductivity than anatase TiO2. In addition, the value of density of states near Fermi surface for doped TiO2 (25.6 electrons/eV) is higher than pure TiO2 (11.7 electrons/eV).

According to quantum theory, only electrons near the Fermi level can contribute to current in the external electric field, hence the electrical conductivity of material is proportional to the electrons occupied in the Fermi level [222].

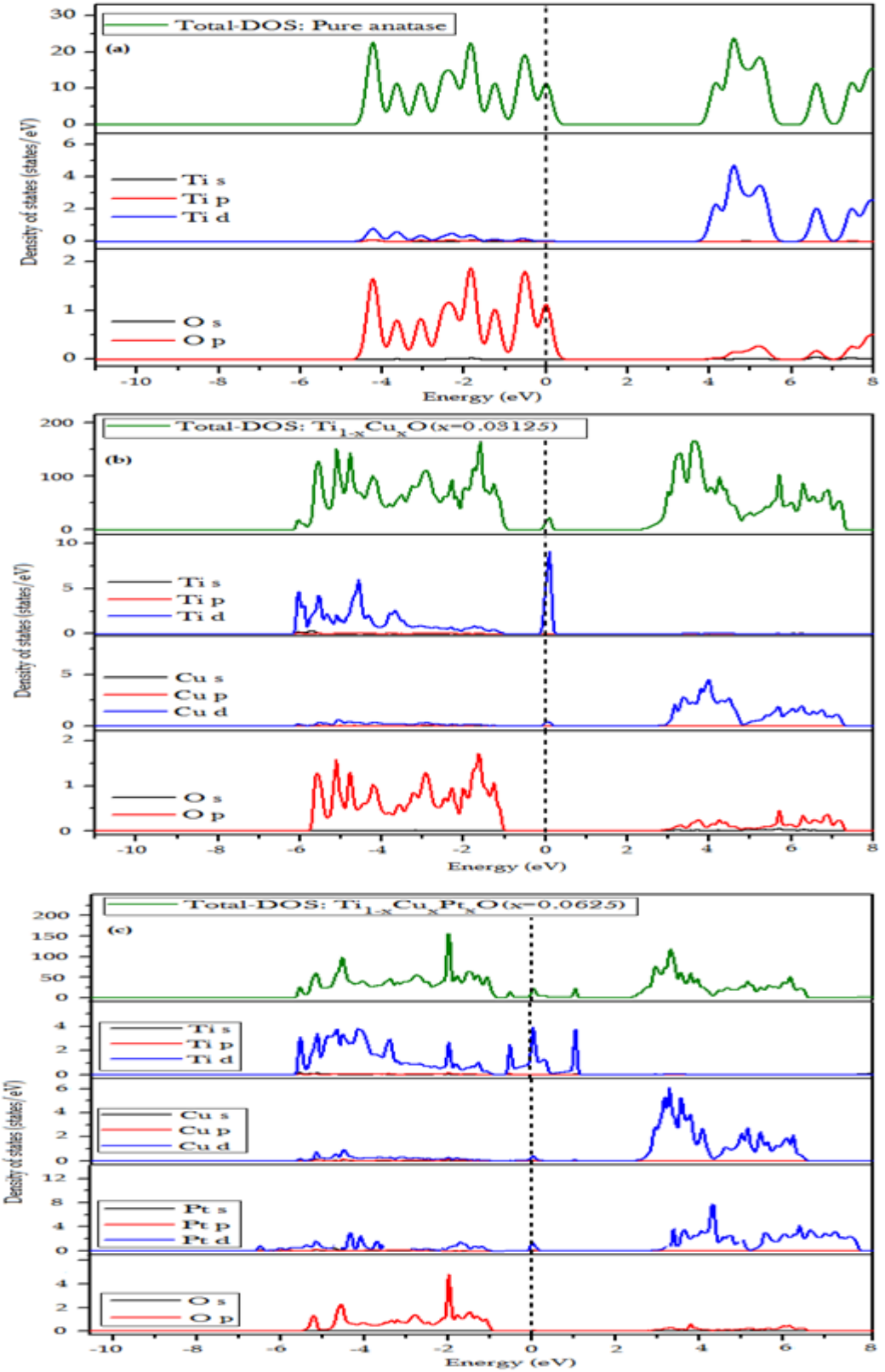

Figure V.14: *Total and partial DOS of pure TiO2 (a), $Ti_{1-x}Cu_xO$ (x=0.03125) (b) and $Ti_{1-x}Cu_xPt_xO$ (x=0.625) (c).*

V.5.4 Optical properties:

The optical properties of pure and doped TiO2 compound were investigated. While the band gap obtained by mBJ correction is close to experimental results, the optical properties are analyzed by using only this approximation. They are described by considering the dielectric function **ε**(ω) related to the interaction between photons and electrons [45], which is mainly contributed from the electronic structures.

The dielectric function (ω) as well as the absorption coefficient α(ω) are described earlier in chapter IV see from eq (IV.1) to eq. (IV.2).

As shown in Figure V.15 (a), the calculated static dielectric constants $\varepsilon_1(\omega)$ are 4.986, 6.01, 8.76 and 10.026 for pure TiO2, $Ti_{1-x}Cu_xO$ (x=0.03125), $Ti_{1-2x}Cu_xPt_xO$ (x=0.03125) and (x=0.0625) respectively. It has been observed for undoped TiO2 that $\varepsilon_1(\omega)$ reaches a maximum at 2.85 eV. The curve decreases and reaches a minimum at 9.3 eV. With the substitution of Copper and platinum for 6.25 %, the constant reaches a maximum at above 3.85 eV. Then, it decreased and becomes negative reaching a minimum at around 8.67 eV.

In the imaginary plot of dielectric function given in Fig. V.15 b. It is well known that the imaginary part of dielectric function can describe the optical transition well. It can be found that the pure TiO2 shows the optical transition at 3.38 eV, which is related to the intrinsic transition between O2p states at the valence band and Ti 3d states at the conduction band. After doping, the intrinsic optical transition is observed having a shift to the low energy range, which means that the band gaps are narrowed by doping with Cu and Pt. The detailed optical transitions are at 1.74, 1.69 and 1.55 eV corresponding to $Ti_{1-x}Cu_xO$ (x=0.03125), $Ti_{1-2x}Cu_xPt_xO$ (x=0.03125) and (x=0.0625) doping concentration respectively. Besides, the maximum of $\varepsilon_2(\omega)$ is reached at about 8.31, 8.25 and 7.61 eV for Cu doped TiO2 at $Ti_{1-x}Cu_xO$ (x=0.03125), $Ti_{1-2x}Cu_xPt_xO$ (x=0.03125) and (x=0.0625) doping concentration respectively, which corresponding to an important absorption peak.

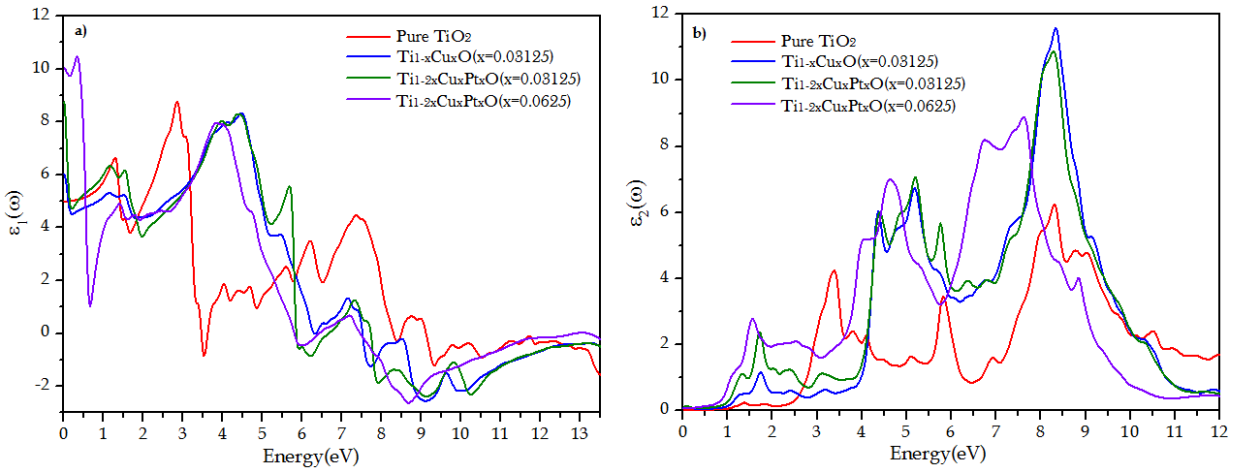

Figure V.15: *(a) real part $\varepsilon_1(\omega)$, (b) imaginary part $\varepsilon_2(\omega)$of the dielectric constant of undoped and (Cu, Pt) codoped anatase TiO2*

Figure V.16 a, demonstrates the optical absorption spectrums as function of wavelength in the range 100-800 nm calculated by mBJ-GGA approximation. It can be observed that the doped TiO2 shows the enhancement of visible light absorption compared to the undoped TiO2 compound. Upon doping with Cu and Pt, it can be seen that the absorption edge is being shifted towards visible region.

The absorption center of Cu-doped TiO2 locates at 260 nm in the case of $Ti_{1-x}Cu_xO$ (3.125%) codoping concentration, and 237 nm in the case of $Ti_{1-2x}Cu_xPt_xO$ (6.25%). The visible light photo-activity of Cu-doped TiO2 was also observed by other experiment reports [223]. Dorothy et al have also reported that the Pt incorporated into TiO2 would definitely enhance the photocatalytic properties on TiO2, and similar optical properties had also been observed [224]. And this improvement could be also seen in fig V.16 b, which shows that the optical conductivity increases with the Cu and Pt doping, compared to the pure TiO2.

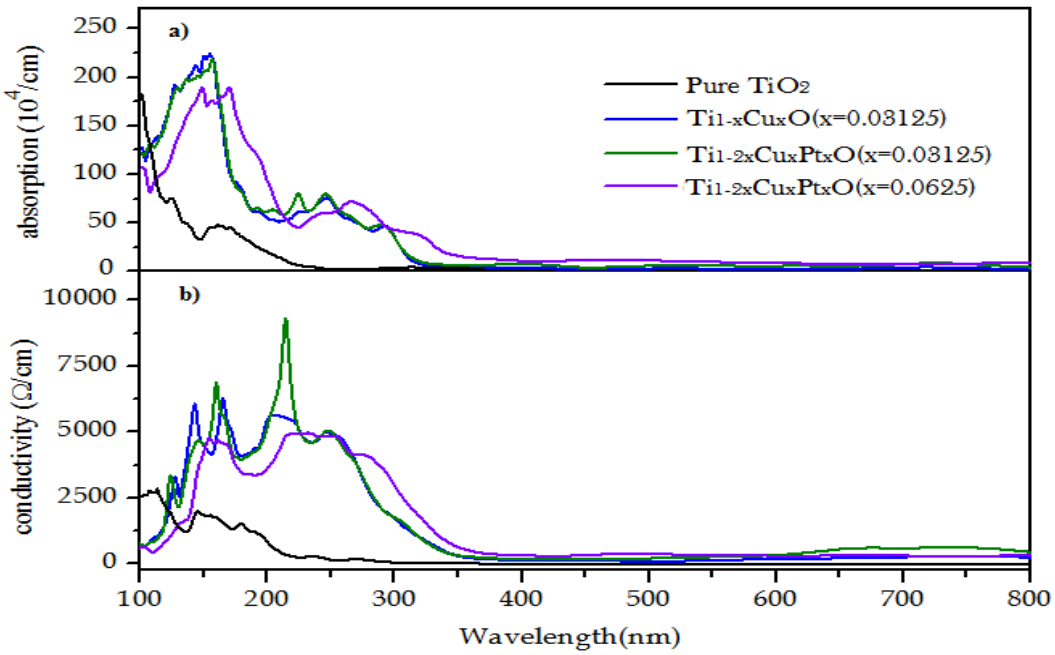

Figure V.16: *(a) absorption coefficient $\alpha(\omega)$ and (b) optical conductivity $\sigma(\omega)$ of undoped and (Cu, Pt) codoped anatase TiO2.*

V.5.5 Transport properties:

The transport coefficients such as the Seebeck coefficient (S), electrical conductivities (σ) and the figure of merit (ZT) of undoped and doped anatase TiO2 compound have been obtained using BoltzTraP Code based on the Boltzmann theory [8] within the following equation respectively [226]:

$$S = \frac{-L^{(1)}}{eTL^{(0)}} \quad \text{(V.6)}$$

Where $L^{(x)}$ is the Lorentz number:

$$L^x = \int_{-\infty}^{+\infty} dE \left(\frac{\partial f_0}{\partial f}\right) g(E)\, V(E)^2 \tau(E)(E - E_f)^x \quad \text{(V.7)}$$

f_0 is the Fermi distribution function: $f_0 = 1 + e^{\left(\frac{(E-E_f)}{k_\beta}\right)-1}$ (V.8)

E_f is the Fermi level, $V(E)$ is the speed of electron: $V(E) = \frac{1}{\hbar \nabla_{kE(k)}}$ (V.9)

$g(E)$ refers to the density of states, τ is the relaxation time and T is the absolute temperature. The electrical conductivity is calculated from the following equation:

$$\sigma = e^2 L(0) \quad \text{(V.10)}$$

Figures V.17 a shows the temperature dependence of Seebeck coefficient in the range of 50 to 800K. From the Figure, the values of the Seebeck coefficient (S) for TiO2 compound appear negative throughout the investigated temperature range, indicating the n-type nature of titanium dioxide. Upon doping, it is noticed that the Seebeck coefficient slightly increases upon codoping with Cu and Pt, for both 3.125 % and 6.25 %, which proves that the number of mobile charge carriers is strongly enhanced.

Seebeck effect consists on the conversion of heat into electric power. It is caused by the movement of free electrons from higher to lower temperature regions, producing a voltage of several microvolts per Kelvin [225].

From Fig. V.17 b, we can obviously see that the electrical conductivity is improved upon adding Pt and Cu impurities to the pure TiO2, and increasing simultaneously with temperature. The noble metals have an electronic structure whose outer band (n-1) d is rich in electrons and the band (ns) half-filled. This band (ns) is superposed with (np) to form a hybridized (sp). As a result, the electrons of (sp) band have access to an almost empty band and will therefore, be able to delocalize on all the atoms forming the solid, we speak then of electron gases providing conduction within the metal.

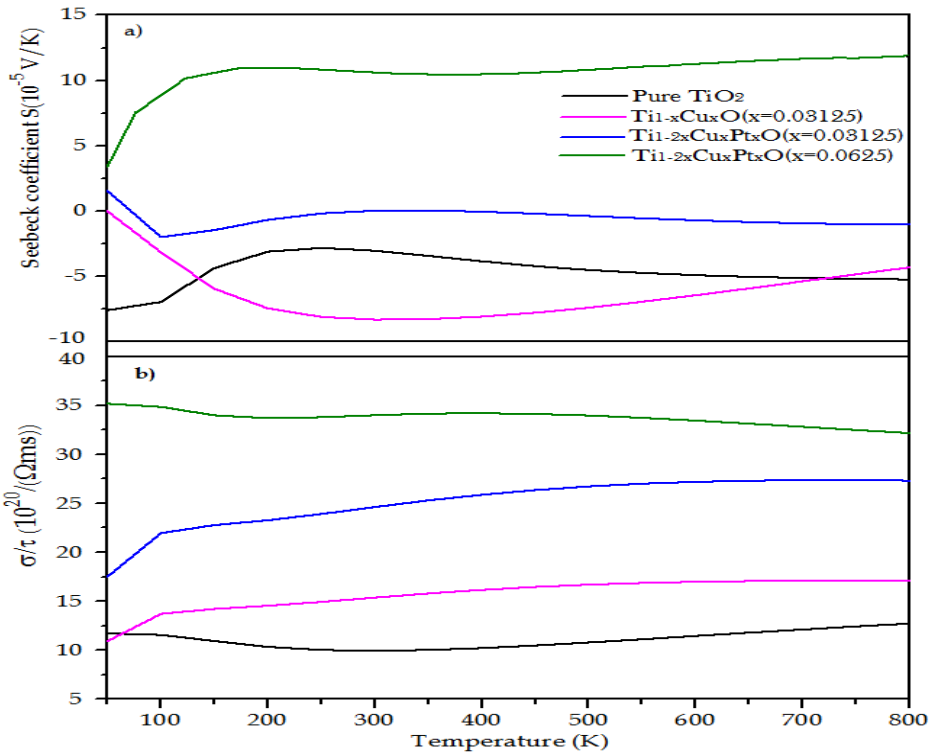

Figure V.17: *Evolution of the Seebeck coefficient (a) and calculated electrical conductivity (σ/τ)(b) as a function of temperature for undoped and (Cu, Pt) codoped TiO2.*

The variation of the figure of merit (ZT) as a function of temperature can be calculated using the values of the electrical conductivity (σ), Seebeck coefficient (S) and thermal conductivity (k), by the following relation [226]:

$$ZT = S^2\sigma T/k \qquad \text{(V.11)}$$

Figure V.18 shows the variation of the figure of merit (ZT) for undoped and doped TiO2 compound in different percentage at annealing temperature of 300K. The value of thermoelectric figure of merit minimum is around 0.02 for pure anatase TiO2 against 0.077 for Cu, Pt codoped TiO2 [$Ti_{1-x}Cu_xPt_xO(x=0.0312)$]. The results shows that figure of merit values can be improved by increasing Cu and Pt composition into the pure TiO2, hence it confirms that this material can be chosen as a suitable candidate for tunable advanced optoelectronic and thermoelectric applications.

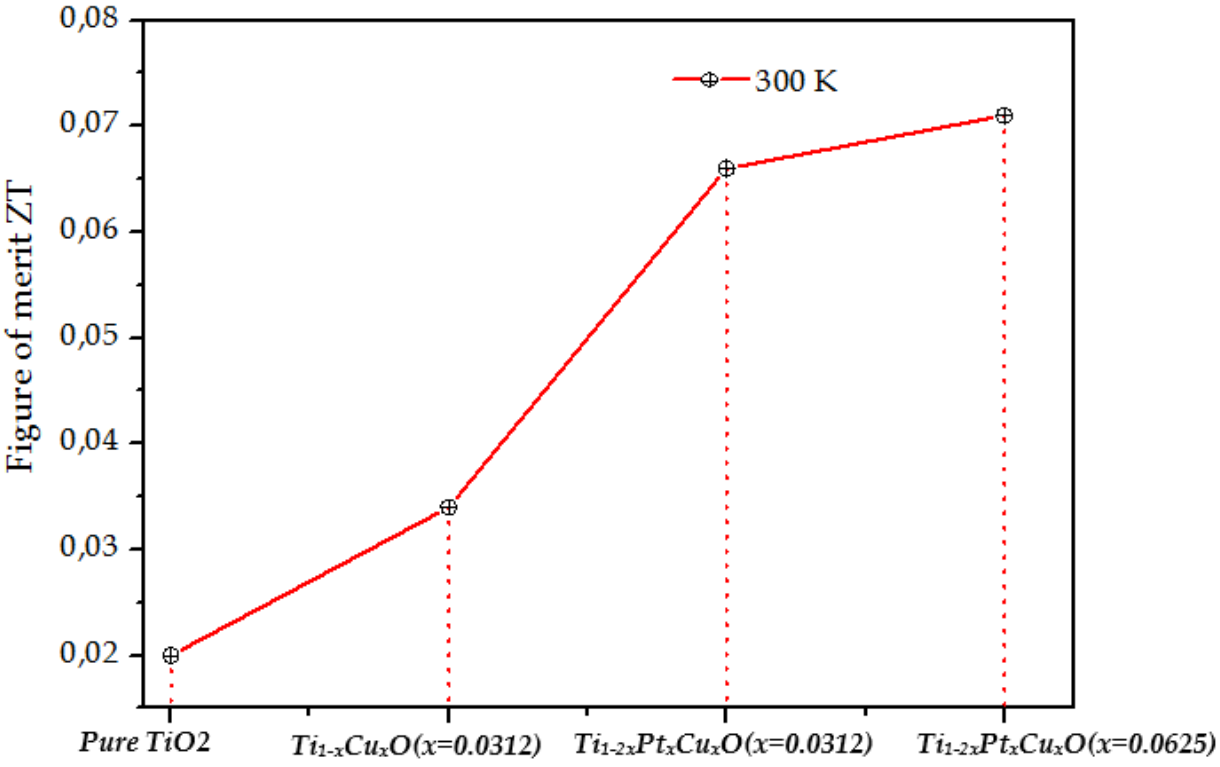

Figure V.18: *Evolution of the figure of merit ZT for undoped and doped TiO2 at annealing temperature of 300K.*

V.6 Conclusion

In summary, the CPTNTs (CuO/Pt-TiO2 NTs) composite has been successfully fabricated by, a simple electro-deposition anodization method. It has been proved that the combination made between the Pt-TiO2 NTs with CuO nanoparticles is an effective way to improve performance of the supercapacitor, and this effect is due from the coupling of pseudocapacitance behavior of CuO NPs and higher surface area of Pt-TiO2 NTs.

The present results for the obtained composite, displays better electrochemical properties, showing high specific capacitance, lower charge transfer resistance than those of pristine TiO2-NTs and Pt-TNTs and excellent cycling stability. It displayed a maximum energy and power densities of ~12.81 Wh Kg^{-1} and 445 W Kg^{-1} respectively at ambient temperature, which confirms the good cycling, and can retain almost 93% of its initial capacitance after 5000 charge–discharge cycles in 1 M Na2SO4 electrolyte.

In addition to that, we have used the density functional theory to investigate the electronic structures and optical properties of undoped and Cu-doped anatase TiO2. Our calculated results

show that the energy gap of anatase TiO2 is substantially improved by mBJ over GGA values toward experimental results. Meanwhile, the energy gap is decreasing when adding copper impurities to the pure TiO2. Our calculated results for optical properties as well as the dielectric functions (both real and imaginary parts) demonstrate the enhancement of visible light absorption of the Cu doped TiO2 compared to the undoped TiO2. Moreover, important transport properties such as Seebeck coefficient (S), figure of merit (ZT) and electrical conductivity (σ) were investigated with the help of Boltzmann theory, which shows an enhancement when incorporating the Cu atoms. Our further study reveals that these excellent improvements are achieved because mBJ potential describes accurately the energy levels of Ti and Cu 3d states and the hybridization between these d states and O p states. The results are promising and confirm that the Cu doped TiO2 can be chosen as a suitable candidate for advanced optoelectronic and thermoelectric applications, as well as energy storage owing to its good electronic properties. These results confirmed and revealed the effectiveness of the CPTNTs electrode by theory through first principles calculations, which proves its effective performance for promising supercapacitor applications.

Summary and outlooks

Summary:

The main goal of this work was to study the electrochemical performance of pure anatase titanium dioxide and copper oxide combined TiO2 dioxide based electrode material for supercapacitor application. During this thesis, an introduction was given about the history and motivation of energy storage devices highlighting supercapacitors (electrochemical capacitors) and its types, followed by a survey of literature of copper oxide and Titanium dioxide materials properties, which are the subject focus of our work.

The essential results of this study can be summarized into two main parts as follows:

1. Structural, optical and electronic properties of copper oxide CuO

In the first part, we studied the structural, electronic, optical and thermoelectric properties of pure CuO using the FP LAPW method based on the DFT density functional theory with the modified Becke-Johnson corrective approach, which provides an improvement for the correction of the energy band-gap calculations. We've calculated the band structure, the density of states, the dielectric function, the reflectivity, the refractive index, the absorption coefficient and the optical conductivity, the results obtained were in good agreement with the theoretical results and experimental.

Our Band structure calculations of CuO using GGA reveals that there is three electronic levels that crossed the Fermi surface set at 0, thus there is no energy gap and CuO is predicted to have a metallic or semi-metallic ground state according others researches. While the mbJ shows no electronic levels crossed by the Fermi surface, and predicts a band gap value about 1.89 eV. Moreover, the optical conduction analysis starts from the energies of about 1.81 eV, which concords our band gap calculation. This value represent the optical energy gap and arrives at a maximum level for 3.04 eV. The average values of the reflection coefficient in the visible spectrum region as well as in the [7-13 eV] region show that the material is semi-transparent in this energy region.

In the experimental part, we have elaborated pure CuO nanoparticles by the sol-gel method, using copper acetate monohydrate (Cu (CH3COO)2, H2O) as a precursor, H2O as a solvent and NaOH was added to this solution as a hydrolysis agent. The samples were annealed at four different temperatures: 200 °C, 400°C, 600°C and 800°C respectively in order to evaluate the effect of the temperature on its structural, morphological, optical and photocatalytic properties. X-ray diffraction measurements revealed an improvement in the crystallinity of samples by comparing the intensity and shape of crystalline peaks with the increase of temperature and also a decrease in the full width at half maximum (FWHM) is observed, suggesting thus a possible change in the grain size. Particle's size of annealed samples were calculated from XRD analysis and compared to those obtained from transmission electronic microscopy.

TEM analysis indicated that the grain size evaluates proportionally with the evolution of temperature, which was well confirmed by XRD results. The optical band gap extracted from UV-Visible spectroscopy indicated that by reducing the CuO nanoparticle's size, the band gap raise to higher values, indicating a blue shift of band gap, which has been attributed to the quantum confinement effect. Photocatalytic degradation of methylene blue was carried out on the as-synthetized and annealed nanoparticles under visible light irradiation. It was found that

almost 80.03% of methylene blue dye were degraded after 540 min UV illumination for samples annealed at 800°C, which show the better photodegradation efficiency. The results have shown that the photocatalytic activity of the samples depended on the annealing temperature that they endured, so in our experiment, the photodegradation performance was improved when increasing the annealing temperature.

2. Electrochemical study on CuO/Pt-TiO2 composite material

In chapter 5, we reported the fabrication of the CPTNTs (CuO/Pt-TiO2 NTs) composite material by a simple electro-deposition anodization method, and further investigate its electrochemical properties. The preparation includes an initial anodic fabrication of well-ordered TiO2 NTs from a Ti substrate, then the sputtering of Pt particles on the top of nanotubes, followed by an electrodeposition of Cu NPs into the as obtained material Pt-TiO2 NTs and then a thermal oxidation was done for copper oxidation. The combination made between the Pt-TiO2 NTs with CuO nanoparticles showed an effective improvement of supercapacitor's performance, and this effect is due from the coupling of pseudocapacitance behavior of CuO NPs and higher surface area of Pt-TiO2 NTs.

CPTNTs have showed better electrochemical properties, depicted in its high specific capacitance, lower charge transfer resistance than those of pristine TiO2-NTs and Pt-TNTs and also an excellent cycling stability. The finding reveals also a maximum energy and power densities of ~12.81 Wh Kg^{-1} and 445 W Kg^{-1} respectively at ambient temperature, which confirms the good cycling, and can retain almost 93% of its initial capacitance after 5000 charge–discharge cycles in 1 M Na2SO4 electrolyte.

In addition to that, we have used the density functional theory to investigate the electronic structures and optical properties of undoped, Cu-doped and (Cu, Pt) codoped anatase TiO2. Our calculated results show that the energy gap of anatase TiO2 is substantially improved by mBJ over GGA values toward experimental results. Meanwhile, the energy gap is decreasing when adding copper or Pt impurities to the pure TiO2. Our calculated results for optical properties as well as the dielectric functions (both real and imaginary parts) demonstrate the enhancement of visible light absorption of the Cu, Pt codoped TiO2 compared to the undoped TiO2. Our further study reveals that these excellent improvements are achieved because mBJ potential describes accurately the energy levels of Ti, Cu and Pt 3d states and the hybridization between these d states and O p states. The results are promising and confirm that the Cu, Pt codoped TiO2 can be chosen as a suitable candidate for advanced optoelectronic and thermoelectric applications, as well as energy storage owing to its good electronic properties. These results confirmed and

revealed the effectiveness of the CPTNTs electrode by theory through first principles calculations, which proves its effective performance for promising supercapacitor applications.

Outlook:

In our work regarding the future research prospects, the aim will be the utilization of *in-situ* characterizing techniques to detect any morphological or structural changes on electrodes during charge-discharge processes. Such detailed studies can provide further insight on the factors behind decreasing capacitance during prolong cycling.

In addition, optimizing CuO contents into the material and trying different electrolytes would be of a precious investigation to further improve the device resistance, power and cycling stability…

Bibliography

[1] X. Liu, G. Sheng, M. Zhong, X. Zhou, "Dispersed and size-selected WO3 nanoparticles in carbon aerogel for supercapacitor applications", *Materials & Design*., vol. 141, no. 5, pp. 220-229, 2018.

[2] A.K Mondal, D. Su, S. Chen, K. Kretschmer, X. Xie, H. Ahn and G. Wang, "A Microwave Synthesis of Mesoporous NiCo2O4 Nanosheets as Electrode Materials for Lithium-Ion Batteries and Supercapacitors", *ChemPhysChem.*, no. 15, pp. 1-8, 2014.

[3] F. Shi, L. Li, X. Wang, C. Gu and J.P Tu, "Metal oxide/hydroxide based materials for supercapacitors", ***RSC Adv.***, vol. **4**, pp. 41910-41921, 2014.

[4] L. Zhang. The study of nickel copper based supercapacitors for energy storage. PhD thesis, National University of Singapore, 2016.

[5] L. Zhu, S. Zhang, Y. Cui, H. Song, X. Chen, "One step synthesis and capacitive performance of graphene nanosheets/Mn3O4 composite", *Electrochimica Acta.,* no. 89, pp. 18-23, 2013.

[6] Y. Wu, G. Gao, H. Yang, W. Bi, X. Liang, Y. Zhang, G. Zhang, and G. Wu, "Controlled synthesis of V_2O_5/MWCNT core/shell hybrid aerogels through a mixed growth and self-assembly methodology for supercapacitors with high capacitance and ultralong cycle life", ***J. Mater. Chem. A***, no. **3**, pp. 15692-15699, 2017.

[7] Z. Gao1, C. Bumgardner, N. Song, Y. Zhang, J. Li2 & X. Li, "Cotton-textile-enabled flexible self-sustaining power packs via roll-to-roll fabrication", *Nat Commun.*, **7,** 11586 2016.

[8] L. Attou, B. Jaber, H. Ez-Zahraouy, "CuO NPs on Pt‑sputtered TiO2‑TNTs composite material for supercapacitors applications: investigation on its electrochemical properties". *Appl. Phys. A.,* vol. 125, 560, pp. 1-12, 2019.

[9] Y.G. Wang, X.G. Zhang. Enhanced electrochemical capacitance of NiO loaded on TiO2 nanotubes. *J Electrochem Soc*, 152, pp. 671-676, 2005.

[10] A. Bendavid, P.J. Martin, Å. Jamting, H. Takikawa, "Structural and optical properties of titanium oxide thin films deposited by filtered arc deposition", *Thin Solid Films,* vol 355-356, pp. 6-11, 1999.

[11] Y.Z Wu, Y. Ding, T. Hayat, A. Alsaedi, S.Y Dai, "Enlarged Working Potential Window for MnO2 Supercapacitors with Neutral Aqueous Electrolytes", *App Surf Sci,* vol. 459, pp. 430-437, 2018.

[12] B. Saravanakumar, K.K. Purushothaman, G. Muralidharan, "V2O5 / nitrogen enriched mesoporous carbon spheres nanocomposite as supercapacitor electrode", *Mesoporous Materials,* vol. 258, pp. 83-94, 2017.

[13] R. Prasad, "Thermal stability and degradation of starch derivatives", *J. Therm. Anal. Calorim.* 85, pp. 279-284, 2006.

[14] X. Fan. "Rational Design of Nanostructured Electrode Materials for High-performance Supercapacitors". PhD thesis, University of Waterloo, 2015.

[15] M. Winter and R. J. Brodd, "What Are Batteries, Fuel Cells, and Supercapacitors?" Chem. Rev. **104**, 4245 (2004).

[16] Shukla, A. K., Sampath, S., Vijayamohanan, K. "Electrochemical supercapacitors: Energy storage beyond batteries", *Current science-bangalore-*, *79*(12), pp. 1656-1661, 2000.

[17] Chen, Y. F., Li, Y. Y., Deng, M. G. "Principles and applications of supercapacitors". *Electronic components and materials*, 27(4), 06, 2008.

[18] Zheng, J. P., Jow, T. R. "A new charge storage mechanism for electrochemical capacitors". *J. The Electrochemical Society*, 142(1), L6-L8, 1995.

[19] F. Béguin and E. Frackowiak, "Supercapacitors: Materials, Systems and Applications". Wiley-VCH Verlag GmbH & Co. KGaA, Weinheim, Germany, 2013.

[20] Augustyn, V., Simon, P., Dunn, B. (2014). Pseudocapacitive oxide materials for high-rate electrochemical energy storage. *Energy & Environmental Science*, *7*(5), 1597-1614.

[21] F. Béguin, E. Raymundo-Piñero, and E. Frackowiak, Electrical Double-Layer Capacitors and Pseudocapacitors. CRC Press, 2009.

[22] Zhong, C.; Deng, Y.; Hu, W.; Qiao, J.; Zhang, L.; Zhang, J.: A review of electrolyte materials and compositions for electrochemical supercapacitors. *Chem. Soc. Rev.* 2015.

[23] Conway, B. E. "Electrochemical Supercapacitors: Scientific Fundamentals and Technological Applications". New York, Kluwer-Plenum, 1999.

[24] Kotz, R. and M. Carlen, "Principles and applications of electrochemical capacitors", Electrochimica Acta, 45 15-16, 2483-2498, 2000.

[25] Whittingham, M. S. "History, Evolution, and Future Status of Energy Storage". *Proceedings of the IEEE, 100*, pp. 1518-1534, 2012.

[26] Shi, F.; Li, L.; Wang, X.-l.; Gu, C.-d.; Tu, J.-p.: Metal oxide/hydroxide-based materials for supercapacitors. *RSC Adv. 4*, pp. 41910-41921, 2014.

[27] Xu, B.; Wu, F.; Chen, R.; Cao, G.; Chen, S.; Wang, G.; Yang, Y.: Room temperature molten salt as electrolyte for carbon nanotube-based electric double layer capacitors. *J. Power Sources, 158*, pp. 773-778, 2006.

[28] Deng, W.; Ji, X.; Chen, Q.; Banks, C. E.: "Electrochemical capacitors utilizing transition metal oxides: an update of recent developments". *RSC Adv., 1*, 1171-1178, 2011.

[29] C. C. Hu, K. H. Chang, M. C. Lin and Y. T. Wu, Design and tailoring of the nanotubular arrayed architecture of hydrous ruo2 for next generation supercapacitors, Nano Lett., 6, pp. 2690-2695, 2006.

[30] H. Zhang, G. Cao, Z. Wang, Y. Yang, Z. Shi and Z. Gu, Growth of Manganese oxide nanoflowers on vertically-aligned carbon nanotubes arrays for high-rate electrochemical capacitive energy storage, Nano Lett., 8 2664, 2008.

[32] Zhu J, He J, Facile Synthesis of Graphene-Wrapped Honeycomb MnO_2 Nanospheres and Their Application in Supercapacitors *ACS Appl Mater Interfaces*, 2012, **4**, 1770.

[33] L. Z. Fan, Y. S. Hu, J. Maier, P. Adelhelm, B. Smarsly and M. Antonietti, High electroactivity of polyaniline in supercapacitors by using a hierarchically porous carbon monolith as a support, Adv. Funct. Mater., 17 3083-3087, 2007.

[34] Wang, H.; Casalongue, H. S.; Liang, Y.; Dai, H.: Ni(OH)2 Nanoplates Grown on Graphene as Advanced Electrochemical Pseudocapacitor Materials. *J. Am. Chem. Soc.* **2010**, *132*, 7472-7477.

[35] Wang, Y.; Yang, X.; Qiu, L.; Li, D.: Revisiting the capacitance of polyaniline by using graphene hydrogel films as a substrate: the importance of nano-architecturing. *Energy Environ Sci* **2013**, *6*, 477-481.

[36] Tomé, L. I. N.; Carvalho, P. J.; Freire, M. G.; Marrucho, I. M.; Fonseca, I. M. A.; Ferreira, A. G. M.; Coutinho, J. A. P.; Gardas, R. L.: Measurements and Correlation of High-Pressure Densities of Imidazolium-Based Ionic Liquids. *J. Chem. Eng. Data* **2008**, *53*, 1914-1921.

[37] Taylor, A. W.; Licence, P.: X-Ray Photoelectron Spectroscopy of Ferrocenyl- and Ferrocenium-Based Ionic Liquids. *Chemphyschem* **2012**, *13*, 1917-1926.

[38] Foo, C.Y., et al., *Flexible and Highly Scalable V2O5-rGO Electrodes in an Organic Electrolyte for Supercapacitor Devices.* Advanced Energy Materials, **4** (12), 2014.

[39] Nam, K.-W. and K.-B. Kim, *A study of the preparation of NiO x electrode via electrochemical route for supercapacitor applications and their charge storage mechanism.* Journal of the Electrochemical Society, 2002. **149**(3): p. A346-A354.

[40] Wang, Y., et al., *Synthesis of 3D-nanonet hollow structured Co3O4 for high capacity supercapacitor.* ACS applied materials & interfaces, 2014. **6**(9): p. 6739-6747.

[41] C. Hu, W. Chen, K. Chang, How to Achieve Maximum Utilization of Hydrous Ruthenium Oxide for Supercapacitors, Journal of The Electrochemical Society, 151(2004) A281-A290.

[42] C. Hu, C. Wang, Improving the utilization of ruthenium oxide within thick carbon-ruthenium oxide composites by annealing and anodizing for electrochemical supercapacitors, Electrochemistry Communications, 4 pp. 554-559, 2002.

[43] W. Yong-gang, Z. Xiao-gang, Preparation and electrochemical capacitance of RuO2/TiO2 nanotubes composites, Electrochimica Acta, 49, 1957-1962, 2004.

[44] S. Ju, J. Li, J. Liu, P. Chen, Y. Ha, I. N. Ishikawa, H. Chang, C. Zhou, A. Facchetti, D.B. Janes and T.J. Marks, Nano Lett. 8 (2008) 997.

[45] S.S. Raut, G.P. Patil, P.G. Chavan, B.R. Sankapal, "Vertically aligned TiO2 nanotubes: Highly stable electrochemical supercapacitor", J. Electroanal. Chem. **780**, pp. 197-200, 2016.

[46] Z. Song, W. Liu, N. Sun, W. Wei, Z. Zhang, H. Liu, G. Liu, Z. Zhao, "One-step self-assembly fabrication of three-dimensional copper oxide/graphene oxide aerogel composite material for supercapacitors", *Solid State Commun*. **287**, pp. 27-30, 2019.

[47] S. Sabbaghi et al,"Effect of temperature and time on morphology of CuO nanoparticle during synthesis".*In.J.Nano Dimens.*3(1): 69-73 ISSN:2008-8868, 2012.

[48] Ohya, Y., Ito, S., Ban, T. and Takahashi, Y. (2000) Prepa-ration of CuO thin films and their electrical conductivity. *Eng. Mater,* **181**, 113-116.

[49] Balamurugan, B. and Mehta, B.R. (2001) Optical and structural properties of nanocrystalline copper oxide thin films prepared by activated reactive evaporation. *Thin Solid Films*, **396**, 90-96.

[50] A.A. Ogwu, E. Bouquerel, O. Ademosu, S. Moh, E. Crossan, F. Placido, « An investigation of the surface energy and optical transmittance of copper oxide thin films prepared by reactive magnetron sputtering », *Acta Materialia* 53, 5151–5159, 2005.

[51] E.M. Alkoy, P.J. Kelly, Vacuum 79 (2005) 221–230.

[52] Dangxin Wu and Qiming Zhang, Phys. Rev. B 73, 235206 (2006).

[53] S.A. Mahmouda, A.A. Akl, S.M. Al-Shomar, "Effect of some preparative parameters on optical properties of spray deposited iridium oxide thin films", *Physica B*, 404, 2151, 2009.

[54] Shymaa K. Hussian, "Study of Optical properties of Copper Oxide (CuO) thin film prepared by SPD technique", *MJPS*, vol. 4, No. 1, 2017.

[55] G. Wang, J. Huang, S. Chen, Y. Gao, D. Cao, "Preparation and supercapacitance of CuO nanosheet arrays grown on nickel foam", Volume 196, Issue 13, 1, pp. 5756-5760, 2011.

[56] Rehana D, Mahendiran D, Kumar RS, Rahiman AK, "Evaluation of antioxidant and anticancer activity of copper oxide nanoparticles synthesized using medicinally important plant extracts", *J.biopha*, 2017.

[57] Yu. P. Sukhorukov, B. A. Gizhevskii, E. V. Mostovshchikova, A. Ye. Yermakov, S. N. Tugushev, and E. A. Kozlov, "Nanocrystalline Copper Oxide for Selective Solar Energy Absorbers", vol. 32, No. 2, pp. 132-135, 2006.

[58] Paramasivam, I., J.M. Macak, and P. Schmuki, "Photocatalytic activity of TiO_2 nanotube layers loaded with Ag and Au nanoparticles". *Electrochemistry Communications*, **10**(1): pp. 71-75, 2008.

[59] Qiu, J., Z. Jin, Z. Liu, X. Liu, G. Liu, W. Wu, X. Zhang, and X. Gao, *Fabrication of TiO_2 nanotube film by well-aligned ZnO nanorod array film and sol–gel process.* Thin Solid Films, **515**(5): pp. 2897-2902, 2007.

[60] Salari, M., S.M. Mousavi khoie, P. Marashi, and M. Rezaee, *Synthesis of TiO_2 nanoparticles via a novel mechanochemical method.* Journal of Alloys and Compounds, **469** (1-2): pp. 386-390, 2009.

[61] Lee, J. and J.Y. Jho, "Fabrication of highly ordered and vertically oriented TiO_2 nanotube arrays for ordered heterojunction polymer/inorganic hybrid solar cell". *Solar Energy Materials and Solar Cells*, **95**(11): pp. 3152-3156, 2011.

[62] Beltrán, A., L. Gracia, and J. Andrés, "Density Functional Theory Study of the Brookite Surfaces and Phase Transitions between Natural Titania Polymorphs". *The Journal of Physical Chemistry B*, **110** (46): pp. 23417-23423, 2006.

[63] Landmann, M., E. Rauls, and W.G. Schmidt, "The electronic structure and optical response of rutile, anatase and brookite TiO_2". *Journal of Physics: Condensed Matter*, **24** (19): pp. 195503, 2012.

[64] B. O'Regan, M. Grätzel, "A low-cost, high-efficiency solar cell based on dye sensitized colloidal TiO2 Films", *Nature*, 353, 737-740, **1991**.

[65] X. D. Li, D. W. Zhang, S. Chen, Z. A. Wang, Z. Sun, X. J. Yin, S. M. Huang, "Enhancing efficiency of dye-sensitized solar cells by combining use of TiO2 nanotubes and nanoparticles", *Mater. Chem. Phys*., 124, 179-183, **2010**.

[66] Asahi, R.; Taga, Y.; Mannstadt, W.; Freeman, A. J. Electronic and optical properties of anatase TiO2. *Phys. Rev. B* **2000**, *61*, 7459.

[67] Q. T. Du, J. S. Tan, Q. T. Wang, C. Y. Li, X. H. Liu, R. S. Cai, Y. H. Ding, Y. Q. Wang, J. Anal. Methods Chem 406162 (2012) 1-8.

[68] M. Ge, C. Cao, J. Huang, S. Li, Z. Chen, K.-Q. ZHANG, S. S. Al-deyab, Y. Lai, "A review of one-dimensional TiO2 nanostructured materials for environmental and energy applications," *J. Mater. Chem. A*, vol. 4, pp. 6772–6801, 2016.

[69] M. A. V. Zwilling, E. Darque-Ceretti, "Anodic oxidation of titanium and TA6V alloy in chromic media. An electrochemical approach," *Electrochim. Acta*, vol. 45, pp. 921–929, 1999.

[70] J. J. Kelly, "The influence of fluoride ions on the passive dissolution of titanium," *Electrochim. Acta*, vol. 24, no. 12, pp. 1273–1282, 1979.

[71] D. Gong, C. A. Grimes, O. K. Varghese, W. Hu, R. S. Singh, Z. Chen, and E. C. Dickey, "Titanium oxide nanotube arrays prepared by anodic oxidation", *J.Mater. Res.*, vol. 16, no. 12, pp. 3331–3334, 2001.

[72] M. Madian, L. Giebeler, M. Klose, T. Jaumann, M. Uhlemann, A. Gebert, S. Oswald, N. Ismail, A. Eychmüller, and J. Eckert, "Self-Organized TiO2/CoO nanotubes as potential anode materials for lithium ion batteries," *ACS Sustain. Chem. Eng.*, vol. 3, no. 5, pp. 909–919, 2015.

[73] C. Ruan, M. Paulose, O. K. Varghese, G. K. Mor, and C. A Grimes, "Fabrication of highly ordered TiO2 nanotube arrays using an organic electrolyte," *J. Phys. Chem. B*, vol. 109, no. 33, pp. 15754–15759, 2005.

[74] X. Quan, S. Yang, X. Ruan, and H. Zhao, "Preparation of titania nanotubes and their environmental applications as electrode," *Environ. Sci. Technol.*, vol. 39, no. 10, pp. 3770–3775, 2005.

[75] S. P. Albu, A. Ghicov, J. M. Macak, and P. Schmuki, "250 μm long anodic TiO2 nanotubes with hexagonal self-ordering," *Phys. status solidi – Rapid Res. Lett.*, vol. 1, no. 2, pp. R65–R67, 2007.

[76] H. E. Prakasam, K. Shankar, M. Paulose, O. K. Varghese, and C. A. Grimes, "A new benchmark for TiO2 nanotube array growth by anodization", *J. Phys. Chem. C*, vol. 111, no. 20, pp. 7235–7241, 2007.

[77] D. Regonini, "Anodised TiO_2 Nanotubes: Synthesis, Growth Mechanism and Thermal Stability". PhD thesis, University of bath, 2008.

[78] J. M. Macak, K. Sirotna, and P. Schmuki, "Self-organized porous titanium oxide prepared in Na2SO4/NaF electrolytes," *Electrochim. Acta*, vol. 50, no. 18, pp. 3679–3684, 2005.

[79] H. Tsuchiya, J. M. Macak, L. Taveira, E. Balaur, A. Ghicov, K. Sirotna, and P. Schmuki, "Self-organized TiO2 nanotubes prepared in ammonium fluoride containing acetic acid electrolytes," *Electrochem. Commun.* vol. 7, no. 6, pp. 576–580, Jun. 2005.

[80] C. A. Grimes, "Synthesis and application of highly ordered arrays of TiO2 nanotubes," *J. Mater. Chem.*, vol. 17, no. 15, pp. 1451–1457, 2007.

[81] Kiyoung Lee, AncaMazare, Patrik Schmuki, *Chem. Rev*, 2014, **114**, 9385

[82] T. Tian, X.-F. Xiao, R.-F. Liu, H.-D. She, X.-F. Hu, *J. Mater.Sci.*, 2007, **42**, 5539

[83] J. Tao, J. Zhao, C. Tang, Y. Kang, Y. Li, *New J. Chem*., 2008, **32**,2164.

[84] Gopal K. Mor, Oomman K. Varghese, Maggie Paulose, Karthik Shankar, Craig A. Grimes, *Solar Energy Materials & Solar Cells*, 2006, 90, 2011.

[85] Abaker M., Umar, A. Baskoutas S., Kim S.H., Hwang S.W., in: Structural and optical properties of CuO layered hexagonal discs synthesized by a low-temperature hydro-thermal process, J. Phys. D: Appl. Phys. 44, 155, (2011).

[86] Camelia V. Stan, Christine M. Beavers, Martin Kunz and Nobumichi Tamura, "X-Ray Diffraction under Extreme Conditions at the Advanced Light Source", Quantum Beam Sci, 2, 4, 2018.

[87] F. Razzaghi, C. Debiemme-Chouvy, F. Pillier, H. Perrot, O. Sel, Ion intercalation dynamics of electrosynthesized mesoporous WO3 thin films studied by multi-scale coupled electrogravimetric methods, Phys. Chem. Chem. Phys. 17 (2015) 14773–14787.

[88] B.J. Inkson, "Scanning electron microscopy (SEM) and transmission electron microscopy (TEM) for materials characterization", *Mat. Char. NDE*, pp. 17-43, 2016.

[89] J. McAneney, Characteristics of Thin and Ultrathin Film Ferroelectric Capacitor Structures. PhD thesis, Queen's University, 2005.

[90] Wooten, F., *Optical Properties of Solids*; Academic press, 2013.

[91] A. Nishino, J. power sources, vol. 60, pp. 137-147 (1996).

[92] Functional Coatings: Research Areas, KIT IAM -Applied Materials Physics Group, University of the State of Baden-Wuerttemberg and National Laboratory of the Helmholtz Association, Web, http://www.iam.kit.edu/awp/english/261.php.

[93] M. Born and J. R. Oppenheimer, Ann. Phys. 87, 457 (1927).

[94] D.R. Hartree, Proc. Cambridge Philos. Soc., 24: 89, 1928.

[95] V. Fock, Z. Phys. 61, 126 (1930); 62, 795 (1930).

[96] E. P. Wigner, Trans. Faraday Soc., 34, 678 (1938).

[97] F. Jensen, 1st edn. John Wiley and Sons, NewYork (1999).

[98] W. Koch and M. C. Holthausen, "A Chemist's Guide To Density Functional Theory", 2nd Ed. Wiley-VCH, Weinheim, Germany, (2000).

[99] J. N. Harvey, 112, 151 (2004).

[100] E. Fermi. Rend.Accad.Naz.Lincei. 6, 602 (1927).

[101] P. A. M. Dirac, Proc. Cambridge Phil. Roy. Soc. 26:376-385, 1930.

[102] J. C. Slater. Phys. Rev. **81**, 385 (1951).

[103] P. Hohenberg and W. Kohn. Phys. Rev. B, 136: pp. 864-870, 1994.

[104] W. Kohn and L.J. Sham. Phys. Rev. **140**, A1133 (1965).

[105] L. Hedin and B. I. Lundqvist, J. Phys. C 4, 2064 (1971).

[106] S. H. Vosko, L. Wilk and M. Nussair, Can. J. Phys. 58, 1200 (1980).

[107] J. P. Perdew and A. Zunger, Phys. Rev. B 23, 5048 (1981).

[108] D.M. Ceperly and B. L. Alder, Phys. Rev. Lett, vol. 45, 566, (1980).

[109] J. P. Perdew, Phys. Rev. Lett. 55, 1665 (1985).

[110] V. ANISIMOV and Y. IZYUMOV, Electronic Structure of Strongly Correlated Materials, Springer 2010, ISBN 978-3-642-04825-8.

[111] S.L. Dudarev, G.A. Botton, S.Y. Savrasov, C.J. Humphreys and A.P. Sutton, phys. Rev. B (57), 1505-1509 (1998).

[112] M. Shishkin, M. Marsman, and G. Kresse, Phys. Rev. Lett. Vol. 99, 246403, (2007).

[113] A. D. Becke and E. R. Johnson, J. Chem. Phys. 124, 221101 (2006).

[114] F. Tran and P. Blaha, Phys. Rev. Lett. 102, 226401 (2009).

[115] A. D. Becke and M. R. Rouseel, Phys. Rev. A39, 3761 (1989).

[116] J. C. Slater, Phys. Rev. 51, 846 (1937).

[117] J.C. Slater, Advances in Quantum Chemistry 1, 35 (1964).

[118] V. Heine and M. J. G. Lee. Phys. Rev. Lett 27, 811 (1970).

[119] W. C. Topp and J. J. Hopfield, Phys. Rev. B7, 1295 (1974).

[120] J. C. Phillips, Phys. Rev. 112, 685 (1985).

[121] T. Starkloff and J. D. Joannopoulos, Phys. Rev. B 16, 5212 (1977).

[122] G. Kresse, J. Hafner and R. J. Needs, J. Phys. Condens. Matter 4, 7451 (1992).

[123] T. Takeda and J. Kubler, J. Phys. F5, 661 (1979).

[124] O.K. Andersen, Phys. Rev. B12, 3060-3083 (1975).

[125] D. R Hamann, Phys. Rev. Lett. 212, 662 (1979).

[126] P. Blaha et al. WIEN97, Technical University. Vienna, (1997).

[127] P. Blaha et al. «An Augmented Plane Wave + Local Orbitals Program for Calculating Crystal Properties». Techn. Universitat. Wien, Austria, (2001).

[128] P. Blaha, K. Schwarz, G. Madsen, D. Kvasnicka, J. Luitz: WIEN2k userguide (2013).

[129] R. Katwal, H. Kaur, G. Sharma, M. Naushad, D. Pathania, Electrochemical synthesized copper oxide nanoparticles for enhanced photocatalytic and antimicrobial activity, J. Ind. Eng. Chem. **2015**, 2566, 1-12.

[130] F Zhao *et al.* J Phys-Condens Mat 20 425- 208 (2008)

[131] Y Zhang *et al.* J Appl Phys 105 086-103 (2009).

[132] Das, S., Majumdar, S., & Giri, S *Applied Surface Science*, *257*(24), 10775–10779, (2011).

[133] Paudel, S., Dandeliya, S., Chaurasiya, R., Srivastava, A., & Kaphle, G. *Journal of Magnetism and Magnetic Materials*, p 8-14, (2015).

[134] Wang, W., Xu, L., Zhang, R., Xu, J., Xian, F., Su, J., & Yang, F. Chemical Physics Letters, 721, 57–61 (2019).

[135] M. ul haq, M. Iqbal, M. A. Z. G. Sial, S. Shabbir, M. Siddiq, A. Iqbal. Journal of Photochemistry and Photobiology A: Chemistry. 335 112-118 (2017).

[136] Chtouki, T., Taboukhat, S., Kavak, H., Zawadzka, A., Erguig, H., Elidrissi, B., & Sahraoui, B. (2018). Abstract. *Journal of Physics and Chemistry of Solids*.

[137] Moosavifard, S. E., El-kady, M. F., Rahmanifar, S., Kaner, R. B., & Mousavi, M. F. ACS Appl. Mater. Interfaces, 7, 8, 4851-4860 (2015).

[138] Zhao, T., Yang, W., Ji, X., Jin, W., Hu, J., & Li, T. Applied Surface Science, Vol 460, p 58-64 (2017).

[139] Kim, D., Lee, G., Lee, S., Kim, J., Lee, H. J., & Kim, D. *Journal of Alloys and Compounds*, Vol 707, p 275-280 (2016). SC.

[140] Zhao, W., Huang, Y., & Li, Z. *Nano Energy*. Vol 59, p 229-236, (2019).

[141] Yuan, W., Qiu, Z., Chen, Y., Zhao, B., Liu, M., & Tang, Y. *Electrochimica Acta*. Vol 267, p: 150-160, (2018).

[142] T. Ishihara, M.Higuchi, T.Takagi, M. Ito, H. Nishiguchi, T.Takita, Preparation of CuO thin films on porous BaTiO3 by self-assembled multilayer film formation and application as a CO2 sensor, J mater Chem., **1998**, 8, 2037-2042.

[145] Wang, Y., Lany, S., Ghanbaja, J., Chen, Y. P., Soldera, F., Mücklich, F., Chen, Y. P. Physical Review B94, 245418 (2016).

[146] Mishra, A. K., Roldan, A., & Leeuw, N. H. De. *J. Phys. Chem. C*, 120 (4), pp 2198–2214Study (2016).

[147] P. Chand, A. Gaur, A. Kumar, Study of CuO nanoparticles synthesized by sol-gel method, AIP Conference Proceedings, **2011**, 211, 1393.

[148] R. Hemanth, M. Sekar, B. Suresha, Effects of fibers and fillers on mechanical properties of thermoplastic composites, Indian Journal of Advances in Chemical Science, **2014**, 2, 28-35.

[149] J.P. Perdew, K. Burke, M. Ernzerhof, Generalized gradient approximation made simple, Phys. Rev. Lett. 77 (18) (1996) 3865–3868.

[150] Chand, P., & Kumar, P. Optik - International Journal for Light and Electron Optics, 156, 743–753, (2018).

[151] Zheng, X. G., Xu, C. N., Tanaka, E., Tomokiyo, Y., Suzuki, M., & Otabe, E. S. Physica C, 360, 181–185, (2001).

[152] Masumi, T., Imanaka, Y., Takehana, K., & Yamaguchi, H. Physica B, 298, 525–530, (2001).

[153] Bello, A., Makgopa, K., Fabiane, M., & Manyala, N. American Journal of Materials Science, *4*(2), 64–73, (2014).

[154] Tyuterev, V.G., et Nathalie Vast. Computational Materials Science 38, no 2, 350-53, 2006.

[155] Cao, H., Zhou, Z., Yu, J., & Zhou, X. Journal of Computational Electronics, 1-8, 2017.

[156] Simon, C. E., Anisimov, V. I., Moreno, J., & Jarrell, M, Electronic Structure and Spectra of CuO, 2013.

[157] W.C. Hu, Y. Liu, D.J. Li, X.Q. Zeng, C.S. Xu, Comput. Mater. Sci. 83 27-34, 2014.

[158] Ekuma, C., Anisimov, V., Moreno, J. et al. Eur. Phys. J. B, 87: 23, 2014.

[159] Maimaiti, Y., Nolan, M., & Elliott, S. D. Physical Chemistry Chemical Physics, 16, 3036-3046, 2014.

[160] Ahmad, F., Agusta, M. K., & Dipojono, H. K. KnE Engineering, 1-7, 2016.

[161] M. Quillec, Materials for optoelectronics, Boston, M A Kluwer 1996.

[162] Dirk Poelman and Philippe Frederic Smet, *J. Phys. D: Appl. Phys.* 36 1850, 2003.

[163] Lawrence Que, "*Physical methods in bioinorganic chemistry: spectroscopy and magnetism*", University Science Books, ISBN: 9781891389023, 2000.

[164] https://www.americanelements.com/copper-ii-acetate-monohydrate-6046-93-1.

[165] C.C. Vidyasagar, Y.A. Naik, T.G. Venkatesh, R. Viswanatha, Solid-State Synthesis and Effect of Temperature on Optical Properties of CuO Nanoparticles, Powder Technol. 214, 337-343, **2011**.

[166] P. Mallick, S. Sahu, Structure, Microstructure and Optical Absorption Analysis of CuO Nanoparticles Synthesized by Sol-Gel Route, Nanosci & Nanotechnol. 2, 71–74, **2012**.

[167] G. Varughese, V. Rini, S.P. Suraj, K.T. Usha, Characterisation and optical studies of copper oxide Nanostructures doped with lanthanum ions, ADV. MAT. SCI, 4 (42), 49-60, **2014**.

[168] N. Zayyoun, B. Jaber, L. Laânab, E. Ntsoenzok, R. Bekkari, Effect of solvent on the morphological and optical properties of CuO nanoparticles prepared by simple sol-gel process, J. Mater. Environ. Sci., 7(5), 1791-1797, **2016**.

[169] K. Borgohain, S. Mahamuni, Formation of single-phase CuO quantum particles, J. Mater. Res. **2002**, 17, 1220–1223.

[170] L.C. Bourne, P.Y. Yu, A. Zettl, M.L. Cohen, High-pressure electrical conductivity measurements in the copper oxides, Phys. Rev. B., 40, 10973–10976, 1989.

[171] H. Bouyarmane, S. Saoiabi, I. El Hanbali, M. El Karbane, A. Rami, S. Masse, A. Laghzizil, T. Coradin, "Porous hydroxyapatite-TiO2 nanocomposites from natural phosphates and their decolorization properties", Eur. Phys. J. Special Topics, 224, 1863-1871, **2015**.

[172] J. Z. Zhang, Optical properties and spectroscopy of nanomaterials; ed. by World Scientific Publishing Co. Pte. Ltd, pp. 229-299, 2009.

[173] Heinemann, M., Eifert, B., & Heiliger, C Phys. Rev. B 87, 115111, (2013).

[174] Nolan, M., & Elliott, S. D. Phys. Chem. Chem. Phys, 8, 5350-5358, (2006).

[175] Dhaouadi, M., Jlassi, M., Sta, I., Miled, I. Ben, Mousdis, G., Kompitsas, M., & Dimassi, W. 6(2), 43–50, 2018.

[176] C. Franchini, R. Podloucky, J. Paier, M. Marsman, and G. Kresse, Phys. Rev. B **75**, 195128, 2007.

[177] F. Schmidt-Stein, R. Hahn, J. F. Gnichwitz, Y.Y. Song, N. K. Shrestha, A. Hirsch, P. Schmuki, Electrochem.Commun, 11 (2009) 2077.

[178] A.A Dorothy, N.G Subramaniam and P. Panigrahi, Materials Research Express (2019).

[179] H. He, C. Liu, K. D. Dubois, T. Jin, M. E. Louis, G. Li**,** Ind. Eng. Chem. Res.51 (2012) 11841.

[180] Varghese, O.K., M. Paulose, and C.A. Grimes,. Nature Nano, 2009. **4**(9): pp. 592-597.

[181] Liu C.M., C. Chen, and H.E. Cheng, Electrochemical and Solid- State Letters, 2011. **14**(6): pp. K33-K35.

[182] H. Wu, D. Li, X. Zhu, C. Yanga, D. Liu, X. Chen, Y. Song, L. Lu, Electrochimica Acta *116 (2014) 129-136.*

[183] H. Dong, G. Zeng, L. Tang, C. Fan, C. Zhang, X. He, Y. He, Wat. Res, 79, 2015, 128-146.

[184] J. Xu, X. Liu, Y. Chen, Y. Zhou, T. Lu, Y. Tang, J. Mater. Chem. 22 (2012) 23659–23667.

[185] M.L. Taylor, G.E. Morris, Roger.St.C. Smart, J. Colloid Interf. Sci. 262 (2003) 81.

[186] M. Sokmen, A. Ozkan, J. Photochem. Photobiol. A: Chem. 147 (2002) 77.

[187] K.L. Frindell, M.H. Bartl, M.R. Robinson, G.C. Bazan, A. Popitsch, G.D. Stucky, J. Solid State Chem. 172 (2003) 81.

[188] Chen X, Burda C: The electronic origin of the visible-light absorption properties of C–, N- and S-doped TiO2 nanomaterials. J Am Chem Soc 2008, 130:5018–5019.

[189] De Angelis F, Fantacci S, Selloni A, Nazeeruddin MK, Grätzel M: Firstprinciples modeling of the adsorption geometry and electronic structure of Ru (II) dyes on extended TiO2 substrates for dye-sensitized solar cell applications. J Phys Chem C 2010, 114:6054–6061.

[190] Valentin CD, Pacchioni G, Onishi H, Kudo A: Cr/Sb co-doped TiO2 from first principles calculations. Chem Phys Lett 2009, 469:166–171.

[191] Hou XG, Liu AD, Huang MD, Liao B, Wu XL: First-principles band calculations on electronic structures of Ag-doped rutile and anatase TiO2. Chin Phys Lett 2009, 26:077106.

[192] Zhang LK, Wu B, Wang M, Chen L, Ye GX, Chen T, Liu HL, Huang CR, Li JL: Crystal, electronic and magnetic structure of Co and Ag doped rutile TiO2 from first-principles calculations. Adv Mater Res 2012, 399:1789–1792.

[193] X. Zheng, X. Zhang, X. Wang, S. Wang, S. Wu, Applied Catalysis A: General 295 (2005) 142–149.

[194] R. Prasad, J. Therm. Anal. Calorim. 85 (2006) 279-284.

[195] K. Krishnamoorthy, S. Kim, Mat Res Bulletin 48 (2013) 3136-3139.

[196] A. Bendavid, P.J. Martin, Å. Jamting, H. Takikawa, Thin Solid Films 355 (1999) 6-11.

[197] Y. Yan, T.W. Xinran, L.H. Pang, H. Xue, Inorg Chem Front 4 (2017) 33-51.

[198] S. Krehula, S. Musiæ, Croatia Chemical Acta 84 (4) (2011) 465–468.

[199] J. Matthey, O. Road, Platinum Metals Rev 57 (4) (2013) 259–271.

[200] H. Pang, Y. Ma, G. Li, J. Chen, J. Zhang, H. Zheng, W. Du, Dalton Trans. 41 13284 2012.

[201] G.S. Gund, D.P. Dubal, S.B. Jambhure, S.S. Shinde, C.D. Lokhande, J. Mater. Chem. A 299 (2013) 4793.

[202] J. Zhang, Z. Zhang, Y. Jiao, H. Yang, Y. Li, J. Zhang, P. Gao, J Power Sources 419 (2019) 99-105.

[203] S. Ramesh, A. Kathalingam, K. Karuppasamy, H.S Kim, H.S Kim, Composites Part B 166 (2019) 74-85.

[204] P. Prasannalakshmi, N. Shanmugam, A. Senthil kumar, N. Kannadasan, 775 pp. 356-363, 2016.

[205] J, Chrzanowski, J.C. Irwin, Solid State Communications, 70 (1989) ll-14.

[206] J.F. Xu, W. Ji, Z.X. Shen, W.S. Li, S.H. Tang, X.R. Ye, D.Z. Jia, X.Q. Xin, J. Raman Spectro 30 (1999) 413-415.

[207] P. Georgios, S.M. Wolfgang, Solid State Phenom. 162 (2010) 163–177.

[208] Deng, C, Li, B, Dong, L.; Zhang, F Fan, M, Jin, G, Gao, J, Gao, L, Zhang, F, Zhou, X. Phys Chem Chem Phys 17 (2015) 16092–16109.

[209] Z, Shan, P.S Archana. G. Shen, A. Gupta, M.G. Bakker, S. Pan, Nanocot: J Am Chem Soc **2015**, 137, 11996–12005.

[210] J. F Moulder, W.F Stickle, P.E. Sobol & Bomben K. D. *Handbook of X-ray Photoelectron Spectroscopy*. 44–89 (Eden Prairie: Perkin Elmer, 1992).

[211] M.T. Qamar, M. Aslam, I.M.I Ismail, N. Salah & A. Hameed, *ACS Appl Mater Inter* 7 pp. 8757-8769, 2015.

[212] X. Li, H. Xue, H. Pang, Nanoscale 9 (2017) 216-222.

[213] H. Absike, H. Labrim, B. Hartiti, K. Douhou, H. Ez-Zahraouy, J. Phys & Chem of Solids 132 (2019) 10-17.

[214] D. Yu, W. Zhou, Y. Liu, P. Wu Journal of Magnetism and Magnetic Materials. 404, 2016, Pages 7-13.

[215] F. H. Tian and C.B. Liu J. Phys. Chem. B 2006, 110, 17866-17871.

[216] T. Soga, Nanostructured Materials for Solar Energy Conversion, Elsevier B. V, the Nederland, (2006).

[217] W.N. Zhao, S.C. Zhu, Y.F. Li and Z.P. Liu, Chem. Sci. **6 (**2015) 3483-3494.

[218] S. Li, J. Huang, X. Ning, Y. Chen and Q. Shi, Mater. Res. Express 5 (2018) 045005.

[219] A. Dey, Materials Science and Engineering: B 229 (2018) 206-217.

[220] K. Nagaveni, M. Hegde, G. Madras, J.Phys.Chem.B 108(2004)20204.

[221] M. Guo, J.D., "First-principles study of electronic structures and optical properties of Cu, Ag, and Au-doped anatase TiO2", *Physica B* 407 pp. 1003–1007, (2012)

[222] U. Mizutani, Introduction to the electron theory of metals, Cambridge University Press, United Kingdom, (2001).

[223] H.S. Park, D.H.Kim, S.J. Kim, K.S. Lee, J. Alloys Compd. 415 (2006) 51

[224] A.A Dorothy, N. Subramaniam and P. Panigrahi, "Tuning Electronic and Optical properties of TiO2 with Pt/Ag doping to a Prospective Photocatalyst: A first principles DFT study" *Mat. Res. Express*, 2019.

[225] W. Naffouti, T.B Nasr, H. Medradji, N.K Turki, Journal of electronic Materials 45 (2016) 5096–5103.

[226] Hao, Q., Xu, D., & Zhao, H. ECS Journal of Solid-State Science and Technology, 6 (3) N3095-N3102 (2017).

[227] Y. Chen, D. D. Dionysiou, Sol-gel synthesis of nanostructured TiO2 films for water purification, Sol-gel methods for materials processing NATO science for peace and security series C: Environmental Security 67, 2008.

[228] Z. Xiong, J. Ma, W. J. Ng, T.D. Waite, X. S. Zhao, Silver-modified mesoporous TiO2 photocatalyst for water purification, Water Research 45 2095, 2011.

[229] M D. Newman, M. Stotland, J. I. Ellis, The safety of nanosized particles in titanium dioxide and zinc oxide based sunscreens. J. Am. Acad. Dermatol. 61 685, 2009.

[230] T. G. Smijs, S. Pavel, "Titanium dioxide and zinc oxide nanoparticles in sunscreens: focus on their safety and effectiveness", *Nanotechnol. Sci. Appl.* 4 95, 2011.

[231] Q. H. Chen, H. L. Liu, Y. J.Xin, X. W. Cheng, J. Zhang, J. J. Li, P. Wang, H. J. Li, Electrochim. Acta, 99 (2013) 152.

[232] A.Haring,A.Morris,M.Hu, Materials,5(2012)1890.

[233] P.Roy,S.Berger,P.Schmuki, Angew. Chem. Int. Ed.,50(2011) 2904.

[234] K. Yasuda, J. M. Macak, S. Berger, A. Ghicov, P. Schmuki, J. Electrochem. Soc., 154 (2007) C472.

[235] R. X. Ge, W. Y. Fu, H. B. Yang, Y. Y. Zhang, W. Y. Zhao, Z. L. Liu, C. J. Wang, H. Y. Zhu, Q. J. Yu, G. T. Zou, Mater. Lett., 62 (2008) 2688.
[236] C. B. Marien, T. Cottinea, D. Robert, P. Drogui, Appl. Catal. B: Environ, 194 (2016) 1.

Published articles:

- **Loubaba. Attou**, Boujemaâ. Jaber and Hamid. Ez-Zahraouy**,** Effect of annealing temperature on structural, optical and photocatalytic properties of CuO nanoparticles, *Mediterranean Journal of Chemistry*, **2018**, 7(5), 308-316.
  DOI : 10.13171/mjc751911261230la

- **Loubaba. Attou**, Boujemaâ. Jaber and Hamid. Ez-Zahraouy, CuO NPs on Pt-sputtered TiO2-TNTs composite material for supercapacitors applications: investigation on its electrochemical properties, *Applied Physics A, Materials Science & Processing*, **2019**, 125(8).
  DOI: 10.1007/s00339-019-2858-4

In progress articles:

- **Loubaba. Attou**, Boujemaâ. Jaber and Hamid. Ez-Zahraouy, Investigation on electronic, optical and thermoelectric properties of metal oxides doped TiO2 using pseudopotetntial approximations.

Résumé

Les oxydes métalliques présentent des propriétés électroniques prometteuses dans différentes applications comme le stockage d'énergie. Le but de cette thèse serait d'élaborer un matériau composite qui rassemblera ces oxydes, puis d'explorer ses performances électroniques et électrochimiques. D'une part étudier théoriquement le CuO (II) en utilisant la méthode FP LAPW, basée sur la DFT avec l'approche corrective modifiée Becke-Johnson mBJ, et expérimentalement par l'effet de la température de recuit sur les propriétés des NPs du CuO élaboré par la méthode Solgel. D'autre part, fabriquer le matériau composite CPTNT (CuO/Pt-TiO2) à partir d'une anodisation des NTs de TiO2, pulvérisant les NPs du Pt en dessus suivi par une électrodéposition des NPs du Cu dans le matériau, et une oxydation du cuivre par recuit thermique. Les propriétés électrochimiques et le comportement capacitif de ce matériau sont évalués en utilisant la voltampérométrie cyclique (CV), la spectroscopie d'impédance électrochimique (EIS) et la chronopotentiométrie (GCD). Une capacité spécifique élevée de 423 F g^{-1} est atteinte à une densité de courant de 0,5 A g^{-1}, avec une stabilité à long terme de 93% sur 5000 cycles. De plus, les résultats démontrent que cette électrode pourra délivrer une haute densité d'énergie de 19,62 Wh Kg^{-1} et une densité de puissance jusqu'à 442,89 W Kg^{-1}. La DFT est utilisée pour étudier la structure électronique du TiO2 codopé par (Cu, Pt), afin de mieux comprendre ses comportements électrochimiques. Les résultats obtenus tout au long de cette étude démontrent que ce nouveau nanocomposite est un candidat notable pour les supercondensateurs à haute performance.

Mots-clés : Anodisation, Dioxyde de titane, CuO, Stockage d'énergie, Conductivité électrique, DFT

Abstract

Metal oxides show promising electronic properties in energy storage applications. The goal of this thesis would be to develop a composite material associating these oxides, then to explore its electronic and electrochemical performance. In the first part, studying theoretically CuO (II) using the FP LAPW method based on DFT with mBJ corrective approach, and experimentally by the effect of the annealing temperature on the properties of the NPs of the CuO produced by the Solgel method. In the second part, fabricating the CPTNT (CuO / Pt-TiO2) composite material from an initial anodic fabrication of the well-ordered TiO2 NTs, sputtering the Pt NPs followed by electrodeposition of the Cu NPs in the material as obtained, followed by oxidation of the copper by thermal annealing. The electrochemical properties and capacitive behavior of this material are evaluated using Cyclic Voltammetry (CV), Electrochemical Impedance Spectroscopy (EIS) and Chronopotentiometry (GCD). A high specific capacity of 423 F g^{-1} is achieved at a current density of 0.5 A g^{-1}, with long term stability of 93% over 5000 cycles. The results show that this electrode will be able to deliver a high energy density of 19.62 Wh Kg^{-1} and a power density of up to 442.89 W Kg^{-1}. DFT is used to study the electronic structure of TiO2 codoped by (Cu, Pt), in order to better understand its electrochemical behavior. The results obtained throughout this study demonstrate that this new nanocomposite is a notable candidate for high performance supercapacitors.

Key Words: Anodization, Titanium dioxide, CuO, Energy Storage, Electrical conductivity, DFT